AD-A121 791 FINITE-ELEMENT FORMULATION FOR THE ANALYSIS OF PLASTIC DEFORMATION OF RAT.. (U) CALIFORNIA UNIV BERKELEY DEPT OF MECHANICAL ENGINEERING S KOBAYASHI 29 OCT 82 1/1

UNCLASSIFIED ARO-15868.8-EG DAAG29-79-C-0217 F/G 11/6 NL

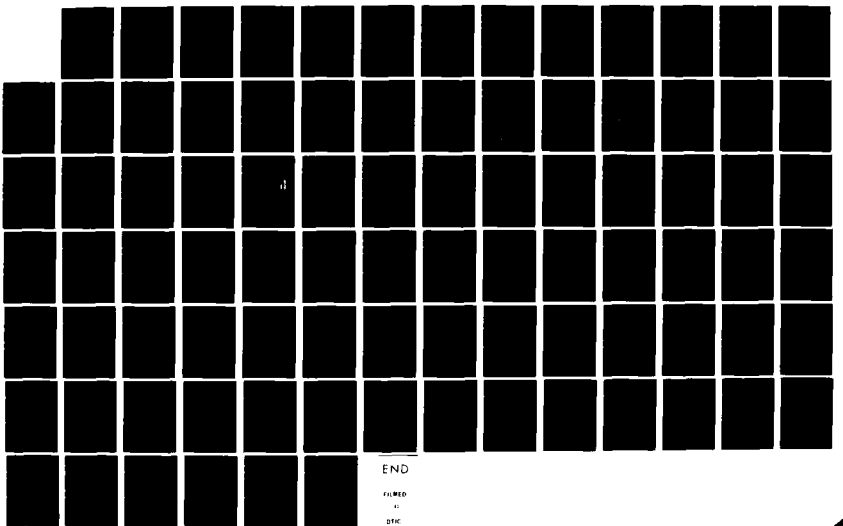

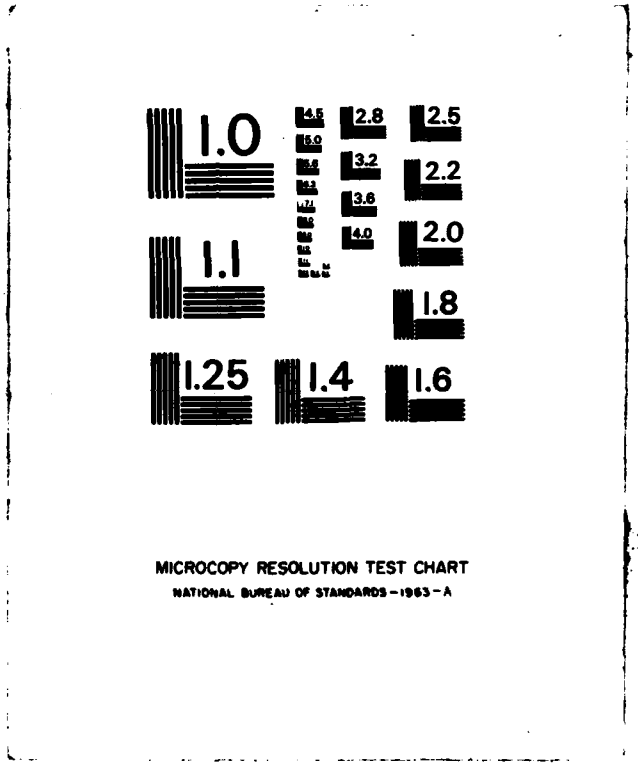

MICROCOPY RESOLUTION TEST CHART
NATIONAL BUREAU OF STANDARDS-1963-A

FINITE ELEMENT FORMULATION FOR THE ANALYSIS OF PLASTIC DEFORMATION OF RATE-SENSITIVE MATERIALS IN METAL FORMING

Final Report

by

S[illegible] Kobayashi

October 29, 1982

U.S. Army Research Office

Contract DAAG29-79-C-0217

Department of Mechanical Engineering
University of California
Berkeley, California 94720

APPROVED FOR PUBLIC RELEASE:
Distribution Unlimited

Unclassified

SECURITY CLASSIFICATION OF THIS PAGE (When Data Entered)

REPORT DOCUMENTATION PAGE	READ INSTRUCTIONS BEFORE COMPLETING FORM
1. REPORT NUMBER	2. GOVT ACCESSION NO. AD-A121 791	3. RECIPIENT'S CATALOG NUMBER
4. TITLE (and Subtitle) Finite-Element Formulation for the Analysis of Plastic Deformation of Rate-Sensitive Materials in Metal Forming	5. TYPE OF REPORT & PERIOD COVERED Final Report, Sept. 20,1979 - Sept. 19, 1982
	6. PERFORMING ORG. REPORT NUMBER
7. AUTHOR(s) Shiro Kobayashi	8. CONTRACT OR GRANT NUMBER(s) DAAG29-79-C-0217
9. PERFORMING ORGANIZATION NAME AND ADDRESS Department of Mechanical Engineering University of California Berkeley, California 94720	10. PROGRAM ELEMENT, PROJECT, TASK AREA & WORK UNIT NUMBERS
11. CONTROLLING OFFICE NAME AND ADDRESS U. S. Army Research Office Post Office Box 12211 Research Triangle Park, NC 27709	12. REPORT DATE October 29, 1982
	13. NUMBER OF PAGES 85
14. MONITORING AGENCY NAME & ADDRESS(if different from Controlling Office)	15. SECURITY CLASS. (of this report) Unclassified
	15a. DECLASSIFICATION/DOWNGRADING SCHEDULE NA

16. DISTRIBUTION STATEMENT (of this Report)

Approved for public release; distribution unlimited.

17. DISTRIBUTION STATEMENT (of the abstract entered in Block 20, if different from Report)

NA

18. SUPPLEMENTARY NOTES

The findings in this report are not to be construed as an official Department of the Army position, unless so designated by other authorized documents.

19. KEY WORDS (Continue on reverse side if necessary and identify by block number)

Finite-Element Method, Viscoplasticity, metal forming. Nosing, Preform Design.

20. ABSTRACT (Continue on reverse side if necessary and identify by block number)

The finite-element formulation for the analysis of metalworking problems for rigid-viscoplastic materials, including the effect of temperature, has been established. Of particular significance is an accomplishment of the coupled analysis of deformation and heat transfer. The formulations were applied to the problems of solid cylinder compression and ring compression. Then, the forming processes of shell nosing at room temperature, as well as at elevated temperatures, were analyzed. The results demonstrate that it is

DD FORM 1 JAN 73 1473 EDITION OF 1 NOV 65 IS OBSOLETE

Unclassified

SECURITY CLASSIFICATION OF THIS PAGE (When Data Entered)

[20] Abstract (continued).

now possible to analyze accurately not only cold forming processes, but also processes in warm and hot forming regimes, by the finite-element method, including the effects of strain, strain-rate, and temperature on material properties. Most recent achievement is an introduction of a new approach to the problem of preform design in shell nosing as a unique application of the finite-element method. The concept involved in the approach is to trace backward the loading path from a given final configuration. The method was applied to preform design in shell nosing.

1. Problem Statement

The objective of the research is to establish a finite-element formulation for the analysis of flow behavior of rate sensitive materials under large plastic deformation. Specifically, the main concern is with flow analysis of metal-forming processes at elevated temperatures. The material's behavior is characterized as rigid-viscoplastic. To accomplish this objective the research was undertaken for the construction of constitutive relations and for establishing basic principles for the finite-element formulation.

In order to demonstrate the usefulness of the theory, the finite-element method code was written and the problems unique in the area of metal-forming were solved.

2. Summary of the Results

A thermodynamic theory of deformation using internal variables was adapted to rigid viscoplastic materials, and the finite element discretization for the analysis of metal-forming problems was established. Of particular significance is an accomplishment of the coupled analysis of deformation and heat transfer. The finite element formulations for coupled analysis were applied to the problems of solid cylinder compression and ring compression. The temperature distributions in solid cylinder compression are compared with experimental data, and the computed results of ring compression of aluminum at elevated temperature are compared with experimental observations as well as with calculated results not including the temperature effects. It is demonstrated that the coupled analysis accurately simulates these processes.

The capabilities of a coupled thermoviscoplastic analysis of non-steady-state forming processes were further demonstrated in the analysis of the shell nosing processes at room temperature, as well as at elevated temperatures.

In cold nosing simulations, the nine-node quadrilateral elements with quadratic velocity distribution were used for the workpiece. The treatment of a moving boundary in the analysis of nosing is discussed and successfully implemented in the finite-element program. FEM simulations of 105-mm diam. shells of AISI 1018 steel and aluminum 2024 were performed and solutions were obtained in terms of load-displacement curves, thickness distribution, elongation, and strain distributions. Comparisons with experimental data show very good agreement.

In the analysis of shell nosing at elevated temperatures, the strain-rate effects on materials properties and the flow stress dependence on temperatures were included in the finite-element analysis. A thermodynamic theory of viscoplasticity based on rational mechanics was adapted to a rigid-plastic material idealization. An implicit scheme is used for the time integration of heat transfer equations, which is coupled to the plasticity equations.

The nine-node quadrilateral elements with quadratic velocity distribution were used for the workpiece, and four-node quadrilateral elements were used for the die in the heat transfer analysis and temperature calculations. The coupled analysis of heat transfer and deformation was applied to the forming of AISI 1045 steel shells. Correlation between simulation and experimental results are good. The results of the analysis of shell nosing processes again confirmed that the coupled thermoviscoplastic analysis by the finite-element method is indeed a significant accomplishment.

The research was continued to explore the use of the capabilities of the finite-element technique to outstanding problem areas in metal forming. In the study on the finite-element analysis of nosing of aluminum alloy 2024 tubular preforms with uniform wall thickness at room temperature, the detailed mechanics were obtained by computer simulation, and the finite-element method was suggested as a fitting approach to solving the problem of preform design in metal forming. The approach assumes that the strain distributions computed by the finite-element method are valid for preforms having nonuniform thicknesses initially, and two types of preform shapes were designed to obtain uniform wall thickness after nosing. Experimental results of nosing these preforms showed that the approach to the problem is satisfactory.

Most recent achievement in this area of preform design in metal forming is an introduction of a new approach to the problem as a unique application of the finite element method. The concept involved in the approach is to trace backward the loading path in the actual forming process from a given final configuration using the finite-element method. The concept was tested with the problem of simple compression of a cylinder and the method was applied to preform design in shell nosing.

For the further development of the new approach to preform design in shell nosing, two approximate solutions were derived. The degree of approximation was examined by the accurate numerical solution based on the new approach

by the finite-element method, for an example of uniform wall thickness of the nosed shell. It was demonstrated that both approximate solutions are useful in design, one for its simplicity and the other for its accuracy. The results of the study on preform design are encouraging in the challenge to this significant and difficult problem in metal forming.

3. List of publications

1. N. Rebelo and Shiro Kobayashi, "A Coupled Analysis of Viscoplastic Deformation and Heat Transfer-I Theoretical Considerations," International Journal of Mechanical Sciences, Vol. 22, 1980, p. 699.

2. N. Rebelo and Shiro Kobayashi, "A Coupled Analysis of Viscoplastic Deformation and Heat Transfer-II Applications," International Journal of Mechanical Sciences, Vol. 22, 1980, p. 707.

3. Ming-Ching Tang and Shiro Kobayashi, "An Investigation of the Shell Nosing Process by the Finite-Element Method. Part 1: Nosing at Room Temperature (Cold Nosing)," to be published in Trans. ASME, Journal of Engineering for Industry, 1982.

4. Ming-Ching Tang and Shiro Kobayashi, "An Investigation of the Shell Nosing Process by the Finite-Element Method. Part 2: Nosing at Elevated Temperatures (Hot Nosing)," to be published in Trans. ASME, Journal of Engineering for Industry, 1982.

5. MIng-Ching Tang, May Hsu and Shiro Kobayashi, "Analysis of Shell Nosing - Process Mechanics and Preform Design," to be published in International Journal of Machine Tool Design and Research, 1982.

6. J. J. Park, N. Rebelo and Shiro Kobayashi, "A New Approach to Preform Design in Metal Forming with the Finite-Element Method," to be published in International Journal of Machine Tool Design and Research, 1983.

7. Shiro Kobayashi, "Approximate Solutions for Preform Design in Shell Nosing," to be published in International Journal of Machine Tool Design and Research, 1983.

The copy of the above publications is given in the Appendix as a part of the report.

4. List of Scientific Personnel

Principal Investigator: Shiro Kobayashi.

1. N. Rebelo, Ph.D. degree, October, 1980.
2. M. N. Tang, Ph.D. degree, September, 1981.
3. May Hsu, M.S. degree, June, 1981.
4. J. J. Park (Ph.D. candidate).
5. C. H. Toh (Ph.D. candidate).

5. Appendix

Copy of the publications.

Int. J. Mech. Sci. Vol. 22, pp. 699–705
Pergamon Press Ltd., 1980. Printed in Great Britain

5

1.

A COUPLED ANALYSIS OF VISCOPLASTIC DEFORMATION AND HEAT TRANSFER—I

THEORETICAL CONSIDERATIONS

N. REBELO and S. KOBAYASHI
Department of Mechanical Engineering, University of California, Berkeley, CA 94720, U.S.A.

(*Received* 22 *February* 1980)

Summary—A thermodynamic theory of deformation using internal variables is adapted to rigid viscoplastic materials, and the formulations for finite element discretization are given specifically for metal forming problems. A scheme of numerical integration of heat-balance equations that leads to the coupled analysis of deformation and heat transfer is presented.

NOMENCLATURE

$\dot{e}$	rate of internal energy per unit mass
q	surface density of heat influx
r	mass density of heat influx
σ_{ij}	stress tensor
$\dot{\epsilon}_{ij}$	infinitesimal strain rate tensor
ρ	mass density
$\dot{\eta}$	rate of entropy per unit mass
T	absolute temperature
ψ	specific free energy per unit mass
$T_{,i}$	temperature gradient
$\mathbf{x}$	location of material point
t	time
$g(\mathbf{x}, t)$	$\{\sigma_{ij}(\mathbf{x}, t), T(\mathbf{x}, t), T_{,i}(\mathbf{x}, t)\}$
$\pi(\mathbf{x}, t)$	$\{\psi(\mathbf{x}, t), \eta(\mathbf{x}, t), q_i(\mathbf{x}, t)\}$
$P(\mathbf{x}, t)$	$\{g(\mathbf{x}, t), \pi(\mathbf{x}, t)\}$
$\mathbf{u}$	velocity of particle
$\mathbf{F}$	body forces
$w(x, t)$	internal parameters
$h(x, t)$	$\{g(\mathbf{x}, t), w(\mathbf{x}, t)\}$
$R(h)$	$\{\phi, \eta, q_i\}$
σ'_{ij}	deviatoric stress tensor
$\bar{\dot{\epsilon}}$	effective strain rate
$\bar{\sigma}$	effective stress
Y	static yield stress
n, γ	material parameters
A, B	material constants
D	energy for self diffusion
k	Boltzman constant
α	dislocation density
k_1	thermal conductivity
ν	energy per unit length of dislocation
$\delta(\ )$	variation of ( )
q_n	heat flow through surface of normal n
$T_{,n}$	temperature gradient along normal n
q_n^r	radiated heat
ϵ	emissivity of the surface
σ	Boltzman constant
T_0	reference temperature/initial temperature
T_e	temperature of external environment
T_s	surface temperature
q_n^c	convected heat
h	surface heat transfer coefficient
Δt	increment of time
$\mathbf{C}$	heat capacity matrix
$\mathbf{K}$	heat conduction matrix
$\mathbf{Q}$	heat flux
$\mathbf{T}$ and $\dot{\mathbf{T}}$	nodal point temperature and temperature rate vectors
β	time integration parameter
$\hat{\mathbf{T}}, \mathbf{R}$	intermediate values in time integration scheme

1. INTRODUCTION

Theoretical considerations pertaining to several disciplines are needed to perform a coupled analysis of viscoplastic deformation and heat transfer. Because these considerations adapt classical formulations to the problems in metal forming and because the necessary formulations are scattered in origin, we believe it important that they be presented together as a coherent formulation.

With the availabillty of inexpensive large computing facilities, there is a trend in the analysis of large plastic deformation for simplified material behavior descriptions to be slowly abandoned and more accurate descriptions introduced. The "problem" of solving complicated equations is left to well developed computer routines, and the analysts can now devote themselves to evaluating the appropriateness of the analysis.

The successful application of the finite element method to the analysis of metal forming processes using rigid plastic materials[1–5] leads to the simple extension to rigid viscoplastic materials[6]. The present work aims at finding the effects of temperature variations within the body on its deformation behavior. A thermodynamic theory of deformation utilizing the concept of internal parameters developed by Perzyna[7, 8] is adapted here to a rigid viscoplastic material. As an introductory treatment, plastic strain and the dislocation density are considered as the only internal parameters, and physically based laws are proposed to deal with them. We also discuss the problem of numerical integration of heat balance equations and present a time-step scheme, leading to a coupled analysis of deformation and heat transfer.

In the companion paper, some simple applications are shown, with calculation procedures and details on the treatment of boundary conditions.

2. THERMODYNAMIC FORMULATION OF THE BEHAVIOR OF RIGID VISCOPLASTIC MATERIALS

2.1 *Thermodynamic variables*

We follow the work of Perzyna[7, 8], which presents a thermodynamic theory of rate sensitive plasticity, following rational thermodynamics, with dissipative effects described by internal parameters.

A thermodynamic process is defined as one which satisfies two postulates: balance of energy and growth of entropy. The thermo mechanical state of a body at a certain time t is a collection of values of internal energy, internal entropy, entropy influx, heating, and power expended with its motion.

Using the principles of conservation of mass, linear momentum, and angular momentum, the first law of thermodynamics is locally stated as

$$\sigma_{ij}\dot{\epsilon}_{ij} + q_{i,i} + \rho r - \rho\dot{e} = 0, \tag{1}$$

and the second law of thermodynamics yields the Duhem inequality

$$\rho\dot{\eta} \geq \frac{q_{ii}}{T} - q_i\frac{T_{,i}}{T^2} + \frac{\rho r}{T}. \tag{2}$$

Calling specific free energy per unit mass ψ to be

$$\psi = e - T\eta,$$

equations (1) and (2) become

$$\sigma_{ij}\dot{\epsilon}_{ij} + q_{i,i} + \rho r - \rho(\dot{\psi} + \dot{T}\eta + T\dot{\eta}) = 0, \tag{3}$$

$$-\dot{\psi} + \dot{T}\eta + \frac{\sigma_{ij}\dot{\epsilon}_{ij}}{\rho} + \frac{q_i T_{,i}}{\rho T} \geq 0. \tag{4}$$

We assume that in order to describe a thermodynamic process in a body, we need to specify a set of three basic variables

$$g(\mathbf{x}, t) = \{\sigma_{ij}(\mathbf{x}, t), T(\mathbf{x}, t), T_{,i}(\mathbf{x}, t)\} \tag{5}$$

at each point $\mathbf{x}$, and seek to determine at each material particle a collection of functions

$$P(\mathbf{x}) = \{g(\mathbf{x}, t), \pi(\mathbf{x}, t)\}, \tag{6}$$

where π represents the set of variables

$$\pi(\mathbf{x}, t) = \{\psi(\mathbf{x}, t), \eta(\mathbf{x}, t), q_i(\mathbf{x}, t)\}, \tag{7}$$

satisfying inequality (4).

Heat supply $r(\mathbf{x}, t)$ and body forces F do not need to be specified, as they can be determined by (3) and by equilibrium equation

$$\sigma_{ij,j} + F_i = \rho \ddot{u}_i. \tag{8}$$

2.2 *Constitutive equations*

For the definition of the thermo-mechanical state, two propositions are accepted; (1) the thermo-mechanical state can be specified by $g(x, t)$ and by its method of preparation, (2) the method of preparing the actual stress temperature configuration can be determined by one group of internal parameters $w(\mathbf{x}, t)$, which, in a ridid, rate sensitive plastic material, describes internal structure changes produced by plastic deformation.

Accordingly, the thermo-mechanical state of a particle at x at time t is described by the value at t of

$$h(\mathbf{x}, t) = \{g(\mathbf{x}, t), w(\mathbf{x}, t)\}, \tag{9}$$

and by the initial value problems given by

$$\dot{w}(\mathbf{x}, t) = W(h(\mathbf{x}, t)), \tag{10}$$

$$w(\mathbf{x}, t_0) = w_0(\mathbf{x}). \tag{11}$$

It is assumed that constitutive relations determine

$$\pi(\mathbf{x}, t) = R(h), \tag{12}$$

with

$$R = \{\psi, \eta, q_i\}.$$

The Duhem inequality imposes some restrictions on the constitutive relations (12).

Assume that ψ is a piecewise continuously differentiable function with respect to $h(\mathbf{x}, t)$;

$$\dot{\psi} = \frac{\partial \psi}{\partial T}\dot{T} + \frac{\partial \psi}{\partial T_{,i}}\dot{T}_{,i} + \frac{\partial \psi}{\partial w}\dot{w} + \frac{\partial \psi}{\partial \sigma_{ij}}\dot{\sigma}_{ij}. \tag{13}$$

Then (4) becomes

$$-\left(\frac{\partial \psi}{\partial T} + \eta\right)\dot{T} - \frac{\partial \psi}{\partial T_{,i}}\dot{T}_{,i} - \frac{\partial \psi}{\partial \sigma_{ij}}\dot{\sigma}_{ij}$$

$$+\frac{\sigma_{ij}\dot{\varepsilon}_{ij}}{\rho} - \frac{\partial \psi}{\partial w}\dot{w} + \frac{q_i T_{,i}}{\rho T} \geq 0. \tag{14}$$

Since we can choose arbitrarily $\dot{T}$, $\dot{T}_{,i}$ and $\dot{\sigma}_{ij}$ for a process and still obtain an admissible local thermodynamic process, it must be

$$\frac{\partial \psi}{\partial T_{,i}} = 0, \tag{15}$$

$$\frac{\partial \psi}{\partial T} = -\eta, \tag{16}$$

$$\frac{\partial \psi}{\partial \sigma_{ij}} = 0, \tag{17}$$

$$\frac{q_i T_{,i}}{\rho T} + \frac{\sigma_{ij}\dot{\varepsilon}_{ij}}{\rho} - \frac{\partial \psi}{\partial w}\dot{w} \geq 0. \tag{18}$$

2.3 *Specialization to metal forming problems*

By using the concept of internal parameters, virtually any feature of material behavior can be taken care of, either macroscopically or microscopically. Microscopic behavior includes isotropic or anisotropic workhardening, relaxation, creep, etc. and microscopic includes, dislocation density, phase tranformation, grain properties, etc.

Unfortunately, data referring to this kind of treatment are not easily available. Hart *et al.*[9–11] have developed an experimental program where an exhaustive number of phenomena are taken into consideration to describe the nonelastic deformation of metals. This type of data, when fully available, will be an excellent basis for the present formulation.

For the time being a simple analysis is made, in which the only internal parameters considered are the plastic strain tensor and the dislocation density α. These parameters are involved with a measurement of workhardening and the change in free energy that external loads produce during deformation in a stable non- recrystalizing material.

The rate equation (10) corresponding to the plastic strain tensor is simply borrowed from the mechanical analysis of rigid viscoplastic deformation[6, 12]. We recall that a stress space yield surface expands with the strain rate from a static yield surface, and that a Mises-like law is obtained, provided we assume isotropy, isotropic workhardening, and no further dependence on internal parameters.

$$\dot{\epsilon}_{ij} = \frac{3}{2}\frac{\dot{\bar{\epsilon}}}{\bar{\sigma}}\sigma'_{ij}. \tag{19}$$

In (19) $\bar{\sigma}$ is a function of strain, strain rate and temperature, and is the scalar representation of how the yield surface behaves. In order to express the dependence on strain rate, experimental data were found to be adequately fitted by expressions of the form

$$\sigma = Y\left[1 + \left(\frac{\dot{\bar{\epsilon}}}{\gamma}\right)^n\right], \tag{20}$$

where Y is the static yield stress, and Y, n and γ are functions of strain and temperature.

The rate equation (10) corresponding to the dislocation density is written based on physical grounds, although the values can be accurate only to the order of magnitude. For this reason we use a simple macroscopic approach, instead of the elaborate physical metallurgy models. Fortunately, as will be seen in the final form of the heat balance equations, the contribution of these terms is small. We take then

$$\dot{\alpha} = A\dot{\bar{\epsilon}} - B\alpha e^{-D/kT},$$
$$\alpha(t_0) = \alpha_0, \tag{21}$$

in a simple attempt to say that dislocation density will have both a positive rate component, due to an increase in plastic deformation (strain hardening), and a negative one. In terms of high temperature deformation, this negative component can be due to annihilation occurring from the diffusion-driven climb of dislocations. In such a case, the greater the number of dislocations, the higher the probability of annihilation.

The constitutive relations (12) are specialized as follows.

A hot metalworking process does not usually take very long, and the temperature changes come from plastic work and losses to the environment. Therefore, an isotropic Fourier law for heat flux, with constant thermal conductivity k_1 is appropriate

$$q_i = k_1 T_{,i}. \tag{22}$$

As is done in elastic–plastic theory[13–15], we assume the following decomposition

$$\psi = \psi_1(T) + \psi_2(\epsilon_{ij}, \alpha), \tag{23}$$

and take

$$\psi_1 = -\int_{T_0}^{T}\left(\int_{T_0}^{T}\frac{c}{T}\,dT\right)dT, \tag{24}$$

where the specific heat (at constant volume) c is assumed constant in the working temperature range.

Now the internal parameters can be used to describe the energy which goes into the structure of the material. Since we neglect elastic deformation, strain energy doesn't apply, and only the energy of dislocations is involved, as

$$\psi_2 = \frac{\nu\alpha}{\rho}. \tag{25}$$

From (23), (24) and (16) we have

$$\psi = -\int_{T_0}^{T}\left(\int_{T_0}^{T}\frac{c}{T}\,dT\right)dT + \frac{\nu\alpha}{\rho}, \tag{23a}$$

$$\eta = \int_{T_0}^{T}\frac{c}{T}\,dT, \tag{16a}$$

and the dissipation inequality (18) becomes

$$\frac{q_i T_{,i}}{\rho T} + \frac{\sigma_{ij}\dot{\epsilon}_{ij}}{\rho} - \frac{\nu A}{\rho}\dot{\bar{\epsilon}} + \frac{\nu B\alpha}{\rho}e^{-D/kT} \geq 0. \tag{26}$$

In (26) $q_i T_{,i} \geq 0$, therefore,

$$\sigma_{ij}\dot{\epsilon}_{ij} \geq \nu A\dot{\bar{\epsilon}} - \nu B\alpha e^{-D/kT}. \tag{26a}$$

This restriction is satisfied with experimentally determined values of ν, A and B. In fact, the r.h.s. represents the rate of energy spent in creating new dislocations, and it has been shown experimentally that this dislocation energy ranges between 5 and 15% of the work spent in plastic deformation.

3. LOADING AND BOUNDARY CONDITIONS

Usually temperatures, temperature rates and stresses are not specified in a process; instead body forces and boundary tractions, together with heat supply both internal and through the surface are known. The equivalence is obtained through equilibrium and energy balance equations.

As closed-form solutions are virtually impossible to obtain in a general problem, numerical approximations are sought. A finite element discretization is a widely used and well-proved method to which we will refer, without entering into its details.

Assuming that no body forces and no inertial effects are present, equilibrium equations become, through the volume

$$\sigma_{ij,j} = 0. \tag{27}$$

Writing equation (27) in a weak form

$$\int_v \sigma_{ij,j}\delta u_i \, dv = 0. \tag{28}$$

Applying the divergence theorem to equation (28), we obtain

$$\int_v \sigma_{ij}\delta\dot{\epsilon}_{ij} \, dv - \int_{S_F} T_i\delta u_i \, dS_F = 0, \tag{29}$$

with imposition of boundary tractions

$$T_i = \sigma_{ij}n_j. \tag{30}$$

Boundary displacements are imposed in the form of their rates (velocities). By discretizing, using (19), and solving finite element equations, a velocity field is obtained and strain rates and stresses are determined.

The energy balance equation (3), considering no external body heat supply, becomes

$$\sigma'_{ij}\dot{\epsilon}_{ij} + k_1 T_{,ii} - \rho c\dot{T} - \nu A\dot{\bar{\epsilon}} + \nu B\alpha e^{-D/kT} = 0, \tag{31}$$

and, in a weak form,

$$\int_v k_1 T_{,ii}\delta T \, dv - \int_v \rho c\dot{T}\delta T \, dv + \int_v (\sigma'_{ij}\dot{\epsilon}_{ij} - \nu A\dot{\bar{\epsilon}} + \nu B\alpha e^{-D/kT})\delta T \, dv = 0. \tag{32}$$

By using the divergence theorem

$$\int_v k_1 T_{,i}\delta T_{,i} \, dv + \int_v \rho c\dot{T}\delta T \, dv - \int (\sigma'_{ij}\dot{\epsilon}_{ij} - \nu A\dot{\bar{\epsilon}} + \nu B\alpha e^{-D/kT})\delta T \, dv - \int_{s_q} q_n\delta T \, ds_q = 0, \tag{33}$$

where

$$q_n = k_1 T_{,n} \tag{34}$$

is the boundary heat flow.

Simple forms of boundary heat flow suffice for the present formulation. Radiation heat flow is expressed as

$$q_n^r = \sigma\epsilon(T_e^4 - T_s^4). \tag{34a}$$

Convection heat flow is expressed as

$$q_n^c = h(T_e - T_s). \tag{34b}$$

Temperatures also can be directly imposed. Upon discretization and solution of finite element equations, we obtain a temperature field provided we know stresses and strain rates.

Equations (29) and (33) are highly coupled, making a simultaneous solution of their finite element counterparts necessary. This process is treated with time dimension analysis.

4. TIME DIMENSION

In order to describe a deformation process in time, integration of rate equations (19), (21) and (33) must be performed with respect to time. As far as the strain equation is concerned, the assumption of no inertial effects requires that for small intervals of time, velocities (and strain rates) change by very small amounts. The strains at time $t + \Delta t$ are obtained from their values and rates at time t

$$\epsilon_{t+\Delta t} = \epsilon_t + \dot{\epsilon}_t \Delta t. \tag{35}$$

Similar treatment is made with respect to updating displacements, using velocities.

In standard finite element books, e.g. [16], it can be seen that heat balance equations such as equation (33), upon finite element discretization are reduced to the form

$$\underline{C}\dot{\mathbf{T}} + \underline{K}\mathbf{T} = \mathbf{Q}. \tag{36}$$

The theory necessary to integrate these equations can be found in numerical analysis books [17, 18]. It suffices to say that one-step method is used. Convergence of a scheme requires consistency and stability. Consistency is satisfied by an approximation of the type

$$\mathbf{T}_{t+\Delta t} = \mathbf{T}_t + \Delta t^*[(1-\beta)\dot{\mathbf{T}}_t + \beta\dot{\mathbf{T}}_{t+\Delta t}]$$

where β is a parameter varying between 0 and 1.

For unconditional stability, β should be greater than 0·5, and a value of 0·75 was chosen. Selection of a proper value for β is an important factor in the situation where it is desired that the time step be as large as possible, provided that the increments in strain are compatible with an infinitesimal analysis. In the standard test problem for checking numerical integration schemes, this value of β gives good accuracy in a wide range of values of Δt starting at zero.

An implementation of the algorithm above, considering $\mathbf{T}_{t+\Delta t}$ as a primary dependent variable [19], has been elaborated here in order to include the coupling of the solution of stress equilibrium equations with heat balance, and to include updating of internal parameters.

The sequence of calculations to be performed in one time step Δt is as follows; (a) assume that the initial temperature field and dislocation density distribution $\mathbf{T}_0$ and α_0 are known; (b) calculate initial velocity field from equations (29); (c) calculate initial temperature rates $\dot{\mathbf{T}}_0$ from equations (36); calculate initial dislocation density rates $\dot{\alpha}_0$, from equations (21); (d) calculate

$$\hat{\dot{\mathbf{T}}} = -\frac{1}{\beta\Delta t}{}^*\mathbf{T}_0 - \left(\frac{1-\beta}{\beta}\right)^*\dot{\mathbf{T}}_0$$

(e) update displacements and strains; (f) use the old velocity field for first approximate temperature calculations

$$\mathbf{R} = \mathbf{Q}^{(1)}_{\Delta t} - \underline{C}\hat{\dot{\mathbf{T}}}$$

solve

$$\left(\underline{K} + \frac{1}{\beta\Delta t}\underline{C}\right)^*\mathbf{T}^{(1)}_{\Delta t} = \mathbf{R} \text{ for } \mathbf{T}^{(1)}_{\Delta t};$$

(g) calculate new velocity field from equations (29); (h) calculate second values for temperatures

$$\mathbf{R} = \mathbf{Q}^{(2)}_{\Delta t} - \underline{C}\hat{\dot{\mathbf{T}}}$$

solve

$$\left(\underline{K} + \frac{1}{\beta\Delta t}\underline{C}\right)^*\mathbf{T}^{(2)}_{\Delta t} = \mathbf{R} \text{ for } \mathbf{T}^{(2)}_{\Delta t}$$

use a similar procedure to calculate dislocation density; (i) iterate until convergence; (j) calculate new temperature rate

$$\dot{\mathbf{T}}_{\Delta t} = \hat{\dot{\mathbf{T}}} + \frac{1}{\beta\Delta t}\mathbf{T}_{\Delta t}$$

and new dislocation density rate.

It should be noted that integration of equations (21) follows the same procedure described above, since equations (21) and (36) are of the same type.

5. CONCLUDING REMARKS

In order to simplify the description of the algorithm for the coupled analysis, the solution for the velocity fields has not been detailed. The finite element equations obtained from (29) and (19) are nonlinear, and an iterative scheme based on the Raphson method is used. Such a scheme, as well as convergence criteria, has been described at length in previous papers [2, 3, 5].

Dislocation density values used are averages for each element. This procedure is justified by the large uncertainty in data, and by the moderate influence of these values in the rest of the calculations.

We have presented the theoretical background necessary for the solution of metalworking problems in which temperature variations as well as a heat transfer analysis are important. The concept of internal parameters, and the way they are imbedded in the solution algorithm, opens good perspectives for better descriptions of material behavior, and of physical phenomena concurrent with plastic deformation.

Acknowledgements—The authors wish to thank the Battelle Columbus Laboratories for the contract S-2935(7128) and the Army Research Office for the contract DAAG29-79-C-0217 under which the present work was possible. They also wish to thank Ms. Katie Triest for editing the manuscript.

REFERENCES

1. C. H. Lee and S. Kobayashi, New solutions to rigid plastic deformation problems using a matrix method. *Trans. ASME, J. Engr. Ind.* 98, 865 (1973).
2. S. I. Oh and S. Kobayashi, Workability of aluminum alloy 7075-T6 in upsetting and rolling. *Trans. ASME, J. Engr. Ind.* 98, 809 (1976).
3. S. Kobayashi and S. N. Shah, The matrix method for the analysis of metal-forming processes. *Advances in Deformation Processing*, p. 51, Plenum Press, New York (1978).
4. S. Kobayashi and J. H. Kim, Deformation analysis of axisymmetric sheet metal forming processes by the rigid-plastic finite element method, *Mechanics of Sheet Metal Forming* (Editors, D. P. Koistinen and N. M. Wang) p. 341. Plenum Press, New York (1978).
5. C. C. Chen and S. Kobayashi, Rigid plastic finite element analysis of ring compression. In *Applications of Numerical Methods to Forming Processes, ASME*, AMD Vol. 28, p. 163, New York (1978).
6. S. I. Oh, N. Rebelo and S. Kobayashi, Finite element formulation for the analysis of plastic deformation of rate sensitive materials in metal forming, *IUTAM Symposium on Metal Forming Plasticity*, p. 273, Tutzing (1978).
7. P. Perzyna, Thermodynamic theory of viscoplasticity, *Advances in Applied Mechanics*, Vol. 11, p. 313, (1971).
8. P. Perzyna and A. Sawczuk, Problems of thermoplasticity. In *Nuclear Engineering and Design*, Vol. 24, p. 1 (1973).
9. E. W. Hart, Constitutive relations for the nonelastic deformation of metals, *Trans. ASME, J. Engr. Mat. Tech.* Vol. 98, p. 193 (1976).
10. E. W. Hart, A phenomenological theory for plastic deformation of polycrystalline metals. *Acta Met.* 18, 599 (1970).
11. E. W. Hart, C. Y. Li, H. Yamada and G. L. Wire, Phenomenological theory: A guide to constitutive relations and fundamental deformation properties. *Constitutive Equations in Plasticity* (Edited by A. S. Argon). M.I.T. Press, Cambridge, Mass. (1975).
12. P. Perzyna, Fundamental problems in viscoplasticity, *Adv. Appl. Mech.* 9, 243 (1966).
13. J. T. Oden, D. R. Bhandari, G. Yagawa and T. J. Chung, A new approach to the finite element formulation and solution of a class of problems in coupled thermoelastoviscoplasticity of crystalline solids. *Nucl. Engng Design*, 24, 420 (1973).
14. W. S. Tseng, Ph.D. Thesis, University of California, Berkeley (1971).
15. J. M. Kelly, Non-linear constitutive relations for plane shock propagation in viscoplastic solids. *Arch. Mech. Stos.* 1, 22 (1970).
16. O. C. Zienkiewicz, *The Finite Element Method*, 3rd Edn. McGraw-Hill, New York (1977).
17. G. Dahlquist and A. Bjorck, *Numerical Methods*. Prentice-Hall, New Jersey (1974).
18. A. Ralston, *A first course in numerical analysis*. McGraw-Hill, New York (1965).
19. R. L. Taylor, *Seminars on Advanced Topics in Finite Elements*. University of California, Berkeley (1979).

12 Int. J. Mech. Sci. Vol. 22, pp. 707–718
Pergamon Press Ltd., 1980. Printed in Great Britain

2.

A COUPLED ANALYSIS OF VISCOPLASTIC DEFORMATION AND HEAT TRANSFER—II

APPLICATIONS

N. REBELO and S. KOBAYASHI
Department of Mechanical Engineering, University of California, Berkeley, CA 94720, U.S.A.

(*Received* 22 *February* 1980)

Summary—The finite element formulations for coupled analysis of deformation and heat transfer are applied to the problems of solid cylinder compression and ring compression. The temperature distributions in solid cylinder compression are compared with experimental data, and the computed results of ring compression of aluminum at elevated temperature are compared with experimental observations as well as with calculated results not including the temperature effects. It is demonstrated that the coupled analysis accurately simulates these processes.

NOTATION

Y	static yield stress
$\dot{\epsilon}$	strain rate
γ, n	material parameters
Y_{T_0}	static yield stress at reference temperature T
Q	material parameter
k	Boltzman constant
T	absolute temperature
$\mathbf{C}$	heat capacity matrix
$\mathbf{K}$	heat conduction matrix
$\mathbf{Q}$	heat flux vector
$\mathbf{T}$	vector of nodal point temperatures
$\dot{\mathbf{T}}$	vector of nodal point temperature rates
$\mathbf{N}$	interpolation function
$\bar{\sigma}\dot{\bar{\epsilon}}$	rate of plastic work
$\nu A\dot{\bar{\epsilon}} - \nu B\alpha\, e^{-D/kT}$	rate of change of dislocation energy
A, B	material constants
α	dislocation density
D	energy for self diffusion
ν	energy per unit length of dislocation
T_e	environment temperature
T_s	surface temperature
T_d	die temperature
T_w	workpiece temperature
σ	Boltzman constant
ϵ	radiation coefficient
h	heat convection coefficient
h_{lub}	heat transfer coefficient from lubricant
q_f	surface heat generation rate due to friction
f	friction force
v_r	relative velocity between the die and the workpiece
H	workpiece height in mm
k_w	heat conductivity—workpiece
k_d	heat conductivity—die
c_w	heat capacity—workpiece
c_d	heat capacity—die
ρ	mass density
n	number of strokes per minute (press)
S	stroke of the press
W	distance from lower position

1. INTRODUCTION

The theory necessary for developing computer simulations of transient viscoplastic metal deformation coupled with a heat transfer analysis has been presented in the companion paper [1].

When deformation takes place at high temperatures, material properties can vary considerably with temperature. During a metalworking process, large nonhomogeneities in deformation and consequently in heat generation, usually occur. Moreover, especially if the dies are at a considerably lower temperature than the workpiece, the heat losses by conduction to the dies and by radiation and convection to the environment contribute to the existence of severe temperature gradients. Thus including temperature effects in the analysis of metal forming problems is very important.

Furthermore, at elevated temperatures plastic deformation can induce phase transformations and alterations in grain structures which in turn will modify the flow resistance of the material as well as other mechanical properties. Including these metallurgical effects in the process analysis contributes significantly to the understanding of material behavior under plastic deformation.

The importance of temperature calculations during a metal forming process has been recognized for a long time. Until recently the majority of the work has been based on procedures that uncouple the problem of heat transfer from the metal deformation problem.

Several research workers have used the approach of determining the flow characteristics of the problem either experimentally or by calculations, and then of using these calculation for the calculation of heat generation. Among these is the work of Johnson and Kudo[2] on extrusion, and Tay, Stevenson and Dans[3] on machining. Another approach uses Bishop's[4] numerical method, in which heat generation and transportation is considered to occur instantaneously for each time step, with conduction taking place during the time step. The new temperature distribution is used to calculate flow characteristics, which in turn will originate the instantaneous heat generation and transportation for the next step. This approach is represented by the work of Altan and Kobayashi[5] on extrusion, Lahoti and Altan[6] on compression and torsion, and Nagpal, Lahoti and Altan[7] on forging. Usually the temperature calculations are done by finite differences, or by finite elements, and the upper bound technique is the most common for determining flow patterns, if not experimental.

As far as we know, a paper by Oden, Bhandary, Yagawa and Chung[8] presents the first coupled analysis of deformation and heat transfer, although the application is to a 3-dimensional rectangular bar, which was constrained on one direction and heated at a corner. The formulation is for elastoviscoplastic materials, and uses the same rational thermodynamics background we have used in the present work.

Zienkiewicz, Onate and Heinrich[9] have made a coupled thermal analysis in extrusion. Because it is a steady state situation, the heat balance equations and equilibrium equations, using rate sensitive materials, are solved simultaneously. Previously Zienkiewicz, Jain and Onate[10] had proposed to solve the same problem by separating the equations, and iterating the results between the two sets of solutions.

The purpose of this paper is to show the results of calculations by applying the formulation developed in [1] to metal forming problems, which demonstrate temperature effects clearly, and to show the potential for further refinements. A brief discussion of the basic finite element equations is presented, in which some details of the treatment of boundary conditions crucial for the algorithm are given.

The compression of a solid cylinder of AISI 1015 is analyzed and compared with experimental data obtained by Pohl[11]. Also, the computed results of the forging of an aluminum 1100 ring at 400°C are compared with the one studied in [7] as well as with calculations not including the temperature effects[12].

2. BASIC EQUATIONS

The finite element equations resulting from discretizing weak forms of equilibrium equations and heat balance equations are described in the literature. We discuss here only the details that are important in the implementation of the algorithm presented in the companion paper.

As far as equilibrium equations are concerned, the only modification of the analysis of Oh, Rebelo and Kobayashi[12] is the temperature dependence of the flow stress. Recall that experimental data on flow stress has been fitted by the expression of the form

$$\sigma = Y\left[1 + \left(\frac{\dot{\varepsilon}}{\gamma}\right)^{n}\right], \tag{1}$$

and that Y, n, γ are functions of strain and temperature. For the range of temperature variations in the metal forming problems, and within the accuracy of data available, equation (1) can be expressed as

$$\sigma = Y_{T_0} \frac{e^{\Omega_0 T}}{e^{\Omega_0 T_0}} \left[1 + \left(\frac{\dot{\varepsilon}}{\gamma}\right)^n\right], \tag{2}$$

Y_{T_0}, n and γ, functions of strain.

The friction factor is defined as the ratio between the frictional shear stress and the rate and temperature dependent yield stress.

For heat balance equations, we recall again that there are of the form (see E.G.[13]);

$$C\dot{\mathbf{T}} - K\mathbf{T} = \mathbf{Q}, \tag{3}$$

where the heat flux vector Q has several components (see [1]);

$$\begin{aligned}\mathbf{Q} = &\int_v (\bar{\sigma}\dot{\bar{\varepsilon}} - \nu A\dot{\varepsilon} + \nu B a\, e^{-(\Omega/RT)})\mathbf{N}\, dV + \int_{S_r} \sigma\epsilon (T_r^4 - T_i^4)\mathbf{N}\, dS_r \\ &+ \int_{S_r} h(T_r - T_i)\mathbf{N}\, dS_r + \int_{S_i} h_{int}(T_d - T_w)\mathbf{N}\, dS_i \\ &+ \int_{S_i} q_f \mathbf{N}\, dS_i.\end{aligned} \tag{4}$$

The first component is the contribution of the net heat generated inside the deforming body, the second one the contribution of the heat radiated into the body, and the third, the contribution of the heat transferred by convection. The fourth term represents the contribution of the heat transferred between workpiece and die through their interface (with or without lubricant), and the last term is the contribution of the heat generated by friction between die and workpiece.

The following remarks pertain to the implementation of the algorithm previously described.

We treat the workpiece and the die separately. In this way, we greatly reduce the number of equations to be solved simultaneously, which in turn reduces the cost of the solution. In the die there is no internal heat generation and no deformation calculations are necessary (rigid dies). Because of the heat transfer at the interface, the die and the workpiece equations contain temperatures of each other, and the solution is found iteratively. For two reasons, this brings no increase in cost: first, iterations with respect to the velocity have to be done anyway; and second, matrices do not have to be recalculated at each iteration, as only the heat-flux vector changes.

In a numerical testing of heat transfer calculations, it was found that lubricant heat transfer coefficients at least one order of magnitude higher than the real ones were necessary to produce instability.

The heat generated through friction, and calculated by

$$q_f = |f| \cdot |v_r|,$$

was evenly distributed between the die and the workpiece.

The die had to be remeshed at each time step, in order to make the nodes at the interface match. Again, numerical testings were made with similar mesh changes in a heat transfer problem whose exact solution is known, and the error in temperatures so introduced was very small.

The temperature values used in the internal heat generation and radiation terms of heat flux are at all times those values from the previous iterations.

Dislocation density calculations, made only in the workpiece, represent a minute fraction of operations, because no coupling was considered from element to element. For each element the scalar version of the time integration scheme described for temperatures was used.

3. COMPRESSION OF A CYLINDER OF AISI 1015 AT ROOM TEMPERATURE

Pohl[11] conducted temperature measurements in order to test his uncoupled analysis, in which approximate stream functions were used for the deformation, and finite differences for the heat balance. A solid cylinder of a carbon steel AISI 1015 was compressed between flat dies at room temperature. Thermocouples were inserted in the cylinder at different locations. Upon deformation, their readings indicated the temperature increases due to the heat generated, but no assessment was made with respect to the accuracy obtained in such measurements. Nevertheless, this is one of few cases in the literature where actual temperature distributions were reported.

Fig. 1 shows the dimensions and locations of measuring points.

Although the values of some parameters must be "guessed" in computation, the results of our analysis are compared with those measurements.

The conditions used in the computation are as follows.

The deformation took place at initial room temperature, up to a height reduction of 1/3. The finite element grid was composed of 132 four node quadilateral elements in the workpiece, and 119 in the die. Because of symmetry, only one fourth of the cylinder needed to be analyzed. The friction factor was taken as 0·65.

In order to simulate a mechanical press, the die velocity was changed at each time step according to the expression

$$v = 12 * \sqrt{(H\text{-}20)}\ \text{mm/s}.$$

Each step corresponded to 1% in height reduction, which was equivalent to time steps of up to 0·03 sec.

In this case the flow stress was taken independently of strain rate and temperature. This is justifiable for

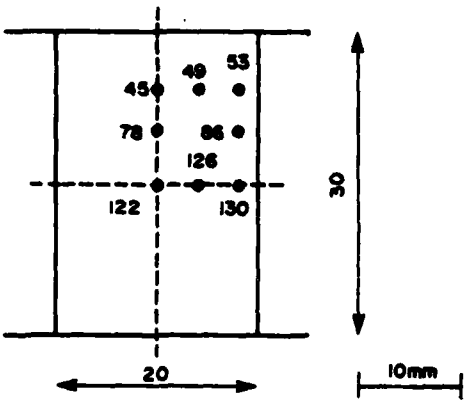

INITIAL LOCATION		
POINT	R_0 mm	Z_0 mm
45	0.0	9.55
78	0.0	5.45
122	0.0	0.0
49	4.0	9.55
126	4.0	0.0
53	8.0	9.55
86	8.0	0.0

FIG. 1. Specimen dimensions. Die dimensions. Locations of temperature measurements[11].

steel being deformed at room temperature. The flow stress values, as given by Pohl, were

$$\sigma = 275 \text{ N/mm} \qquad \epsilon < 0{\cdot}02512$$
$$\sigma = 722 * \epsilon^{0{\cdot}262} \text{ N/mm} \qquad \epsilon \geq 0{\cdot}02512.$$

The heat transfer characteristics, other than the thermal conductivity and heat capacity of AISI 1015 measured by Pohl, are taken from handbooks;

$$k_w = 36 \text{ N/s °K}$$
$$\rho c_w = 3{\cdot}77 \text{ N/mm}^2 \text{ °K}$$
$$k_d = 19 \text{ N/s °K}$$
$$\rho c_d = 3{\cdot}77 \text{ N/mm}^2 \text{ °K}$$
$$\sigma\varepsilon = 85 * 10^{-13} \text{ N/mms (°K)}^4$$
$$h = 0{\cdot}00295 \text{ N/s mm °K}$$
$$h_{insb} = 4 \text{ N/S mm °K}.$$

The dimensions of the die are such that at the outside boundaries a constant temperature is imposed.

The material was given an initial dislocation density of $10^6/\text{mm}^2$, and constants A, B, ν and D were chosen in such a way that practically no annihilation occurs (room temperature), and the density grows with strain to an order of $10^{10}/\text{mm}^2$ at a strain of about 50%

$$A = 125 * 10^8/\text{mm}^2$$
$$B = 155 * 10^3/\text{s}$$
$$D/k = 17000 \text{ °K}$$
$$\nu = 317 * 10^{-11} \text{ N mm/mm}.$$

Fig. 2 shows the initial finite element layout, and Fig. 3 shows how it deformed after 1/3 reduction in height. The barreling and the nearly sticking situation along the interface should be noted.

In Fig. 4 the effective strain distribution is shown, which points out the nonuniformity in deformation. The most deformed zone is the outside corner, and shear band formation is clearly seen. As expected, the zone under the die shows little deformation.

Temperature contours in both workpiece and die are presented in Fig. 5. In the workpiece the temperature distribution has a similar pattern to that of effective strain distribution. Since the initial temperatures were the same for die and workpiece, and equal to room temperature, internal heat generation is clearly the prevailing factor in modifying temperatures. The temperature distribution in the die shows well that the most deformed zone was the largest source of heat.

The temperature values measured by Pohl are compared with the calculated values in Figs. 6–8.

The agreements are excellent for the inner points, as seen in Figs. 6 and 7. For the most outer points, however, the computed results indicate that the temperature difference for the three points is minor, while experiments show more difference. Nevertheless, this difference does not seem to negate the analysis technique, as the heat conduction part of the program has been tested with accurate results and the accuracy of the finite element deformation analysis has been well established.

The discrepancies seen in Fig. 8 can be attributed to possible inappropriate material constants and experimental inaccuracies.

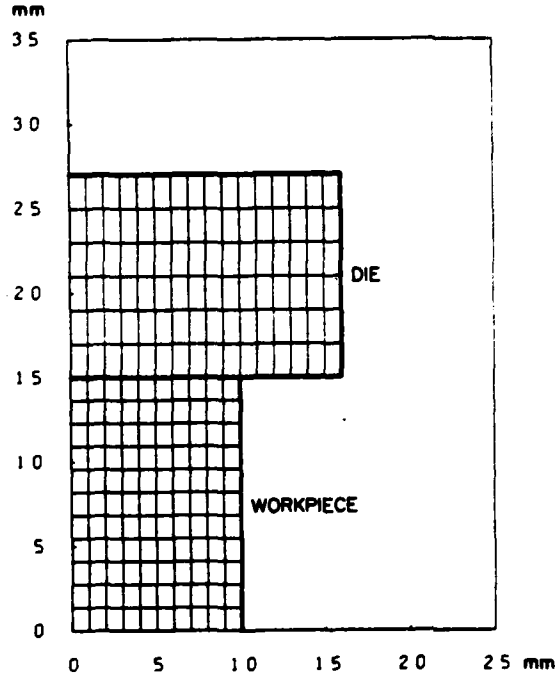

FIG. 2. Finite element layout for AISI 1015 steel cylinder compression.

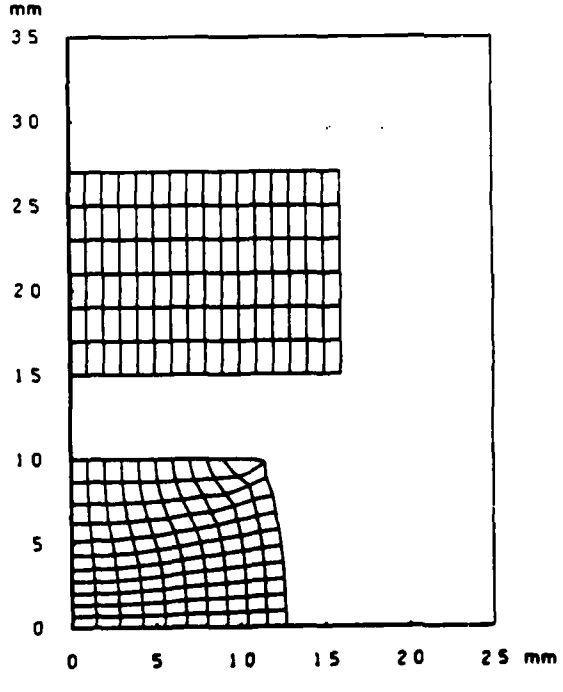

FIG. 3. Distorted grid pattern after 1/3 reduction in height.

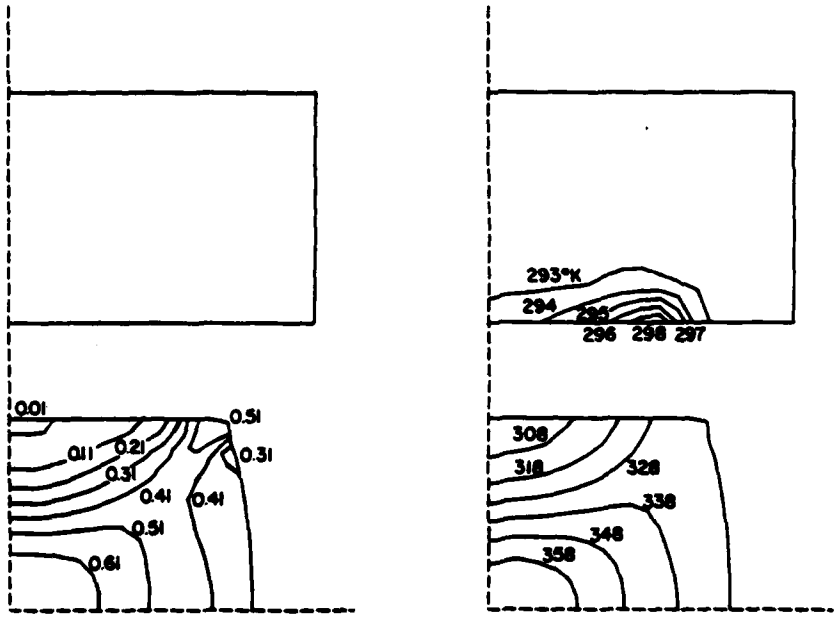

FIG. 4. FIG. 5.

FIG. 4. Effective strain distribution after 1/3 reduction in height.

FIG. 5. Temperature distribution after 1/3 reduction in height.

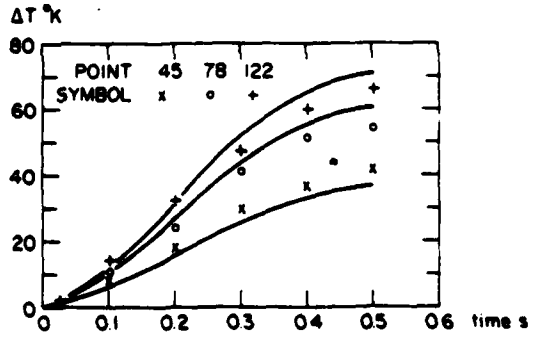

FIG. 6. Comparison of temperature distribution between theory (—) and experiments (×, O, +).

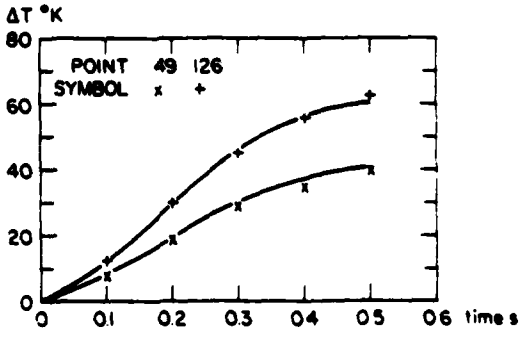

FIG. 7. Comparison of temperature distribution between theory (–) and experiment (×, +).

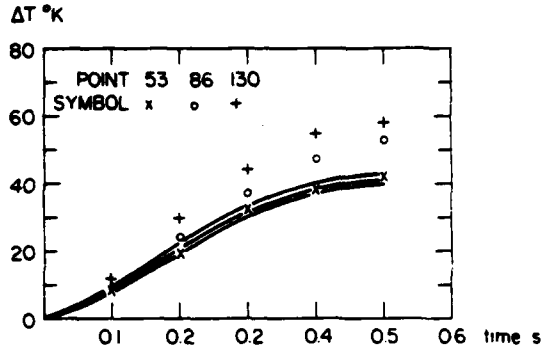

FIG. 8. Comparison of temperature distribution between theory (—) and experiment (×, O, +).

4. COMPRESSION OF A RING OF ALUMINUM 1100 AT HIGH TEMPERATURE

Complete finite element solutions for ring compression of rigid plastic materials have been obtained by Chen and Kobayashi[14]. In [12] they were extended to rate-sensitive materials. The purpose of analyzing the problem with temperature effects is twofold; to compare calculations with some experimental measurements of Nagpal, Lahoti and Altan[7] and to compare them with our previous results without temperature effects. The success of the analysis makes it possible to extend the ring compression test to quantitative lubricant evaluation in the hot forming range.

The rings tested have a o.d.:i.d.:height ratio of 6:3:2, and an outer diameter of 54 mm.

As both dies and workpiece had their surfaces cleaned, and no lubricant was used, the friction factor was taken as 1·0. The dies were initially at room temperature, and the rings were heated to 427°C (800°F).

Total reduction in height was 50%, and the calculations were performed in steps of 1% deformation each. The equivalent time steps did not exceed 0·003 sec. Assuming symmetry, one quarter of the ring was analyzed and 104 4-node quadrilateral elements were placed in the ring and 150 in the die. Fig. 9 shows the initial grid layout as well as the dimensions.

In order to simulate a mechanical press, the instantaneous velocities of the die were obtained from the expression[15];

$$v = 0{\cdot}1 * n * \sqrt{(S * W - W^2)} \text{ mm/s}$$
$$n = 90$$
$$S = 254\ mm$$
$$W = 9 \text{ mm initially.}$$

Flow stress expressions for Aluminum 1100 were derived from experimental data of Lindholm[16] and Altan and Boulger[17]. The expressions in Table 1 correspond to a reference temperature of 400°C to which the following factors in equation (2) were applied

$$e^{Q/kT_0} = 3{\cdot}55$$
$$Q/k = 852{\cdot}6855°\text{K}.$$

TABLE 1. STRESS-STRAIN STRAIN-RATE PROPERTIES OF Al 1100 AT 400°C USED IN CALCULATIONS

ϵ	0·05	0·10	0·15	0·25	0·50	0·70
n	0·346	0·226	0·200	0.419	0·507	0·502
Y^n	7·908	3·936	4·162	4·228	5·060	4·509
Y	$2 + 10{\cdot}86\epsilon - 29{\cdot}84\epsilon^2 + 12{\cdot}7\epsilon^3$			$3 + 2{\cdot}765(\epsilon - 0{\cdot}15) - 5{\cdot}98(\epsilon - 0{\cdot}15)^2 + 13{\cdot}866(\epsilon - 0{\cdot}15)^3$		3·4

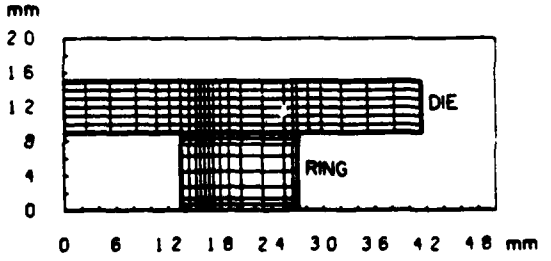

FIG. 9. Initial mesh for Al 1100 ring compression.

The heat transfer characteristics were taken from standard handbooks.

$$k_w = 242 \text{ N/s °K}$$
$$\rho c_w = 2{\cdot}4255 \text{ N/mm}^2 \text{ °K}$$
$$k_d = 19 \text{ N/s °K}$$
$$\rho c_d = 3{\cdot}77 \text{ N/mm}^2 \text{ °K}$$
$$\sigma\varepsilon = 85 * 10^{-13} \text{ N/mm s °K}^4$$
$$h = 0{\cdot}007 \text{ N/s mm °K}$$
$$h_{tub} = 35 \text{ N/s mm °K}.$$

As Fig. 9 shows, the outer boundaries of the die are sufficiently far from the interface so that a constant temperature is imposed on them.

The dislocation data utilized were prepared under two basic assumptions. First, if there were no annihilation, dislocation density would grow from, say, 10^4/mm² in the annealed state to 10^9/mm² at an effective strain of 50%. Second, because of annihilation at high temperatures and in a relatively fast process, dislocation density will not grow above 10^9/mm². The values used are

$$A = 2 * 10^9/\text{mm}^2$$
$$B = 1{\cdot}1 * 10^{14}/\text{s}$$
$$D/k = 17000 \text{ °K}$$
$$\nu = 105 * 10^{11} \text{ N mm/mm}.$$

In deformation calculations an average of 12 iterations were needed for convergence, and up to 3 more for temperatures. Whenever a node on the surface touched the die, convergence was much much slower and up to 30 iterations were then needed.

Fig. 10 compares the decrease in inner diameter vs reduction in height obtained in the present calculations with the experimental point of Nagpal *et al.* and with the previous solutions not including temperature effects. When the effect of temperature is included, the effect of chilling by the dies causes relatively small sliding along the interface and results in more decrease in inner diameter than the case without temperature effect.

Fig. 11 shows the ring profiles after 48·5% reduction. The agreement is excellent between computed and experimental profiles.

Grid distortions, indicating the flow of material after 20 and 50% reduction, are presented in Figs. 12(a) and 13(a). The neutral zone is distinctively traceable, and the large amounts of folding are evident. Their equivalent effective strain distributions, clearly showing the nonuniform deformation, are given in Figs. 14(a) and 15(a). The most deformed areas are the original corners in contact with the die, and the least deforming regions are noticeable near the neutral axis. A comparison with equivalent figures (12(b)–15(b)) for the temperature-independent calculations in similar conditions indicates a more severe distortion in the temperature dependent case, and demonstrates how the die-chilling effect concentrates the deformation on the equatorial regions, which are the hottest and least resistant to flow.

A characteristic behavior of calculated dislocation densities is that they increase sharply during the first 5% of deformation, to values from 10^6/mm² up to $5 * 10^7$/mm². At this point the elements at higher temperatures begin to have negative rates, while the ones near the die keep increasing their densities. At 25% deformation the highest value of $1{\cdot}2 * 10^8$/mm² is reached, in the upper right corner element. By that time the great majority of elements have densities between 1 and $3 * 10^7$/mm², although some are increasing and others decreasing. When 46% deformation is reached, all elements start to have negative rates of dislocation density. This means that the density values reached are high enough to induce strong annihilation, even in the colder zones near the die. The average values at this stage are in the 10^8/mm² order of magnitude for the hotter zones, and the 10^7/mm² order of magnitude for the colder zones.

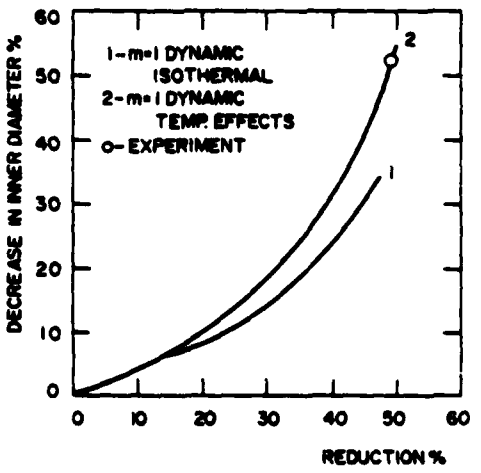

FIG. 10. Change or ring inner diameter as functions of reduction in height.

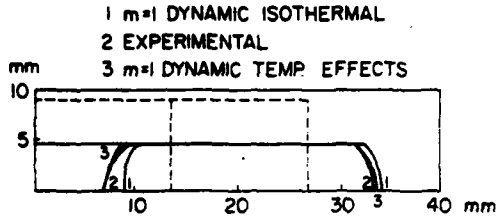

FIG. 11. Deformed ring profiles.

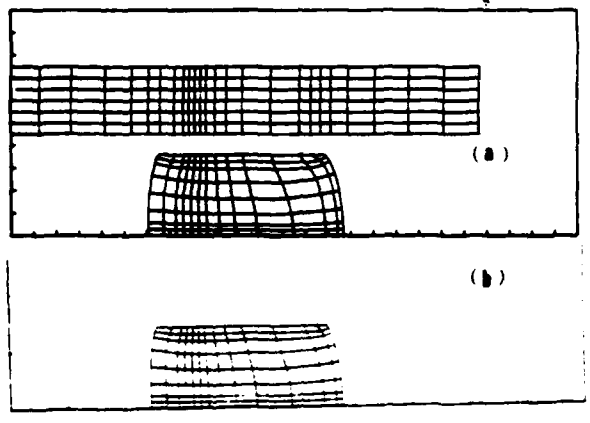

FIG. 12. Grid distortions of Al 1100 ring at 20% reduction in height (a) with temperature effect and (b) without temperature effect.

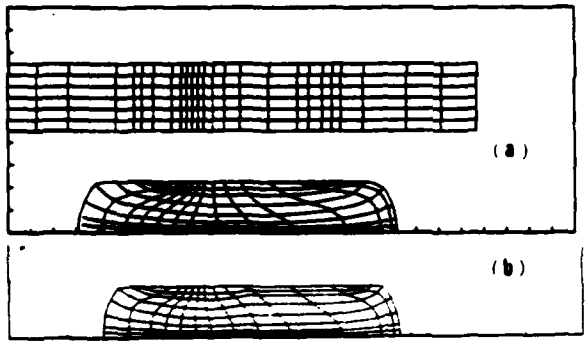

FIG. 13. Grid distortions of Al 1100 ring at 50% reduction in height (a) with temperature effect and (b) without temperature effect.

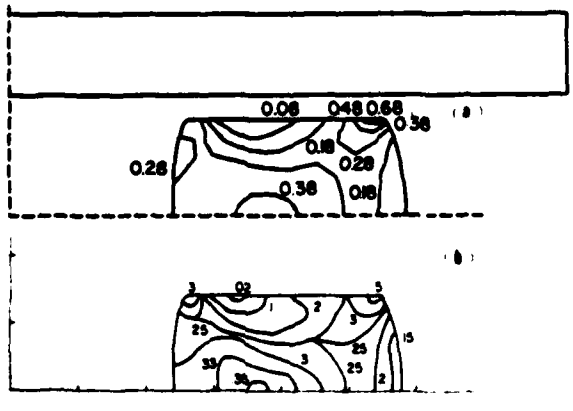

FIG. 14. Strain distributions of Al 1100 ring at 20% reduction in height (a) with temperature effect and (b) without temperature effect.

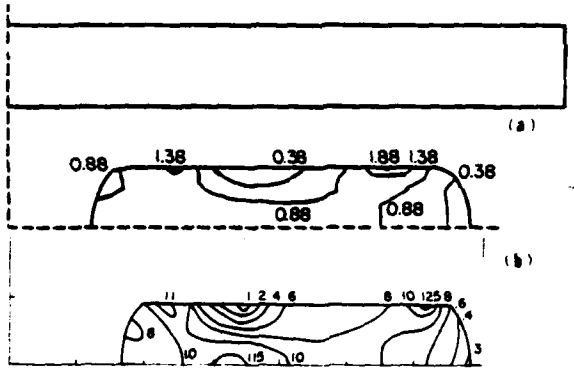

FIG. 15. Strain distribution of Al 1100 ring at 50% reduction in height (a) with temperature effect and (b) without temperature effect.

We chose the material constants for the dislocation density calculations, having in mind that in overall deformation the energy spent with the creation of dislocations is around 10% of the total deformation energy. The results discussed above show that the former energy is mostly spent in the early stages of deformation, and that towards the end, annihilation is helping plastic work to supply heat generation throughout the body.

In Figs. 16 and 17 temperature contours in both ring and die are presented. The temperature field is dominated by the heat flow from the workpiece to the die, and only near the equator temperatures rise slightly. Temperature differences across the workpiece die interface decrease from 407 K initially, to around 220 K at the end of deformation.

An appraisal of influence of parameters in the temperature calculations was done by roughly calculating heat fluxes in 1 radian section for a typical step of deformation, and comparing them to heat generation;

radiated heat ~ 350 Nmm/s
convected heat ~ 500 Nmm/s
heat lost to die ~ 6500000 Nmm/s
heat generated ~ 1000000 Nmm/s

this indicates that heat generation and conduction to the die govern the whole heat balance process.

In Fig. 18 the load displacement curve is compared to the previously calculated one not including temperature effects. During the initial stages of deformation the values are similar, due to the fact that in

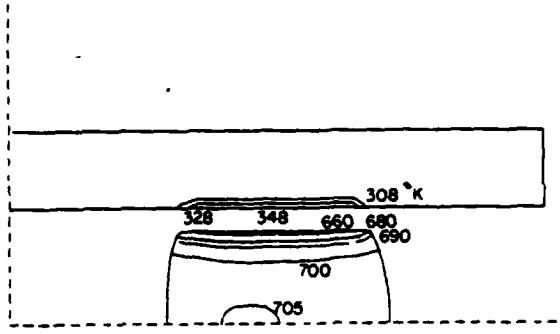

FIG. 16. Temperature contours at 20% reduction in height in Al 1100 ring compression.

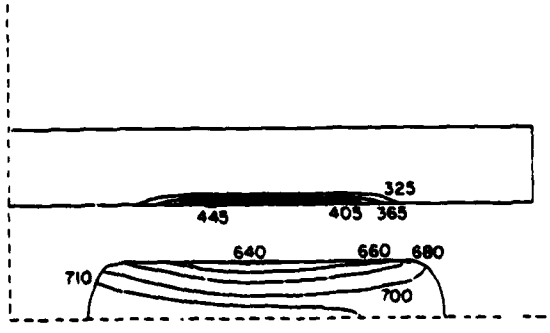

FIG. 17. Temperature contours at 50% reduction in height in Al 1100 ring compression.

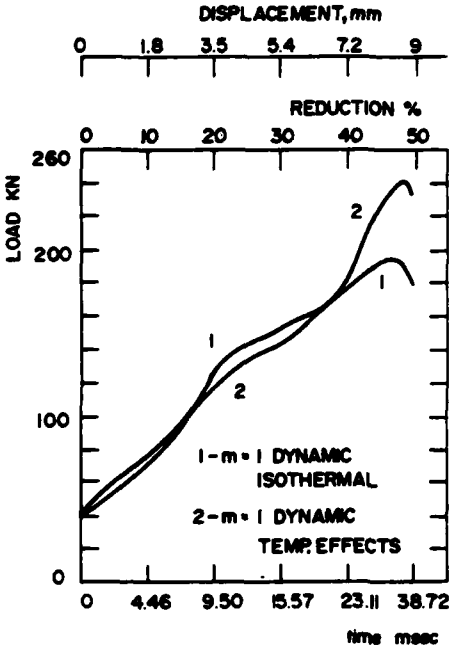

FIG. 18. Load displacement curves for Al 1100 ring compression.

the temperature independent calculations the flow stress used referred to a temperature similar to the initial one in the temperature dependent case. As deformation proceeds, the zones near the die cool down and the equatorial zones heat up. Since deformation occurs mainly in the latter, the lower flow stress here induces a lower total load necessary for deformation.

The decrease in load towards the end is a result of the rapid decrease in velocity of the die, and the subsequent strain rate effects.

5. CONCLUDING REMARKS

The capabilities of a coupled thermoviscoplastic analysis of non-steady-state metal forming processes have been demonstrated in this paper. The finite element analysis of deformation and heat transfer is a significant extension to the analysis of warm and hot forming processes. It produces accurate simulations of the processes and provides insight into the governing parameters in the process.

A higher level of sophistication in the analysis is invariably associated with a higher level of sophistication in the input data necessary. At this stage much work is still needed in order to utilize all the capabilities of the method. It is hoped that in the future the important internal parameters will be screened from the superfluous, and programs to quantify their importance will be set.

Acknowledgements—The authors wish to thank the Battelle Columbus Laboratories for the contract S-2935 (7128) and the Army Research Office for the contract DAAG29-79-C-0217 under which the present work was possible. They also wish to thank Ms Katie Triest for editing the manuscript.

REFERENCES

1. N. REBELO and S. KOBAYASHI, A coupled analysis of viscoplastic deformation and heat transfer—I. Theoretical considerations. *Int. J. Mech. Sci.* **22**, 11 (1980).
2. W. JOHNSON and H. KUDO, The use of upper-bound solutions for the determination of temperature distributions in fast hot rolling and axisymmetric extrusion processes. *J. Mech. Sci.* 1, 175 (1960).
3. A. O. TAY, M. G. STEVENSON and G. V. DAVIS, Using the finite element method to determine temperature distributions in orthogonal machining. *Proc. Inst. Mech. Engineers* **188**(55/74), 627 (1974).
4. J. F. W. BISHOP, An approximate method for determining the temperatures reached in steady-state motion problems of plane plastic strain. *Q. J. Mech. Appl. Math.* **9**, 239 (1956).
5. T. ALTAN and S. KOBAYASHI, A numerical method for estimating the temperature distributions in extrusion through conical dies. *J. Engng Indust. Trans. ASME* **90**, 107 (1968).
6. G. LAHOTI and T. ALTAN, Prediction of temperature distributions in axisymmetric compression and torsion. *J. Engng Materials Technol. Trans. ASME*, **97**, 113 (1975).

7. V. NAGPAL, G. D. LAHOTI and T. ALTAN, A numerical method for simultaneous prediction of metal flow and temperatures in upset forging of rings. *ASME Paper No. 77-WA/PROD-35* (1977).
8. J. T. ODEN, D. R. BHANDARI, G. YAGAWA and T. J. CHUNG, A new approach to the finite element formulation and solution of a class of problems in coupled thermoelastovisco-plasticity of crystalline solids. *Nucl. Engng Des.* **24**, 420 (1973).
9. O. C. ZIENKIEWICZ, E. ONATE and J. C. HEINRICH, Plastic flow in metal forming—I. Coupled thermal behaviour in extrusion—II. Thin sheet forming. *Appl. Numer. Meth. Forming Proc. ASME AMD* **28** (1978).
10. O. C. ZIENKIEWICZ, P. C. JAIN and E. ONATE, Flow of solids during forming and extrusion: Some aspects of numerical solutions. *Int. J. Sol. Struct.* **14**, 15 (1978).
11. W. POHL, A methof for approximate calculation of heat generation and transfer in cold upsetting of metals. Doctoral Dissertation, University of Stuttgart (1972).
12. S. I. OH, N. REBELO and S. KOBAYASHI, Finite element formulation for the analysis of plastic deformation of rate sensitive materials in metal forming. *IUTAM Symposium on Metal Forming Plasticity*, p. 273. Tutzing (1978).
13. O. C. ZIENKIEWICZ, *The Finite Element Method*, 3rd. Edn. McGraw-Hill, New York (1977).
14. C. C. CHEN and S. KOBAYASHI, Rigid-plastic finite element analysis of ring compression. *Applications of numerical Methods to Forming Processes, ASME, AMD* **28**, 163 (1978).
15. T. ALTAN, Forging equipment, materials and practices. Metals and Ceramics Information Center, Battelle Columbus Laboratories (1973).
16. U. S. LINDHOLM, Experiments in dynamic plasticity. *Symposium on Mechanical Behaviour of Materials Under Dynamic Loads*, San Antonio, Texas (1968).
17. T. ALTAN and F. W. BOULGER, Flow stress of metals and its application in metal forming analysis. *J. Engng Indust.* **95**, 1009 (1973).

THE AMERICAN SOCIETY OF MECHANICAL ENGINEERS
345 E. 47 St., New York, N.Y. 10017

82-Prod-14

24 # 3.

24

An Investigation of the Shell Nosing Process by the Finite-Element Method. Part 1: Nosing at Room Temperature (Cold Nosing)

Ming-Ching Tang
IBM, San Jose, Calif.

Shiro Kobayashi
Professor,
Department of Mechanical Engineering,
University of California,
Berkeley, Calif.
Fellow ASME

The metal-forming process of shell nosing at room temperature was analyzed by the finite-element method. The strain-rate effects on materials properties were included in the analysis. In cold nosing simulations; the nine-node quadrilateral elements with quadratic velocity distribution were used for the workpiece. The treatment of a moving boundary in the analysis of nosing is discussed and successfully implemented in the finite-element program. FEM simulations of 105-mm dia. shells of AISI 1018 steel and aluminum 2024 were performed and solutions were obtained in terms of load-displacement curves, thickness distribution, elongation, and strain distributions. Comparisons with experimental data show very good agreement.

Introduction

Shell nosing refers to the process of forming an ogive nose at the end of a tubular part by pressing the tube into a suitably formed die (Fig. 1). The flow of metal in nosing is very complex and only a slight variation in friction or temperature conditions may result in a misformed shell due to improper metal flow. Understanding the deformation mechanics of a metal-forming process is an essential and important step towards the control of metal flow, and, subsequently, the design of the forming process. Experimental characterizations of process parameters involve trial and error, and it is difficult to separate the influence of individual parameters upon each other. It is desirable and necessary to use an inexpensive analytical simulation method in order to improve industrial productivity.

Successful efforts have been carried out by Kobayashi and co-workers [1-4] using the finite-element method in analyzing various metal-working processes, such as compression, heading, piercing, and extrusion. The objective of the present investigation is to develop the finite-element simulation technique, including flow stress dependence on strain rates, for the shell nosing process.

The flow of metal in the nosing process is affected by the characteristics of the lubricant and the speed of the nosing operation. If the lubrication is not sufficient and if the nosing process is slow, the lubricant is squeezed out and the friction

Contributed by the Production Engineering Division for presentation at the Design and Production Engineering Technical Conference, Washington, D.C., September 12-15, 1982 of THE AMERICAN SOCIETY OF MECHANICAL ENGINEERS. Manuscript received by the Production Engineering Division February 8, 1982. Paper No. 82-Prod-14.
Copies will be available until June 1983.

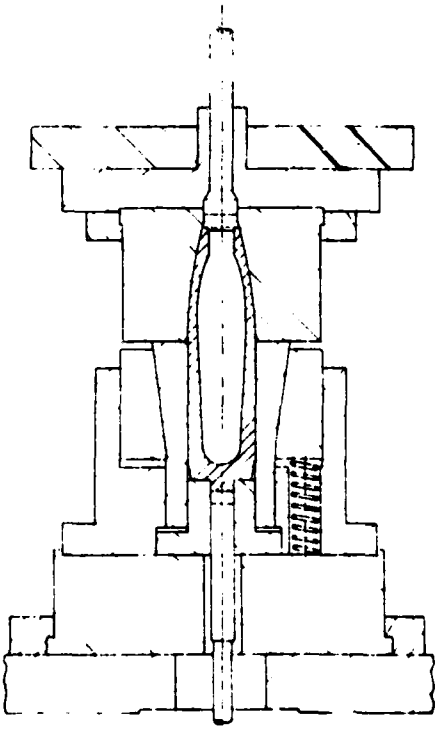

Fig. 1 Shell nosing process (from reference [6])

25

between shell and die tends to shorten the shell. On the other hand, if the lubrication is good and if the nosing proceeds rapidly, the lubricant is squeezed out to a lesser extent. Therefore, the friction is reduced and the shell is lengthened.

Small caliber shells (up to 105 mm) can be cold nosed, while larger shells (155 mm and up) are hot nosed. In cold nosing, the entire shell is initially maintained at a constant temperature and the flow stress is uniform. The deformation work-hardens the shell material nonuniformly, and the resistance to further deformation by various parts of the shell is unequal. The elastic spring back is very small compared to plastic strain; therefore, the dies are given the shape of the rough-finished nose. The slight elastic back spring is removed in the process of finish turning.

In 1943 Nadai [5] conducted, for the ASME Special Research Committee on Forging of Steel Shells, an extensive theoretical investigation on the forces required in nosing of shells. This work is basically an extension of the theory of curved shells to cover cases in which the metal is in a plastic state of equilibrium. The approximation is based upon constant coefficient of friction and ignores variations in the flow stress of the shell material. Onat and Prager [6] extended Nadai's work to include the changes in the shell wall thickness due to the nosing operation. They investigated the influence of these changes on the stresses in nosing. Cruden and Thompson [7] conducted an experimental study of the nosing process to establish the limitations of the process and to assess the effects of the various process parameters. Recently, the metal flow in nosing of shells was analyzed, using Hill's general method of analysis, by Lahoti and Altan [8].

In the present study of cold nosing operation, the rigid-viscoplastic finite-element method is used for the analysis, with reference to the effects of friction. Simulation of 105-mm shell nosing for AISI 1018 steel is performed, and solutions are compared with available experimental data from Battelle Columbus Laboratories [9]. The experiments of shell nosing of aluminum alloy 2024 were conducted and an extensive comparison was made between the computer simulation and experiments.

Finite-Element Method

General theories about the finite-element method have been well described in many books. Therefore, only a brief description of the method that is necessary for the discussion of the features involved is given here. Detail formulations and computer programs for the analysis can be found in reference [10].

For an incompressible, rigid-viscoplastic material, the variational formulation in boundary value problems is given by

$$\int_V \sigma'_{ij}\delta\dot{\epsilon}_{ij}dV - \int_{S_F} F_i\delta u_i dS_F + \int_V \lambda\delta\dot{\epsilon}_{ii}dV + \int_V \dot{\epsilon}_{ii}\delta\lambda dV = 0 \quad (1)$$

In equation (1), σ'_{ij} is the deviator stress, $\dot{\epsilon}_{ij}$ is the strain rate, F_i is the traction prescribed over the surface S_F, u_i is the velocity, and λ is the Lagrange multiplier.

Constitutive equations for viscoplastic materials are expressed by

$$\sigma'_{ij} = \frac{2}{3}\frac{\bar{\sigma}}{\dot{\bar{\epsilon}}}\dot{\epsilon}_{ij} \quad (2)$$

where $\bar{\sigma}$ is the effective stress which is a function of strain and strain rate, and $\dot{\bar{\epsilon}}$ is the effective strain rate.

Discretization of equation (1) is performed by using nine-node isoparametric elements for the axisymmetric deformation problem. Applying the arbitrariness of the variations of the nodal point velocity vector v and the element Lagrange multiplier λ, the system of equations is obtained in the form of

$$\mathbf{f}(\mathbf{v},\lambda) = 0 \quad (3)$$

Equations (3) are nonlinear in v and linear in λ. To solve these nonlinear equations, the Newton-Raphson iterative method was used. Expanding equations (3) into Taylor's series and maintaining only the first two terms,

$$\mathbf{f}(\mathbf{v}_n,\lambda) + \frac{\partial \mathbf{f}}{\partial \mathbf{v}}(\mathbf{v}_n,\lambda)\Delta\mathbf{v}_n = 0 \quad (4)$$

which results in the system of equation linear in Δv and λ. In equation (4), $\mathbf{v}_n$ represents the input values from the previous solution and $\Delta\mathbf{v}_n$ represents the correction values obtained from the present iteration. After each iteration, the values of v are updated as $\mathbf{v}_{n+1} = \mathbf{v}_n + \alpha\Delta\mathbf{v}_n$, where α is a deceleration coefficient. For solution convergence, two measures, namely, the error norm of the velocities and the norm of the residual equation (3), are used as criteria.

The constitutive equation (2) becomes undetermined at zero strain rate. Whenever some regions in a nonuniform deformation process become rigid, the system of equations becomes very ill conditioned. To avoid this, a strain rate offset $\dot{\epsilon}_0$ is introduced such that the stress drops linearly to zero when the strain state is below $\dot{\epsilon}_0$. This offset value is chosen only for numerical reasons. Values of two orders of magnitude smaller than an average strain rate in the deformation have given successful results [11].

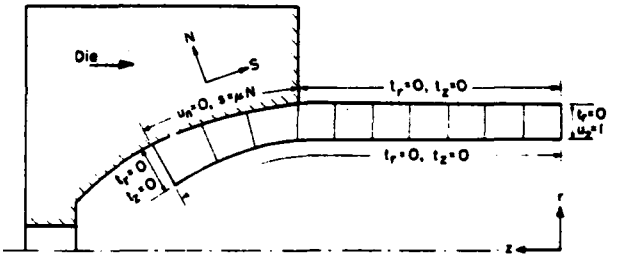

Fig. 2 Mesh system and boundary conditions

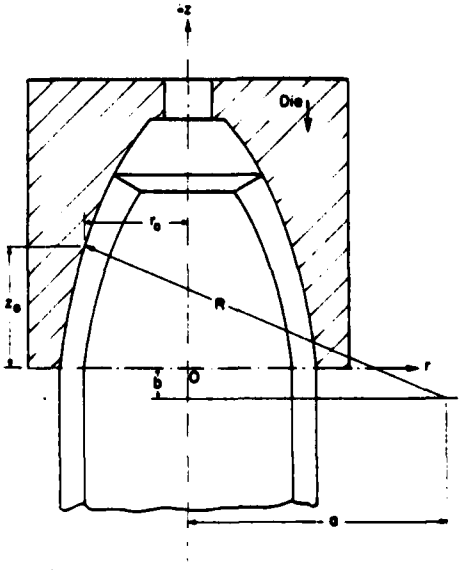

Fig. 3 Configuration of shell during nosing

26

Table 1 Dimension of 105-mm shell

Outside diameter at the nose base	108 mm
Radius of curvature of the nose ogive	650 mm
Initial wall thickness of the preform	12 mm
Axial length of the nose portion	150 mm
Distance of the ogive center from nose base	25 mm

Computational Procedures

In applying the finite-element method to shell nosing, some thought should be given to the implementation of boundary conditions. Figure 2 shows the boundary conditions and the mesh that was used in the calculations. Once the nosing process begins, the top portion of the tube enters the die zone. The boundary conditions in the contact region are stated not only by prescribing tractions and incremental displacements, but by their ratios. The radial and axial velocities of the material nodes in the contact region are not independent, and they are related to each other through a mathematical expression for the geometrical requirement that they must be actually on the surface of the die. The expression is

$$(r_0+a)^2+(z_0+b)^2=(r_0+\Delta r+a)^2+(z_0+\Delta z+b)^2=R^2, \quad (5)$$

where r_0, z_0 are radial and axial positions of the node at the present configuration at time t_0, and Δr, Δz are the increments of radial and axial displacements. R is the radius of curvature of the nose ogive. See Fig. 3.

Rewriting Δr and Δz in terms of velocities u_r and u_z as $\Delta r = u_r \Delta t$ and $\Delta z = u_z \Delta t$, and linearizing, equation (5) results in the boundary condition given by

$$\Delta u_r = \frac{\Delta u_z}{\alpha} + \beta \quad (6)$$

where

$$\alpha = -\frac{(r_0+a)+u_r\Delta t}{(z+b)+u_z\Delta t} = \frac{1}{\tan\theta},$$

$$\beta = -\frac{[2(r_0+a)u_r+u_r^2+\Delta t+2(z_0+b)u_z+u_z^2\Delta t]}{2[(r_0+a)+u_r\Delta t]}. \quad (7)$$

Coulomb friction is assumed to be operative between workpiece and die. First, we prescribe a tangential friction force S and obtain a converged solution. Then, we compute the generalized nodal forces. With angle α defined in equation (7), we then are able to compute the normal component N and the friction coefficient $\mu = S/N$ corresponding to the initially prescribed value of S. If the computed friction coefficient is not what is intended, we then modify the friction force S and repeat the computational procedure.

Simulation of Cold Nosing of 105-mm Shell of AISI 1018 Steel

In order to illustrate the application of the FEM analysis, simulations were made for cold nosing of a 105-mm shell. Some cold nosing experiments were conducted at the Battelle Columbus Laboratories [9], and the dimensions were selected from these experiments, as shown in Table 1. The specimens were cut from AISI 1018 mild steel tubing, and its flow stress was determined at Battelle by conducting uniform compression tests. The actual true stress versus true strain curve ($\bar{\sigma}$ – $\bar{\varepsilon}$) is given approximately by the expression

$$\bar{\sigma}=37.0(1+50\bar{\varepsilon})^{0.264} \quad (8)$$

where $\bar{\sigma}$ is the flow stress at an effective strain $\bar{\varepsilon}$. In the computer program, we have constitutive relationship of the form

$$\bar{\sigma}=Y\left[1+\left(\frac{\dot{\bar{\varepsilon}}}{\gamma}\right)^n\right] \quad (9)$$

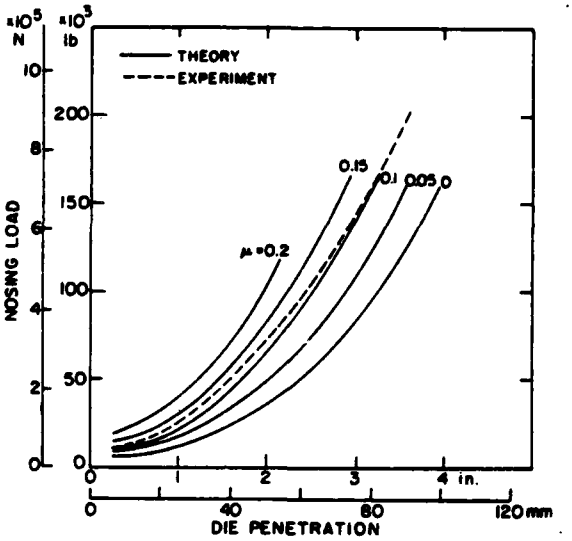

Fig. 4 Load-displacement curves for cold nosing of AISI 1018 steel shell

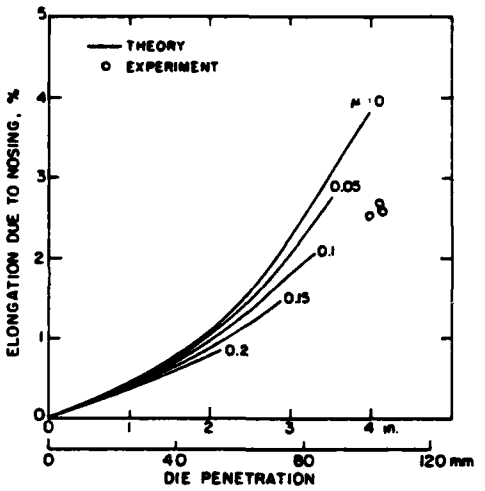

Fig. 5 Elongation of cold nosing of AISI 1018 steel shell

By making $\gamma = \infty$, and $Y = \bar{\sigma}$, the relationship given by (8) is easily incorporated.

This nonsteady-state deformation problem was analyzed in a step-by-step manner by treating it quasi-linearly during each incremental deformation. Ten uniform elements were used in the axial direction. The initial step size for each incremental deformation step is 6 mm. When the boundary contact region moves, the step size is modified in such a way that a free nodal point just comes in contact with the die at the end of the step.

The nosing velocity was 6.0 in./min, or 2.54 mm/s. The uniform velocity field of 2.54 mm/s was used as an initial guess. The solution obtained from the previous step was then used as an initial guess for the subsequent step. The computation was performed for each step solution until an accuracy of the error norm $\|\Delta v\|/\|v\| \leq 0.00001$ was reached. It took 8 to 10 iterations to reach this point of convergence. For each step, the friction forces were modified three to four times to get to within 5 percent of error of the desired friction coefficient value. The considered offset value $\dot{\bar{\varepsilon}}_0$ described previously was 0.0001.

The calculated load-displacement curves, with friction coefficients of 0, 0.05, 0.1, 0.15, and 0.2, respectively, are shown in Fig. 4. It is observed that the experimentally

27

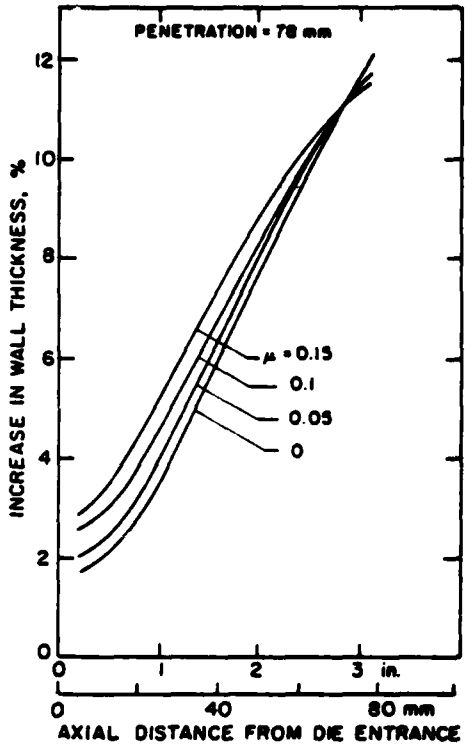

Fig. 6 Increase of wall thickness of AISI 1018 steel shell at penetration of 78 mm

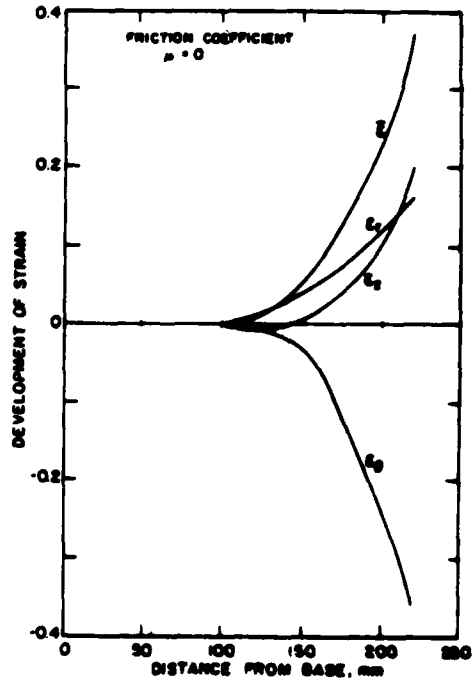

Fig. 7 Strain distributions for AISI 1018 steel shell at $\mu = 0$

measured curve of Battelle Laboratories agrees well with the FEM simulated curves for $\mu = 0.1$. In the experiments, the specimens were phosphated and coated with commercial soap lubricant before nosing. It is interesting to note that $\mu = 0.1$ is typically used in cold forging analysis of steel specimens with phosphate coating and soap lubrication.

Figure 5 shows the elongation in shell length due to nosing

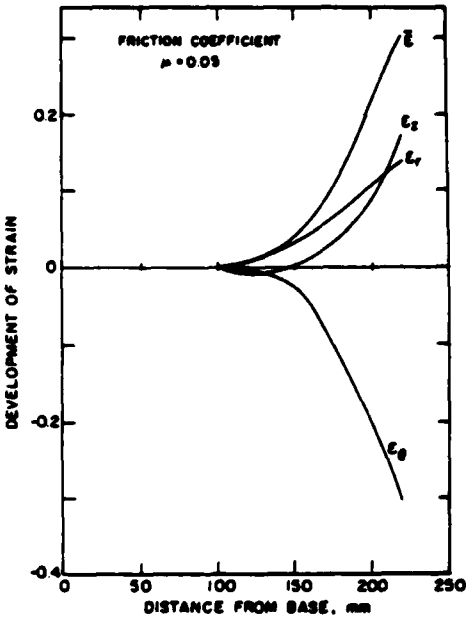

Fig. 8 Strain distributions for AISI 1018 steel shell at $\mu = 0.05$

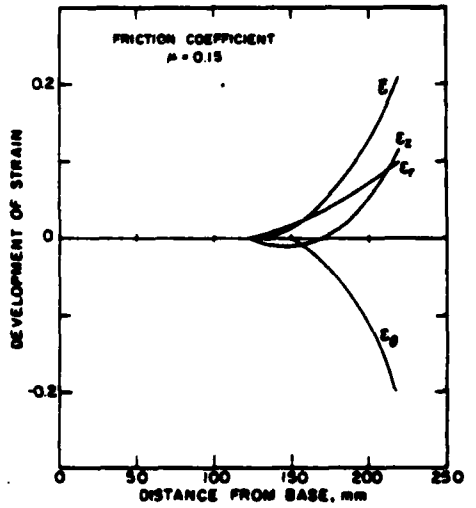

Fig. 9 Strain distributions for AISI 1018 steel shell at $\mu = 0.15$

at various friction values. At low friction values, we have a greater increase in length than at high friction values. This predicted trend is in agreement with experimental observations reported in the literature. As seen in Fig. 5, again the experimentally obtained elongation due to nosing agrees very well with finite-element simulations for friction condition $\mu = 0.1$.

During the nosing process, the shell wall thickness invariably increases with increasing penetration in the die and with increasing frictional restraint at the die-workpiece interface. Figure 6 illustrates this trend and gives the shell-wall thickness distribution as predicted by the FEM simulation at various friction conditions. The thickness of the shell-wall progressively increased over the length of the shell in contact with the die, with the increase being greatest at the nose tip. It is observed in a small region near the nose tip that the increases in wall thicknesses are about the same for various friction values.

For different frictional conditions, the distributions of

28

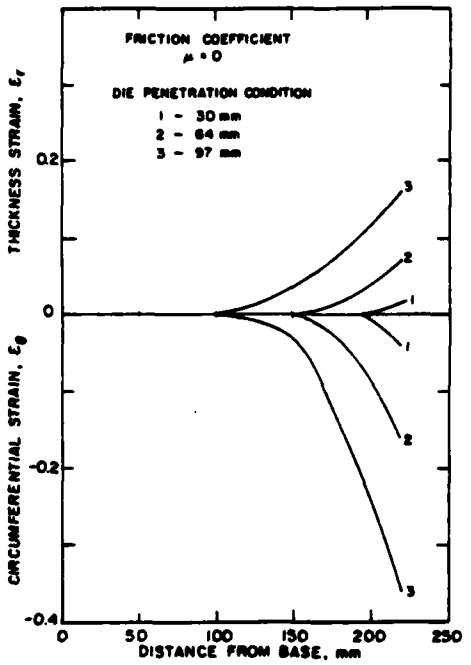

Fig. 10 Strain distributions during nosing of AISI 1018 steel shell

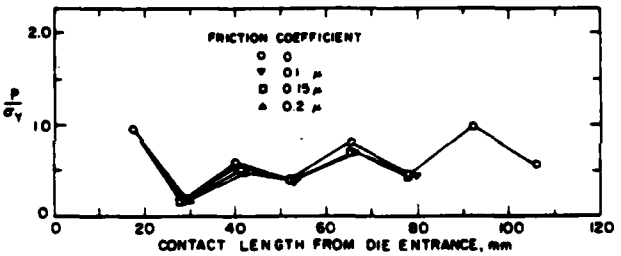

Fig. 11 Die pressure distribution in the nosing of AISI 1018 steel shell

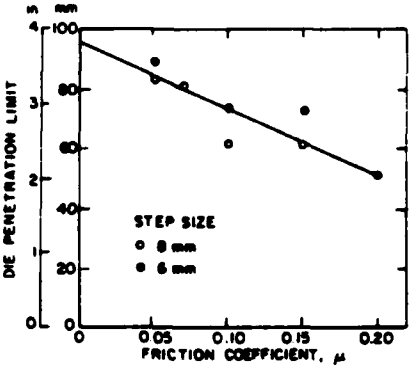

Fig. 12 The effect of friction coefficient on die penetration limit in nosing

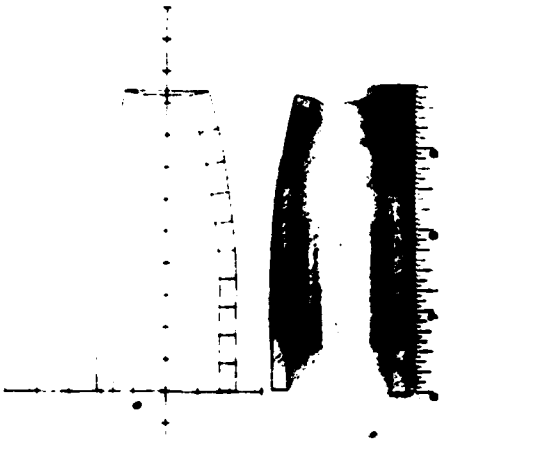

Fig. 13 Comparison of deformed shapes between FEM calculation and experiment for specimen with t/OD = 12 percent at penetration of 46.5 mm

axial strain ϵ_z, circumferential strain ϵ_θ, thickness strain ϵ_r, and effective strain $\bar{\epsilon}$ are plotted in Figs. 7 to 9 for the entire length of the nosed shell for various values of coefficient of friction. The sum of ϵ_z, ϵ_r, and ϵ_θ remains zero for any amount of plastic deformation, and the incompressibility condition is satisfied.

It is interesting to note from the strain distribution plots that axial strain ϵ_z has negative values near the main body of the shell. This suggests that the workpiece is shortened near the entrance of the die. The lengthening of the shell takes place in the remaining two-thirds of the nosed portion.

The determination of the proper preform profile to use, in order to obtain a certain finished shape after nosing, involves a consideration of the strains existing in the shell nose. Figure 10 shows progressively how the strain distributions change during the nosing process for frictionless conditions. The general trend is the same for all friction conditions.

The die pressure distribution was calculated from finite-element simulation results by dividing nodal point forces over the element contact area. In Fig. 11, the die pressure distribution is plotted along the die contact length for various friction conditions at the end of nosing. The yield strength of the material is σ_y.

It can be seen from the figure that friction at the die-workpiece interface has little effect on die pressure distribution. It is also noted that the die pressure at the die entrance, or the nose base, is of the magnitude of the yield strength of the material at the nosing limit. This indicates that for friction formulations in FEM simulation, both the Coulomb Law, $F = \mu P$, and the Shear Friction Formulation, $F = mk$ (k is shear yield stress) will give similar results. In other words, the values of μ and m in shell nosing process are comparable.

The limit of die penetration was recognized in the finite-element simulation by the fact that the solution diverges after a certain amount of penetration. The limit of die penetration depends on friction along the interface, and the effect of friction coefficients on this limit is illustrated in Fig. 12. As the coefficient of friction is increased, the penetration limit is reduced, according to the computer simulation.

Investigation of the Nosing of Shells for 2024 Aluminum

In order to make more extensive comparisons between theory and experiment, laboratory experiments were conducted to study the geometrical changes and the forces required for nosing shells of aluminum alloy 2024.

The geometry of the die shape and the dimension of the die and the workpiece comprise a scaled-down model of the 105-mm shell. The specimen dimensions are 1.7 in. (43.18 mm) outside diameter, 3.6 in. (91.44 mm) length, and 0.204 in. (5.18 mm) wall thickness. Nosing was conducted, using wax as a lubricant, with a speed of 0.1 in./min. Four specimens were tested, but pushed to various depths into the die. The load and displacement curves were recorded. After nosing,

29

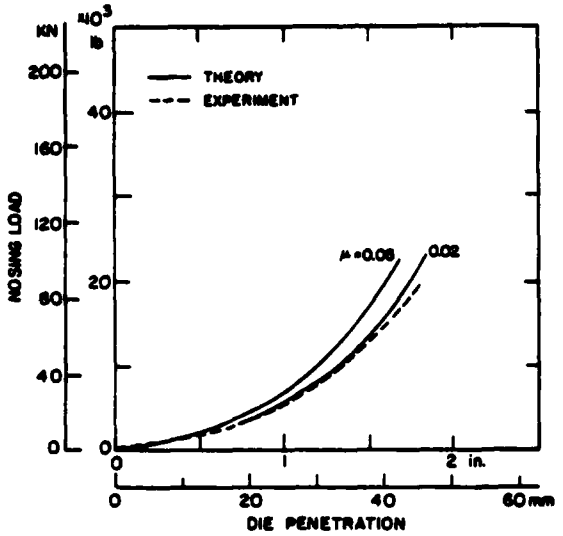

Fig. 14 Comparison of load-displacement curves between FEM calculation and experiment

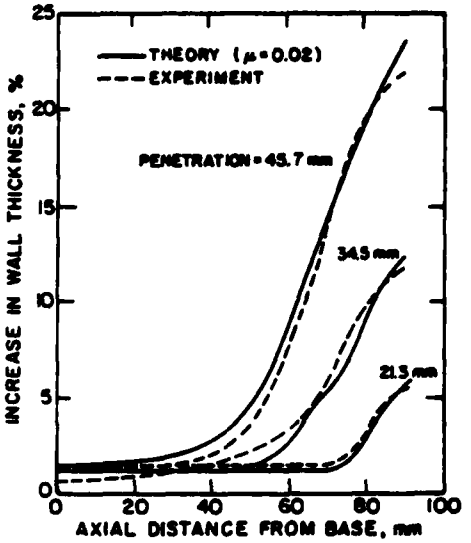

Fig. 16 Development of increase in wall thickness

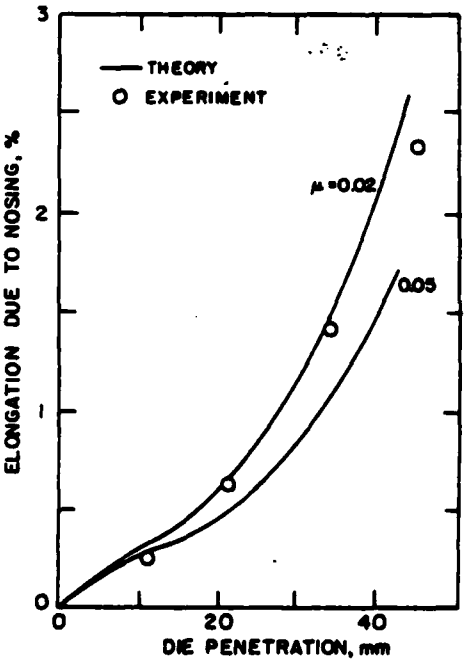

Fig. 15 Elongation due to nosing

the specimens were cut along a diametric plane and elongation and thickness distribution were measured. The true stress and strain relationship, given by $\sigma = 10\,(1 + 4.6\epsilon^{0.292})$ (ksi), was used in the finite-element calculation. The over-all visual comparison of the deformed shapes, obtained by computation and by experiment, is shown in Fig. 13. Good agreement between them in terms of total height and wall thickness change is evident. Computer simulations were made for two friction conditions: $\mu = 0.02$ and $\mu = 0.05$. The calculated load-displacement curves, together with the experimental result, are presented in Fig. 14. It is observed that the experimental result agrees very well with the simulation for friction condition, $\mu = 0.02$.

The elongation of specimens due to nosing, together with the elongation predicted by the finite-element method, are shown in Fig. 15. Under the test conditions, the largest increase in length was about 2.5 percent. Again, the agreement between the experimental results with finite-element simulations for friction condition $\mu = 0.02$ are good. As the depth of penetration increased, the experimental results moved closer towards the finite-element predictions for the friction condition of $\mu = 0.05$. This is because the speed of nosing was slow and the lubricant was squeezed out as the specimen penetrated deeper into the die. Then the friction condition between shell and die no longer remained the same as at the beginning of nosing, and the lengthening was reduced. It is also noted that the change in length becomes more sensitive to the lubrication condition as the depth of penetration increased. This illustrates the importance of lubrication in nosing.

The development of increase in wall thickness at various depths of penetration is shown in Fig. 16. The finite-element predictions for friction condition $\mu = 0.02$ are also presented for comparison. The results shown in Figs. 14, 15, and 16 demonstrate that agreement between theory and experiment is excellent, not only over-all but also in detail.

Summary and Conclusions

The finite-element simulation methods were developed to study nosing of shells at room temperature. In the finite-element formulation, the nine-node quadrilateral elements with quadratic velocity distribution were used. In order to satisfy the geometrical requirement, the boundary conditions of the material nodes in the die contact region were implemented through a mathematical expression which relates the axial velocity to radial velocity during the nosing. With the advancement of the die, the boundary separating the contact region from the unsupported region changes. The treatment of moving boundary in the analysis of nosing was successfully implemented in the finite-element program.

Computer simulations were performed for nosing shells of AISI 1018 steel and aluminum alloy 2024. The solutions were obtained in terms of load-displacement curves, thickness distribution, elongation and strain distributions. The solutions for 1018 steel nosing were compared with experimental results obtained at the Battelle Columbus Laboratories. Experiments of aluminum 2024 nosing were conducted to observe metal flow characteristics in more detail.

Comparisons between the predictions and experimental

30

results were satisfactory, not only over-all but also in detail for both materials.

Acknowledgments

The authors wish to thank the Army Research Office, Research Triangle Park, North Carolina, for Contract DAAG 29-79-C-0217 under which the present investigation was possible.

They also wish to thank Dr. G. D. Lahoti, Battelle Columbus Laboratories, for providing the detail information on the experiment using AISI 1018 steel nosing. They further wish to thank Ikuko Workman for typing the manuscript.

References

1 Shah, S. N., Lee, C. H., and Kobayashi, S., "Compression of Tall, Circular, Solid Cylinders Between Parallel Flat Dies," *Proc. Int. Conf. Prod. Engrs.*, Tokyo, 1974, p. 295.

2 Shah, S. N., and Kobayashi, S., "Rigid-Plastic Analysis of Cold Heading," *Proc. 15th Int. Mach. Tool Design & Res. Conf.*, 1975, p. 603.

3 Chen, C. C., Oh, S. I., and Kobayashi, S., "Ductile Fracture in Axisymmetric Extrusion and Drawing. Part 1: Deformation Mechanics of Extrusion and Drawing," ASME JOURNAL OF ENGINEERING FOR INDUSTRY, Vol. 101, No. 1, 1979, pp. 23-35.

4 Chen, C. C., and Kobayashi, S., "Rigid-Plastic, Finite-Element Analysis of Ring Compression," *Applications of Numerical Methods to Forming Processes*, ASME, AMD, Vol. 28, 1978, p. 163.

5 Nadai, A., "Plastic State of Stress in Curved Shells: The Forces Required for Forging of the Nose of High-Explosive Shells," *Forging of Steel Shells*, presented at the annual meeting of the ASME, New York, Nov. 23-Dec. 1, 1943.

6 Onat, E. T., and Prager, W., "Nosing of Shells," Technical Report DA798/15, Brown University, Providence, R.I., 1954, pp. 1-8.

7 Cruden, A. K., and Thompson, J. F., "The End Closer of Backward Extruded Cans," NEL Report No. 511, National Engineering Laboratories, Glasgow, 1972.

8 Lahoti, G. D., and Altan, T., "Analysis of Metal Flow in Nosing of Tubular Products," *Proc. 6th NAMRC*, Manufacturing Engineering Transaction, 1978, p. 151.

9 Lahoti, G. D., Subramanian, T. L., and Altan, T., "Development of a Computerized Mathematical Model for the Hot/Cold Nosing of Shells," Contract Report ARSCD-CR-78019, Battelle Columbus Laboratories, Sept. 1978.

10 Tang, M. C., "An Investigation of the Shell Nosing Process by the Finite-Element Method," Ph.D. dissertation, Department of Mechanical Engineering, University of California, Berkeley, September 1981.

11 Oh, S. I., Rebelo, N., and Kobayashi, S., "Finite-Element Formulation for the Analysis of Plastic Deformation of Rate-Sensitive Materials in Metal Forming," Metal Forming Plasticity, IUTAM Symposium, Tutzing, Germany, Aug.-Sept. 1978, p. 273.

Printed in U.S.A

THE AMERICAN SOCIETY OF MECHANICAL ENGINEERS
345 E. 47 St., New York, N.Y. 10017

82-Prod-15

31
#4

31

An Investigation of the Shell Nosing Process by the Finite-Element Method. Part 2: Nosing at Elevated Temperatures (Hot Nosing)

Ming-Ching Tang
IBM,
San Jose, Calif.

Shiro Kobayashi
Professor,
Department of Mechanical Engineering,
University of California,
Berkeley, Calif.
Fellow ASME

The metal-forming processes of shell nosing at elevated temperatures were analyzed by the finite-element method. The strain-rate effects on materials properties and the flow stress dependence on temperatures were included in the finite-element analysis. A thermodynamic theory of visco-plasticity based on rational mechanics was adapted to a rigid-plastic material idealization. An implicit scheme is used for the time integration of heat transfer equations, which is coupled to the plasticity equations. The nine-node quadrilateral elements with quadratic velocity distribution were used for the workpiece, and four-node quadrilateral elements were used for the die in the heat transfer analysis and temperature calculations. The coupled analysis of heat transfer and deformation was applied to the forming of AISI 1045 steel shells. Correlation between simulation and experimental results are good.

Introduction

Nosing of large shells (155 mm and above) is done at hot working temperatures. Prior to nosing, the end portion of the tube to be formed is heated to temperatures of between 1500 to 1900°F by tubular wound induction coils. Then the shell is nosed by forcing it into a suitably shaped die. When deformation takes place at high temperature, the flow stress of the material is a function of temperature and strain rate. The temperatures in the shell wall are influenced by (1) preheating conditions, (2) heat generation due to deformation and friction, and (3) heat transfer to the nosing die. Determination of these temperature distributions along the length of the shell wall is important and necessary in order to predict accurately the flow of metal and the nosing load in the hot nosing.

In fact, the temperature distribution is rather critical and much effort has been concentrated on the preheating conditions. If the heating is gradual and slow, the unheated portion of the tube gains heat by conduction. Consequently, the tube tends to buckle under axial load during nosing. Therefore, preheating is done at a rapid rate so that the high temperature does not travel back to that part of the shell which should remain relatively cold.

Until recently, most of the temperature calculations during a metal-forming process have been based on a procedure that uncouples the problem of heat transfer from the metal deformation problem. The approach was to determine the flow characteristics of the problem either experimentally or by calculations, then use these calculations for the computation of heat generation and temperature distribution.

A paper by Oden, Bhandary, Yagawa, and Chung [1] presents the first coupled analysis of deformation and heat transfer for elasto-viscoplastic materials in a three-dimensional rectangular bar. Rebelo and Kobayashi [2] have made a coupled thermo-viscoplastic analysis in solid cylinder and ring compression. In a previous work by Lahoti, Subramanian, and Altan [3], the heat-transfer problem during and after induction heating was analyzed by the finite-difference method. We present here the finite-element

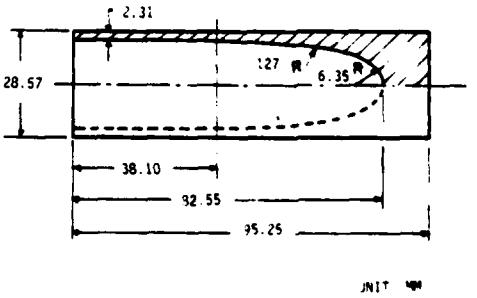

Fig. 1 Hot nosing specimen

Contributed by the Production Engineering Division for presentation at the Design and Production Engineering Technical Conference, Washington, D.C., September 12-15, 1982, of THE AMERICAN SOCIETY OF MECHANICAL ENGINEERS. Manuscript received by the Production Engineering Division February 8, 1982. Paper No. 82-Prod-15.
Copies will be available until June 1983.

32

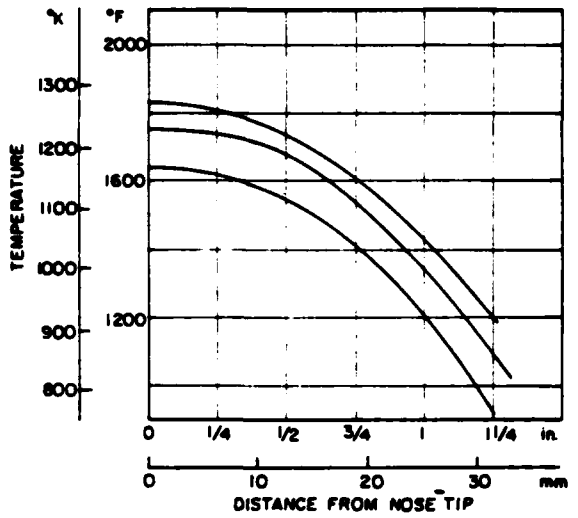

Fig. 2 Temperature distributions obtainable by induction heating for a small model of 105-mm shell

simulation for the coupled analysis of metal deformation and heat transfer during hot nosing. The results are compared with the experimental work by Carlson [4], and with the confirmation testing of hot nosing process conducted by Battelle Columbus Laboratories [5]. The effects of temperature distribution on nosing are shown and discussed.

Coupled Thermo-Viscoplastic Analysis

The finite-element equations resulting from discretizing weak forms of the equilibrium equations and heat balance equations were given by Rebelo and Kobayashi [2]. The finite-element method for the deformation analysis is described in the accompanying paper [6].

For heat-transfer analysis, heat balance equations upon finite-element discretization are reduced to the form

$$C\dot{\mathbf{T}}+K\mathbf{T}=\mathbf{Q}, \tag{1}$$

where

- C = heat capacity matrix
- K = heat conduction matrix
- $\mathbf{Q}$ = heat flux vector
- $\mathbf{T}$ = vector of nodal point temperatures
- $\dot{\mathbf{T}}$ = vector of nodal point temperature rates

The heat flux vector $\mathbf{Q}$ in equation (1) has several components, and is expressed with interpolation function N by

$$\mathbf{Q}=\int_V \upsilon(\partial\dot{\varepsilon})N\,dV+\int_{S_r}\sigma\epsilon(T_e^4-T_s^4)\mathbf{N}\,dS_r$$

$$+\int_{S_c} h(T_e-T_s)\mathbf{N}\,dS_c$$

$$+\int_{S_t} h_{\text{Lub}}(T_d-T_w)\mathbf{N}\,dS_t+\int_{S_t} q_f\mathbf{N}\,dS_T \tag{2}$$

The first component is the contribution of the net heat generated inside the deforming body, and the fraction υ of the plastic work rate is assumed to be 0.9. The second component is the contribution of the heat radiation from the environment, where σ is the Boltzman constant, ϵ is the radiation coefficient, and T_e and T_s are environment temperature and surface temperature, respectively. The third term describes the heat convection between body surface and environment with heat convection coefficient h. The fourth term represents the contribution of the heat transferred between workpiece and die through their interface. T_d and T_w are die temperature and workpiece temperature, respectively, and h_{Lub} is the heat transfer coefficient from the lubricant. The last term is the contribution of the heat generated by friction along the die-workpiece interface, q_f being the surface heat generation rate due to friction.

Coupling of deformation analysis and temperature calculation is seen in the scheme of time integration of equation (1).

The scheme requires consistency and stability. The first requirement is satisfied by an approximation

$$\mathbf{T}_{t+\Delta t}=\mathbf{T}_t+\Delta t[(1-\beta)\dot{\mathbf{T}}_t+\beta\dot{\mathbf{T}}_{t+\Delta t}] \tag{3}$$

where t and Δt are time and its increment, respectively, and β

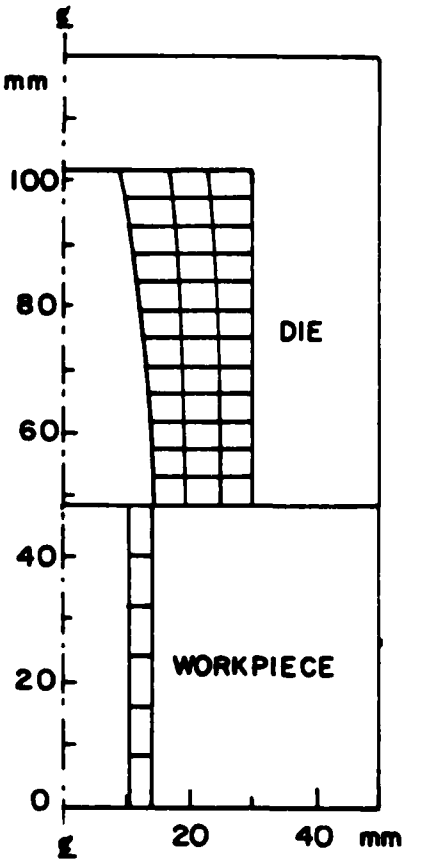

Fig. 3 Initial mesh for nosing of a small model of 105-mm shell

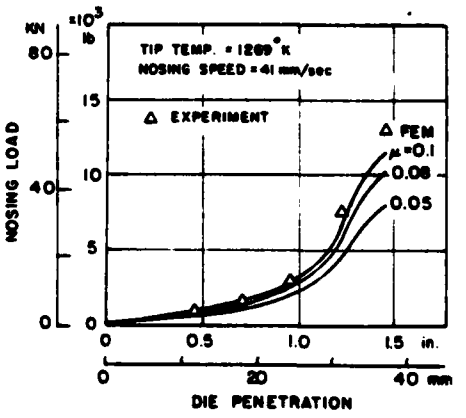

Fig. 4 Load-displacement curves at various friction conditions for hot nosing of a small model of 105-mm shell

Table 1 Stress, strain, strain-rate, temperature relationships of AISI 1045 steel

$$Y\left[1+\left(\frac{\dot{\epsilon}}{\gamma}\right)^{n}\right] \text{ (unit Ksi)}$$

At $\epsilon = 0.1$

$$Y = -7.2588\times10^{-8}T^3 + 4.4912\times10^{-4}T^2 - 0.938T + -64.6$$

$$n = -0.1743\times10^{-9}T^3 + 0.1026\times10^{-5}T^2 - 0.1917\times10^{-2}T + 1.3$$

$$\gamma = -0.8682\times10^{-8}T^3 + 0.5285\times10^{-4}T^2 - 0.107 + 72.28$$

At $\epsilon = 0.2$

$$Y = -4.9439\times10^{-8}T^3 + 3.1695\times10^{-4}T^2 - 0.69T + 513.56$$

$$n = 0.7859\times10^{-9}T^3 - 0.4496\times10^{-5}T^2 + 0.8633\times10^{-2}T - 5.38$$

$$\gamma = -0.501\times10^{-8}T^3 + 0.3057\times10^{-4}T^2 - 0.062T + 42.06$$

At $\epsilon = 0.3$

$$Y = -6.3728\times10^{-8}T^3 + 4.082\times10^{-4}T^2 - 0.8831T + 648.61$$

$$n = -0.5858\times10^{-9}T^3 + 0.3396\times10^{-5}T^2 - 0.6397\times10^{-2}T + 4.09$$

$$\gamma = -0.8535\times10^{-8}T^3 + 0.519810^{-4}T^2 - 0.1053T + 71.05$$

At $\epsilon = 0.4$

$$\gamma = -0.8535\times10^{-8}T^3 + 0.5198\times10^{-4}T^2 - 0.1053T + 71.05$$

$$n = -0.2457\times10^{-9}T^3 + 0.1278\times10^{-5}T^2 - 0.2046\times10^{-2}T + 1.15$$

$$\gamma = -0.6617\times10^{-9}T^3 + 0.4094\times10^{-5}T^2 - 0.8441\times10^{-2}T + 5.79$$

where T is temperature in °F. Use interpolation to get flow stress for any $\epsilon < 0.4$

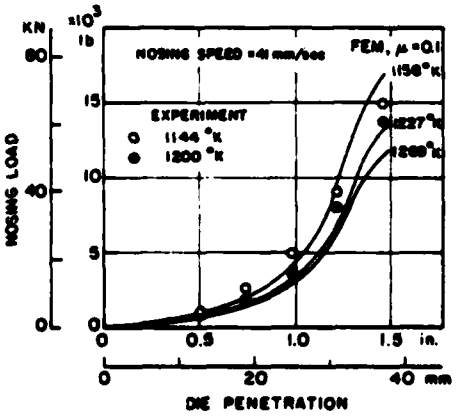

Fig. 5 Load-displacement curves for different initial tip temperatures at speed of 41 mm/s for hot nosing of a small model of 105-mm shell

is a parameter varying between 0 and 1. For unconditional stability β should be greater than 0.5, and a value of 0.75 was chosen. A detail on an implementation of the algorithm to include the coupling of the solution of stress equilibrium equations with heat balance in the finite-element program is given elsewhere [6].

Hot Nosing of a Small Model of 105-mm Shell

To study the nature of the nosing process in the forging of shells, Carlson [4] conducted hot nosing on a small model of a 105-mm shell. Commercial open-hearth, cold-rolled steel was used in making the specimens. Geometric details of the specimens are given in Fig. 1.

The die that was employed throughout the experiments has a radius of curvature of 11.85 in. for an ogive profile. To simulate the amount of nosing done on the 105-mm shell, 1.45 in. of the specimen was made to enter the die, giving a maximum reduction in the mean diameter of about 33 percent.

In preparation for the test, the die was heated for about 1 hr to bring it to a temperature of 1000°F. The testing temperature of the shell was from 1600°F to 1900°F at the tip. To measure the temperature distribution, six chromel-alumel thermocouples were placed along the shell model. The measured temperature distributions are shown in Fig. 2.

The heating of the shell was done in about 1 min by an induction coil. The time of nosing was of the order of 1 s.

The finite-element simulations were carried out, using the mesh system and dimensions shown in Fig. 3. A total of 39 nodes and 6 nine-node elements were used for the workpiece. The die mesh has 13 four-node quadrilateral elements and a total of 52 nodes.

The material properties of the specimen used in the experiments were very close to that of AISI 1045 steel. Flow stress expressions of 1045 steel were found from experimental data of Altan and Boulger [7]. We rederive the expressions and reduce them to fit the relationship, as shown in Table 1.

The heat transfer characteristics were taken from standard handbooks:

K_w = 30.28 N/s K (workpiece heat conductivity)
$(\rho C)_w$ = 3.69 N/mm² K (ρ, density; C_w, workpiece heat capacity)
K_d = 19 N/s K (die heat conductivity)
$(\rho C)_d$ = 3.69 N/mm² K (ρ, density; C_d, die heat capacity)
h = 0.0692 N/s mm K (heat convection coefficient)
h_{Lub} = 32.88 N/s mm K (heat transfer coefficient from lubricant)

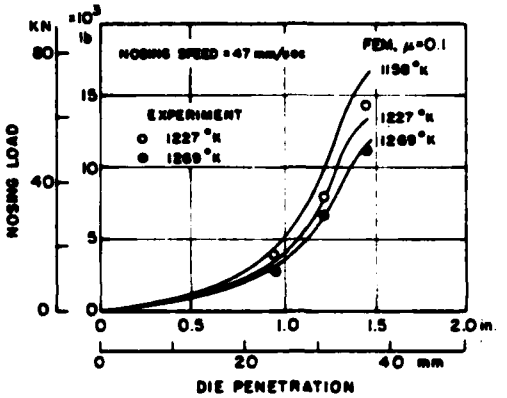

Fig. 6 Load-displacement curves for different initial tip temperatures at speed of 47 mm/s for hot nosing of a small model of 155-mm shell

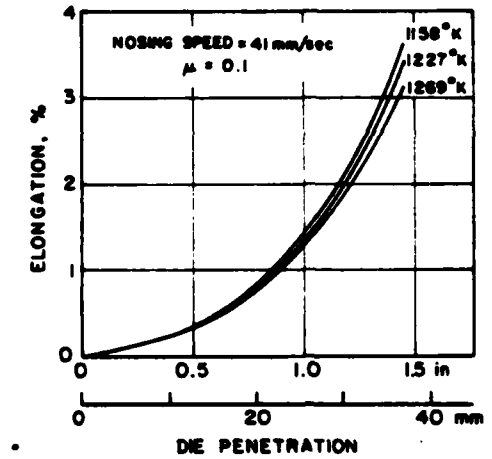

Fig. 7 Effect of initial temperature on elongation due to nosing

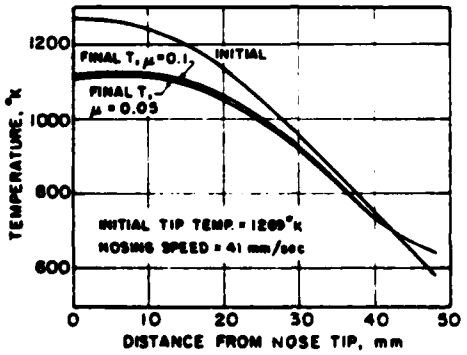

Fig. 8 Temperature distribution after nosing with initial tip temperature = 1269 K

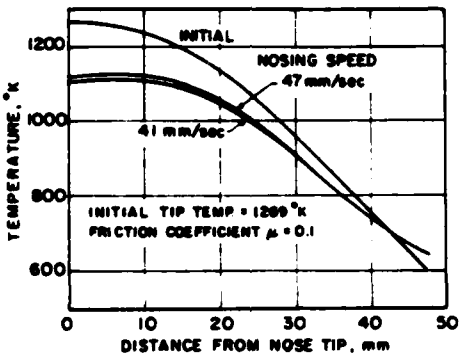

Fig. 9 Comparison of final temperature distributions for different nosing speeds

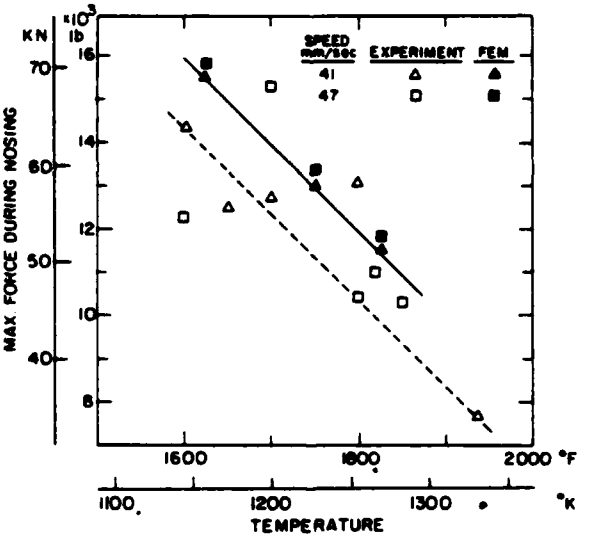

Fig. 10 Effect of temperature on maximum force during nosing

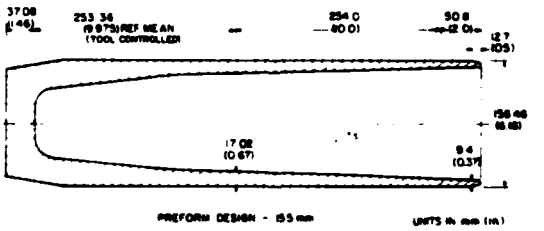

Fig. 11 Preform design of 155-mm shell

The outer boundaries of the die are sufficiently far from the interface, and a constant temperature is imposed on time.

The nosing speeds of 47 mm/s (1.85 in./s) and 41 mm/s (1.62 in./s) were simulated by the finite-element calculations. The uniform velocity field equivalent to the nosing speed was used as the initial guess. Step size was 2.5 mm.

In deformation calculations, an average of nine iterations was needed for convergence, plus up to ten more to get the desired friction coefficient. Normally another three iterations were needed for temperature convergence.

The FEM load-displacement curves for hot nosing at various friction conditions, with initial tip temperature at 1825°F (1269 K) and speed 1.62 in./s (41 mm/s) are given in Fig. 4. It can be seen that the simulation results are very close to those of the experiments for friction coefficient $\mu = 0.1$. In Fig. 5, the load displacement curves are obtained by FEM for initial tip temperatures at 1625°F (1158 K), 1750°F (1227 K), and 1825°F (1269 K), respectively, at nosing speed of 41 mm/s and $\mu = 0.1$. Figure 6 is a plot similar to Fig. 5, with higher nosing speed of 47 mm/s. All of the FEM simulation results showed good agreement with the experimental data for $\mu = 0.1$. It is observed that the nosing load increased as the workpiece temperature decreased.

The effect of temperature on shell elongation is illustrated in Fig. 7. It is noticed that as the wall temperature increased, the elongation is reduced slightly.

Figure 8 shows the temperature distribution before and after nosing, for initial tip temperature of 1269 K and nosing speed of 41 mm/s, at $\mu = 0.1$ and $\mu = 0.05$. At the end of nosing, the FEM predicted a temperature drop of about 160 K on the nose tip. However, at the nose base, a temperature rise

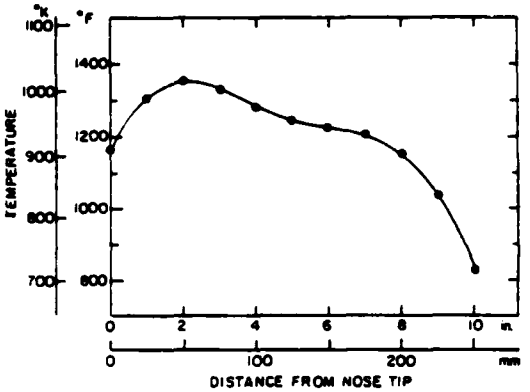

Fig. 12 Temperature distribution of 155-mm preform prior to nosing

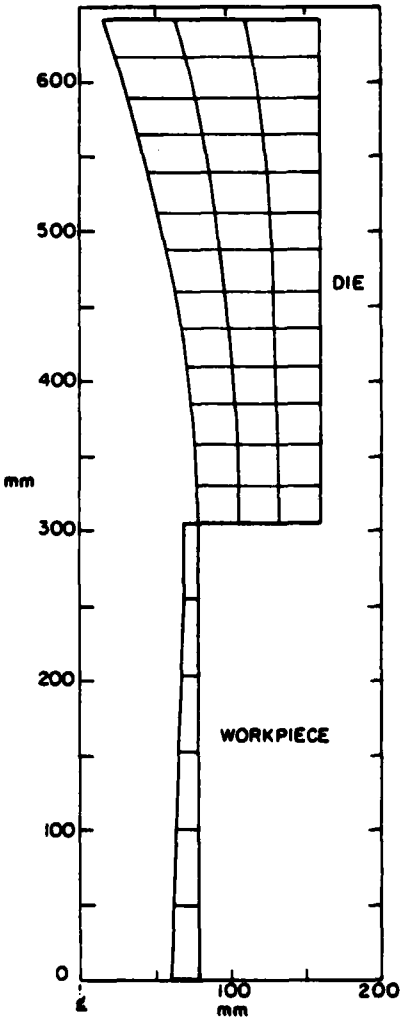

Fig. 13 Mesh system for FEM simulation of 155-mm shell nosing

of about 50 K was expected due to conduction heat from the upper portion of the shell to the lower portion. Friction condition has very little effect on the temperature distribution. This means that the heat generated due to friction is small compared to the amount generated by convection or conduction. With lower initial temperatures on the workpiece, the results in temperature distribution after nosing are similar. A comparison of final temperature distributions for different nosing speeds is shown in Fig. 9. In the region near the nose tip where large deformation occurred, the final temperatures are predicted to be higher with greater nosing speed. In the region near the nose base, the temperatures are the same. More heat is generated when nosing speed increases.

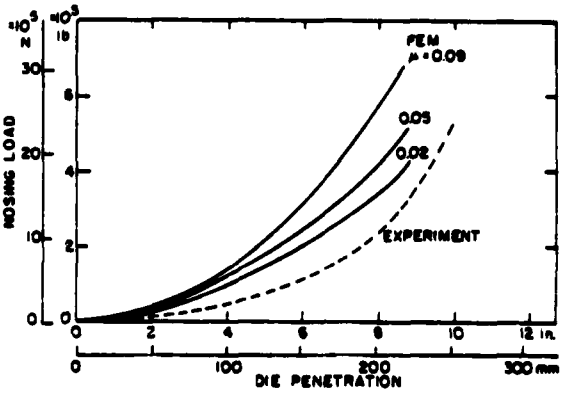

Fig. 14 Comparison of load-displacement curves from FEM calculation and experiment for hot nosing of 155-mm shell

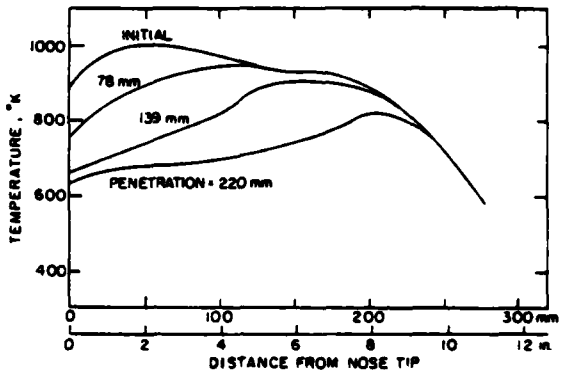

Fig. 15 Outer surface temperature distributions at different die penetrations

Figure 10 shows maximum force curves during nosing and at initial tip temperature. The considerable scattering of the experimental results is due to the limitation of the indicator diagram in depicting maximum force. However, a consistent trend was observed when comparisons were made between FEM simulation and experimental results. Deviations between computer and experimental values were about 15 percent. The effect of nosing speed on maximum force was less obvious from FEM simulation than from experiments. This may be due to the fact that the rate-sensitivity constant used in the simulation is different from that of the material used in experiments.

Hot Nosing of 155-mm Shell

Confirmation testing of the hot nosing process was conducted by Battelle Laboratories at Chamberlain Manufacturing Corp. in order to study the material flow of a selected preform at hot nosing temperatures. The projectile was that of a 155-mm shell, and the material was modified AISI 1045.

Preform dimensions were measured and recorded. Preform temperatures were measured, using imbedded thermocouples at six places in the region near the nose tip. Details of the preform design are given in Fig. 11. The preform was heated to 1400°F at the tip, using the induction coil. The temperature distribution prior to nosing is shown in Fig. 12. The nose die has 10.5-in OD and is enclosed by a water-jacket; typically, the water in the jacket is nearly boiling. The die temperature is estimated at about 400°F.

Water-based graphite was used as the lubricant in the test.

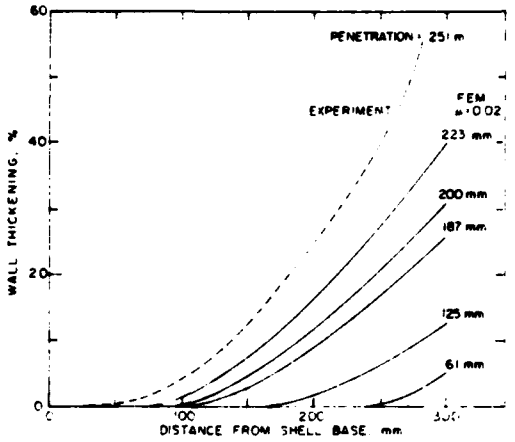

Fig. 16 Comparison of thickness distribution between FEM prediction and experiment

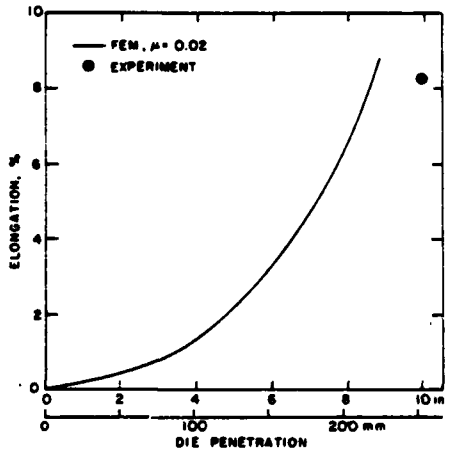

Fig. 17 Elongation during hot nosing

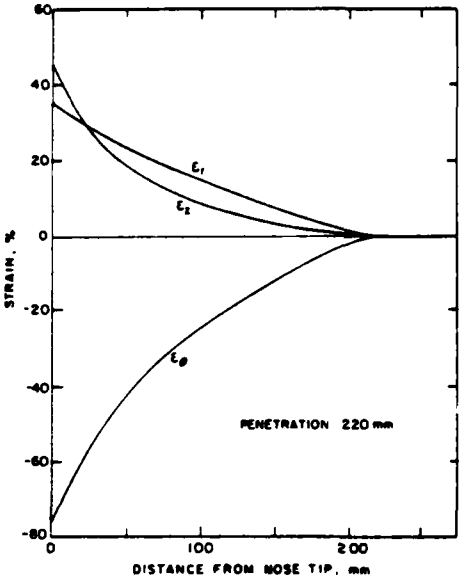

Fig. 18 Strain distributions at penetration of 220 mm

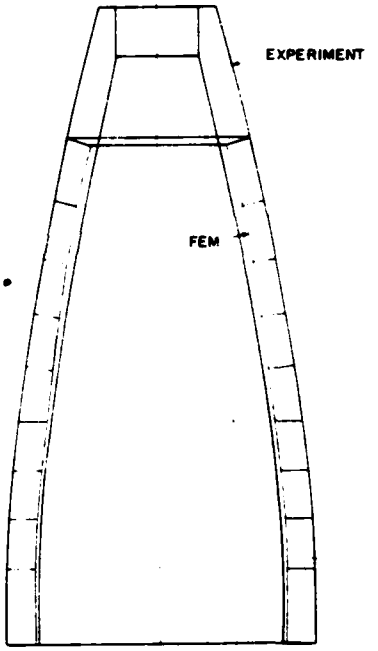

Fig. 19 Comparison of deformed shapes between FEM and experiment

The ram speed of the 800-t mechanical press was 2.5 in. (63.5 mm) per second in carrying out the nosing process.

The mesh system for the finite-element simulation was built with 39 nodes and 6 nine-node elements in the workpiece, and 56 nodes and 39 four-node elements in the die. The initial grid is shown in Fig. 13. Total penetration of the shell into the nosing die was about 225 mm, obtained in 14-mm steps. A constant temperature was imposed on the outer boundaries of the die.

Flow stress expressions for AISI 1045 and the heat transfer characteristics were the same as described in the previous section.

The load-displacement curves that were obtained from finite-element simulations for various friction coefficients are compared with experiments in Fig. 14. The ring-compression test gave a value of $\mu = 0.09$, and from FEM results this value was considered to be too high. A value of $\mu = 0.02$ or smaller gives simulation results closer to that in the experiments. Near the end of nosing, the experiments showed a steeper increase in the load than did the FEM, possibly because the lubricant was squeezed out, thereby increasing friction.

The temperature distributions of the shell outer surface at different penetration depths are presented in Fig. 15. As the contact between die and workpiece increases, the temperature of the workpiece in the contact region gradually decreases due to heat flow from the workpiece to the colder die. The test results showed product temperatures of between 900 and 1000 K, which agree with the average temperature distribution from the FEM.

Temperature rises as expected around the contact areas in the die, and the differences between workpiece and die temperatures decrease substantially during the course of deformation.

A comparison of thickness distribution along the shell is given in Fig. 16. Thickness distributions at several penetration depths are predicted by the FEM model. An increase of penetration depth increases the thickness for a given point. Also, the region of wall thickening extended towards the nose base. A consistent trend was observed when comparisons were made between computer-calculated wall thickness and experimental results.

The 155-mm shell length increases after hot nosing under good lubrication, as shown both by experiments and by FEM simulation. Figure 17 gives shell elongation versus die

penetration during hot nosing. An increase in length of 8 percent is expected after penetration of 220 mm. Recall that only 4 percent elongation was expected at the end of nosing for a 105-mm shell. This indicates more elongation for larger reduction in mean diameter in shell nosing.

In Fig. 18 we plotted the distributions for axial strain ϵ_z, radial strain ϵ_r, and circumferential strain ϵ_θ at die penetration of 220 mm. The compatibility is satisfied as the sum of ϵ_r, ϵ_z, ϵ_θ remains zero. The axial strain ϵ_z does not show negative value near the nose base as it did in the cold nosing simulation. This suggests that lengthening takes place in the entire nosed portion of the shell.

The deformed shape of the nose from FEM simulation is compared to that of the experiment in Fig. 19. Since the preforms are not exactly the same in the region near the nose tip, the FEM predictions did not match the experiments. Additionally, the FEM model showed a nosing limit beyond which material can no longer support the nosing load, and a change of deformation mode (e.g., buckling) may occur. Therefore, the maximum depth of penetration was also different for the FEM model. The discrepancy may arise from the fact that the flow stress expressions implemented in FEM calculations could be different from those of the materials used in experiments.

Summary and Conclusions

In this investigation the finite-element simulation methods were developed to study nosing of shells at elevated temperatures. The deformation analysis and heat transfer analysis, including dies, were coupled together for an iterative simultaneous solution. The nine-node quadrilateral elements with quadratic velocity distribution were used for the workpiece, and four-node quadrilateral elements were used in the die for the heat transfer analysis and temperature calculations.

The equations that describe the deformation mechanics are nonlinear and were solved by Newton-Raphson's iterative technique. An implicit scheme was used in the time integration of heat transfer equations which provides good accuracy for a reasonably large range of time steps. The die part was remeshed after each deformation step.

Finite-element programs were written in FORTRAN IV for a CDC 7600 computer. Listing of these programs, including instructions for input data preparation, are given in reference [8].

It is important to determine the precise shapes of the profiles of shells (thickness distribution) in the original cylindrical forgings to produce the prescribed shapes of shells in their finished condition. For this requirement, the determination of deformation characteristics, in particular the thickness changes, as functions of process variables is essential. Some factors which influence deformation characteristics significantly are the temperature distribution along the cylinder, friction along the die, and pressing speeds.

The coupled analysis of heat transfer and deformation was performed by simulating nosing of a 155-mm shell of AISI 1045 steel. Experimental results were available from Battelle Laboratories, and correlation was good.

By using the finite-element programs developed in this research, we are able to obtain such detailed deformation characteristics as: load-displacement curves, thickness distribution, elongation, strain and strain-rate distributions, and temperature distributions. They are valuable for the control of the nosing process, design of equipment, and preparation of workpieces.

Acknowledgments

The authors wish to thank the Army Research Office, Research Triangle Park, North Carolina, for Contract DAAG 29-79-C-0217 under which the present investigation was possible.

They also wish to thank Dr. G. D. Lahoti, Battelle Columbus Laboratories, for providing the detail informaton on the experiment using AISI 1018 steel nosing. They further wish to thank Ikuko Workman for typing the manuscript.

References

1 Oden, J. T., Bhandari, D. R., Yagawa, G., and Chung, T. J., "A New Approach to the Finite-Element Formulation and Solution of a Class of Problems in Coupled Thermoelastoviscoplasticity of Crystalline Solids," *Nuclear Eng. Design*, Vol. 24, 1973, p. 420.

2 Rebelo, N., and Kobayashi, S., "A Coupled Analysis of Viscoplastic Deformation and Heat Transfer—I and II," *Int. J. Mech. Sci.*, Vol. 22, 1980, pp. 699–718.

3 Lahoti, G. D., Subramanian, T. L., and Altan, T., "Development of a Computerized Mathematical Model for the Hot/Cold Nosing of Shells," Contract Report ARSCD-CR-78019, Battelle Columbus Laboratories, Sept. 1978.

4 Carlson, R. K., "An Experimental Investigation of the Nosing of Shells," *Forging of Steel Shells*, presented at the Winter Annual Meeting of the ASME, New York, Nov. 29–Dec. 3, 1943.

5 Lahoti, G. D., "Confirmation Testing of Hot Nosing of M107 155-mm Shell," unpublished data, Battelle Columbus Laboratories, Sept. 1980.

6 Tang, M. C., and Kobayashi, Shiro, "An Investigation of the Shell Nosing Process by the Finite-Element Method. Part 1: Nosing at Room Temperature (Cold Nosing)," submitted for publication in ASME JOURNAL OF ENGINEERING FOR INDUSTRY, 1982.

7 Altan, T., and Boulger, F. W., "Flow Stress of Metals and its Application in Metal Forming Analysis," ASME JOURNAL OF ENGINEERING FOR INDUSTRY, Vol. 95, No. 4, Nov. 1973, pp. 1009–1019.

8 Tang, M. C., "An Investigation of the Shell Nosing Process by the Finite-Element Method," Ph.D. dissertation, Department of Mechanical Engineering, University of California, Berkeley, Sept. 1981.

Printed in U.S.A.

#5

ANALYSIS OF SHELL NOSING -- PROCESS MECHANICS AND PREFORM DESIGN+

Ming-Ching Tang*

May Hsu**

Shiro Kobayashi***

ABSTRACT

The finite-element method for rigid-plastic materials is used for the analysis of nosing of aluminum alloy 2024 tubular preforms with uniform wall thickness at room temperature. The detailed mechanics were obtained by computer simulation and some of the results, such as load displacement curves, elongation and thickness distributions, were compared with experimental results. Then, assuming that the strain distributions computed by the finite-element method are valid for preforms having nonuniform thicknesses initially, two types of preform shapes were designed to obtain uniform wall thickness after nosing. Experimental results of nosing these preforms showed that the approach to the problem is satisfactory.

February, 1982

* IBM, San Jose, California

** KLA Instruments, Santa Clara, California

*** Department of Mechanical Engineering,
University of California, Berkeley

+ The paper is in press and no clean copy is available at the present time.

6.

A NEW APPROACH TO PREFORM DESIGN IN METAL FORMING WITH THE FINITE ELEMENT METHOD†

by

J. J. Park*, Nuno Rebelo** and Shiro Kobayashi*

ABSTRACT

A new approach to preform design is introduced, as a unique application of the finite element method to the problems in metal forming. The concept involved in the approach is to trace backward the loading path in the actual forming process from a given final configuration using the finite element method. The concept was tested with the problem of simple compression of a cylinder and the method was applied to preform design in shell nosing.

---

† Part 1 of "Preform Design in Metal Forming"

* Department of Mechanical Engineering, University of California, Berkeley, California

** Brown Boveri Research Center, Switzerland

1. INTRODUCTION

One of the most important aspects of the closed die forging process is the design of preforms. An example of preform design for steel finish forgings of various H-shapes is shown in Fig. 1a. Preform design involves the determination of number of preforms and design of the shapes and dimensions of each preform. According to Biswas and Knight [1], the bulk of the work to determine the preform shapes for complex forging components has been carried out in Germany and the Soviet Union, as reported by Spies [2]. Chamouard [3] in France, and Akgerman et al. [4] in the U.S. dealt with some practical problems of preform design for certain forging cross-sections. The present practice to this complex problem is to computerize the design calculations required for the designer's decisions, based on qualitative guidelines which have been derived mainly from experience or experimental studies.

Preform design problem is also involved in shell nosing. Shell nosing is the process of forming an ogive nose at an open end of a tubular part (preform) by pressing the tube into a contoured die. Wall thickness increases, but the shell may elongate or shrink in length during nosing. Because shell specifications usually require certain wall thickness distributions after nosing, the problem is to design the preform with which the desired shape after the nosing operation can be achieved. An example of such a preform is shown in Fig. 1b.

The approach to the preform design in shell nosing has been more quantitative, because the number of variables involved in the determination of preform shapes in shell nosing is fewer than those for preform shapes in general forgings. Nadai [5] outlined an approach for designing the preforms for shells with uniform wall thickness after nosing, based on the strains in the shell nose. Carlson [6] extended Nadai's approach and suggested the method for determining the original shell profile. Based on Carlson's method, Lahoti et al. [7] developed a computer program for the preform design.

In this paper a new approach to preform design is introduced. The concept involved in the approach is to trace backward the loading path in the actual forming process from a given final configuration by the finite element method. The concept was tested with the problem of simple cylinder compression and the method was applied to preform design in shell nosing. Because the computational technique uses the finite element method, a brief description of the finite element method is given, and the new approach to the problem follows.

2. FINITE-ELEMENT METHOD

The concept of the finite-element method is one of discretization. The finite-element model is constructed in the following manner. A number of finite points is identified in the domain of the function, and the values of the function and its derivatives, when appropriate, at these points are specified. These points are called nodal points. The domain of the function is represented approximately by a finite collection of subdomains called finite elements. The domain then is an assemblage of elements connected together appropriately on their boundaries. The function is approximated locally within each element by continuous functions which are uniquely described in terms of the nodal point values associated with the particular element. The path to the solution of a finite-element problem consists of five specific steps: (a) the problem, (b) the element, (c) the element equation, (d) the assemblage of element equations, and (e) the numerical solution of the global equations.

The basis of finite-element metal flow simulation, using the variational approach is to formulate proper functionals, depending upon specific constitutive relations. The solution of the original boundary value problem is obtained by the solution of the dual variational problem where the first-order variation of the functional vanishes. Choosing an approximate interpolation function for the field variable in the elements, the functional is expressed

locally within each element in terms of the nodal point values. The local-element equations are then assembled into the overall problem. Thus, the functional is approximated by a function of global nodal point values. The condition for this functional to be stationary results in the stiffness equations. For metal-forming problems the stiffness equations are nonlinear and solved by the Newton-Raphson iterative method.

For rigid-plastic materials, obeying the Mises yield criterion and its associated flow rule, the incompressibility constraint can be removed by introducing either the Lagrange multiplier or a penalty function into the functional. If the body contains a rigid region, the stresses in the region cannot be determined. This difficulty is handled by considering an offset of the effective strain rate, which is several orders of magnitude smaller than the average strain rate in the deforming zone. The deviatoric stresses are assumed to vary linearly from zero to the flow stress if the effective strain rate is smaller than this offset value. This stress-strain rate relation in the "nearly rigid" region modifies the functional accordingly.

For rigid-viscoplastic materials, the constitutive equations derived from the viscoplastic theory are similar to those of rigid-plastic materials except that the yield stress is a function of strain and strain-rate. Applications of these methods to various metal forming problems are given in a review on the finite element method and metal forming process modeling [8]. Recently, Oh [9], at the Battelle Columbus Laboratories has accomplished a significant development of a user-oriented general purpose FEM program, namely a rigid-viscoplastic FEM Code ALPID. The special features of the program include: (1) use of higher order elements, (2) general description of die and automatic handling of die boundary conditions, and (3) automatic generation of initial guess for iteration procedure. The program ALPID was used for the computation throughout the present investigation.

3. METHOD OF APPROACH

A method of approach is illustrated in Fig. 2. At time $t = t_0$, the geometrical configuration $\underset{\sim}{x}_0$ of a deforming body is represented by a point Q. The point Q is arrived at from the point P whose configuration is given as $\underset{\sim}{x}_{0-1}$ at $t = t_{0-1}$, through the displacement field $\underset{\sim}{u}_{0-1}$ during a time step Δt, namely, $\underset{\sim}{x}_0 = \underset{\sim}{x}_{0-1} + \underset{\sim}{u}_{0-1}$. Therefore, the problem is to determine $\underset{\sim}{u}_{0-1}$, based on the information ($\underset{\sim}{x}_0$) at point Q. The solution scheme is as follows: taking a loading solution $\underset{\sim}{u}_0$ (forward) at Q, a first estimate of P can be made according to $p^{(1)} = \underset{\sim}{x}_0 - \underset{\sim}{u}_0$. Then, the loading solution $\underset{\sim}{u}_{0-1}^{(1)}$ can be calculated on the basis of the configuration of $p^{(1)}$ with which the configuration $\underset{\sim}{x}_0$ at Q can be compared with $p^{(1)} + \underset{\sim}{u}_{0-1}^{(1)} = Q^{(1)}$. If Q and $Q^{(1)}$ are not sufficiently close to each other, then $p^{(2)}$ can be estimated by $p^{(2)} = \underset{\sim}{x}_0 - \underset{\sim}{u}_{0-1}^{(1)}$. The solution for loading at $p^{(2)}$ is then $\underset{\sim}{u}_{0-1}^{(2)}$ and the second estimate of the configuration $Q^{(2)} = p^{(2)} + \underset{\sim}{u}_{0-1}^{(2)}$ can be made. The iteration is carried out until $Q^{(n)} = p^{(n)} + \underset{\sim}{u}_{0-1}^{(n)}$ becomes sufficiently close to Q. Displacement solutions are computed by the finite element method. The sufficient condition for convergence is that the body is plastically deforming at all times, if the boundary condition does not change at P and Q. We call this calculation scheme "Backward Tracing by FEM." So far, the concept includes only the geometry of deforming materials, and some questions as to its applicability to real problems arise immediately. Some of them are: (i) how to include the effect of material properties, such as work-hardening, strain-rate, and temperature effects; (ii) how to modify the method when the boundary conditions change; and (iii) the problem of solution uniqueness.

Although complete and satisfactory answers to these questions await further investigations, a test with axisymmetric compression of a cylinder demonstrates that the concept does work.

44

A circular cylinder of height-to-diameter ratio equal to 1 is compressed between two parallel platens with friction (friction factor, $m = 0.5$) to 10 percent reduction in height. The material is assumed to be rigid-perfectly plastic. In Fig. 3 the workpiece configuration at 10 percent reduction is shown by dotted lines as the result of rigid-plastic finite-element simulation of loading. Now, the backward tracing scheme was applied to the known configuration at 10 percent reduction in height. After the 10 percent axial displacement was traced backward, the result indeed gave the circular cylinder as the preform.

For both forward loading and backward tracing, a step size of 1% reduction in height was used. Because of the use of Newton-Raphson method in the finite-element program, iteration is involved in obtaining a loading solution (forward iteration), and another iteration is necessary in the backward tracing scheme (backward iteration). Numbers of iterations for each step of deformation were 6 ~ 7 and about 3 for forward and backward procedures respectively. Closeness of the two configurations $Q^{(n)}$ and Q was measured by $|\underset{\sim}{x}_0 - \underset{\sim}{x}_0^n|$ and the limit was set as 0.005 (mm), where $\underset{\sim}{x}_0^n$ represents the coordinates of the configuration of $Q^{(n)}$.

It should be noted that the process reversal (reverse loading) by reversing the direction (sign) of the boundary conditions does not trace the loading path backward, because the process reversal is a different boundary value problem from that of loading. Figure 3 shows that clearly the shape that is obtained by reverse loading did not result in the original circular cylinder.

4. APPLICATION TO SHELL NOSING

Preform design in forging is complex and generally involves many problems in applying the new approach. Less complex is the preform design in shell nosing, because the number of parameters in defining preform shapes is fewer.

In shell nosing, two simple preform configurations can be realized for a uniform wall thickness after nosing. The wall thickness distributions required in the preform can be accommodated by varying either the inner or the outer diameters of the preform. It is not difficult to see that different preform configurations can be arrived at by imposing different sequences of boundary conditions (such as where and when the nodal point in contact with the die should be freed from the die) during the backward process. This aspect of the problem is first investigated for non-workhardening materials. Then, using work-hardening materials, the procedure to include the effect of work-hardening is introduced in the new approach.

Rigid-perfectly plastic materials:

With reference to Fig. 4, specifications of the final nosed shell configuration are given by (unit; mm)

$L_f = 48.84$ $\quad r_o = 21.526$ $\quad b_f = 14.47$

$(L_o = 47.26)$ $\quad r_i = 14.648$ $\quad h_f = 6.88$ (uniform)

$R = 259$ $\quad (a_o = 237,\ b_o = 18.75)$

Coefficient of friction at the die-workpiece interface is assumed to be $\mu = 0.05$. For the finite element calculation, 40 four node elements and 63 nodal points are used. The criterion for controlling the boundary condition during the backward tracing depends on the preform shape under consideration.

For the preform shape with constant outer diamter (Type-O preform), $r_o^n = r_o$ for all n, where r_o^n is the radius of a nodal point located along the outer surface of the shell. The boundary condition for this type of preform is controlled in such a way that nodes which are in contact with the die ($r_o^n < r_o$) are freed from the die when the condition that $r_o^n = r_o$ is reached during the backward tracing.

For the preform shape with constant inner diameter (Type-I preform),

the criterion for changing the boundary condition is that as soon as $r_i^p = r_i$ for the nodes $r_i^p < r_i$, the boundary condition of the corresponding outside node is changed from that of die-contact to the force free condition, where r_i^p is the radius of a nodal point along the inner surface of the shell.

The above criteria, however, result in some errors because the deformation of the shell is not confined within the die, but extends beyond the die-entrance. In order to reduce the error, the criteria for change of the boundary condition are modified as

$$r_o^n = r_o - \Delta_o \quad \text{for Type-O preform}$$

$$r_i^p = r_i - \Delta_i \quad \text{for Type-I preform}$$

The amount Δ in the modified criteria can be estimated, for example, from the loading simulation of nosing with a preform of uniform wall thickness.

Using the modified criteria for controlling the boundary condition, the computation of backward tracing was carried out taking 2 mm penetration (in loading) as one step (total 22 steps to complete the calculation). Solution convergence needed about 6 ~ 7 iterations and for completing one step backward tracing 1 ~ 2 iterations for the case where boundary condition does not change, 2 ~ 3 iterations are required for the case where change in the boundary condition occurs. Convergence for backward tracing was determined by closeness of the solution within the limit of 0.005 (mm). The two types of preforms determined by the method are compared with the final nose configuration in Fig. 5. In Fig. 5, the lengths ξ_o^O and ξ_o^I, for Type-O and Type-I preforms, respectively, indicate the portion of the preform which becomes the nosed shell length L_f after nosing. Because the shell elongates during nosing, the preforms are shorter than the nosed shell. It can also be observed that the Type-O preform is slightly shorter than the Type-I preform. This is because the amount of deformation involved in nosing is more for Type-O than for

Type-I, and the total elongation is larger for the Type-O preform. The thickness distributions in the two preforms are compared in Fig. 6. The distributions are almost the same for both preforms, except that the thicknesses in Type-O are slightly smaller. This is reasonable based on the amount of deformation involved, and from the condition of volume constancy.

Work-hardening materials:

The following specifications of the nosed shall are used:

material = Al alloy 2024, annealed, with the stress-strain curve given by

$$\bar{\sigma} = 68.9\ (1.0 + 4.6(\bar{\varepsilon})^{0.29})\ \text{Mn/m}^2$$

Die geometry (mm): same ($R = 259$, $a_o = 237$, $b_o = 18.77$)

Shell dimensions (mm): $L_f = 36.84$, $b_f = 16.369$,

$r_o = 25.526$, $r_i = 14.648$, $h_f = 6.88$

Die-workpiece interface conditions: $\mu = 0$.

The shell configuration (in terms of total penetration) is different from the previous non-workhardening case. The reason for the use of different nosed shell specifications is that there exists a limit beyond which nosing cannot be continued and cylindrical part of the shell begins to deform. This limit depends on the work-hardening characteristics of the material, and the present specifications are selected within this limit.

In order to include the work-hardening effect in preform design, it is necessary to know the strain distributions in the nosed shell, in addition to the geometrical configurations, but the strain distributions in the nosed shell depend on the preform shapes, and are not known (or cannot be specified). In Fig. 7 the procedures to take into account the work-hardening effect in the

present approach are illustrated.

Applying the backward tracing scheme for non-work-hardening materials explained in the previous section, the two types of preforms can be determined. With these preforms the loading solutions are obtained for a work-hardening material. The results provide the strain (effective strain) distributions and the nosed shell configurations. The configurations are very close but not identical to the specifications. These configurations, mainly, the thickness distributions, are, then, corrected exactly according to the specifications, maintaining the same effective strain distributions. With these strain distributions, the application of the backward tracing scheme results in the preform shapes for a work-hardening material. At each step, the strain and corresponding stress are also traced backward following the stress-strain curve of the material. It should be mentioned that the first computational procedure in Fig. 7 may be eliminated by using approximate solutions [10] for preform shapes of non-work-hardening materials.

The number of iterations required was about the same as for non-work-hardening materials. However, solution convergence is somewhat sensitive to the size of time step, and a reduction of step size to 1 mm penetration was necessary. This step size required total 30 steps for completing the computations.

The effective strain distributions in the nosed shell obtained from loading solutions for both types of preforms are shown in Fig. 8. The strains are larger for Type-0 preform than for Type-I preform. The preforms for the work-hardening material were determined by applying the backward tracing scheme to the nosed shell with the strain distributions shown in Fig. 8, and the specified geometrical dimensions. The effective strains in the preforms were indeed negligible (within 0.1% strain), when the backward tracing calculation was completed. The thickness variations in the preform of the work-

hardening material is compared with that of non-work-hardening materials in Fig. 9(a) for Type-O preform and in Fig. 9(b) for Type-I preform. Fig. 9 shows that the preform shapes for work-hardening and non-work-hardening materials are almost identical to each other for both preform types. It may be due to the fact that the total penetration of the shell into the die is so small that the work-hardening effect is negligible for this specific case. Nevertheless, it suffices to show the procedure to include the work-hardening characteristics of the material in the backward tracing technique.

5. CONCLUDING REMARKS

A new technique, called backward tracing scheme, was devised for preform design. This is a unique application of the finite element method to the problems in metal forming. It was demonstrated that the technique can be applied to preform design in shell nosing. It was also revealed that one of the critical aspects for further development of the technique concerns with the treatment of the boundary conditions. The boundary conditions for non-steady state forming processes change during loading, and the way in which this change occurs depends on the preform shapes. Thus, the criterion for the selection of desired (or optimum) preform are needed, and then the condition for controlling the boundary conditions, corresponding to a selected preform must be developed.

A challenge to this new approach for further development, thus, lies in its application to preform design in forging.

ACKNOWLEDGEMENTS

The authors wish to thank the Army Research Office, for its contract No. DAAG 29-79-C-0217 and the National Science Foundation for its grant NEA-8112843 under which the present investigation was carried out. They also wish to thank Mrs. Carmen Marshall for typing the manuscript.

REFERENCES

1. S. K. Biswas and W. A. Knight, "Computer-aided design of axisymmetric hot forging dies," Proc. 15th Int. MTDR Conference, 1974, pp. 135-143.

2. K. Von Spies, "Intermediate forms in drop forging and their production by roll forming," West Deutscher Verlag, Cologne, 1959. (Translated by Ministry of Technology, 1969).

3. A. Chamouard, Estampage et Forge, 1964, Dunod (Paris).

4. N. Akgerman, J. R. Becker, and T. Altan, "Preform design in closed die forging," Metallurgia and Metal Forming, Vol. 40, 1973, p. 135.

5. A. Nadai, "Plastic state of stress in curved shells: The forces required for forging of the nose of high-explosive shells," Forging of Steel Shells, presented at the annual meeting of the ASME, New York, November 29 through December 3, 1943.

6. R. K. Carlson, "An experimental investigation of the nosing of shells," Forging of Steel Shells, presented at the annual meeting of the ASME, New York, November 29 through December 3, 1943.

7. G. D. Lahoti, T. L. Subramanian and T. Altan, "Development of a computerized mathematical model for the hot/cold nosing of shells," Report ARSCD-CR-78019 to U.S. Army Research and Development Command, September 1978.

8. S. Kobayashi, "A Review on the Finite Element Method and Metal Forming Process Modeling," J. App. Metalworking, Vol. 2, No. 3, 1982, p. 1.

9. S. I. Oh, "Finite Element Analysis of Metal Forming Processes with Arbitrarily Shaped Dies," Int. J. Mech. Sci., Vol. 24, 1982, p. 479.

10. S. Kobayashi, "Approximate Solutions for Preform Design in Shell Nosing," submitted to Int. J. Mach. Tool Des. Res., 1982.

FIGURE TITLES

Figure 1(a) Preforms for finish forgings of various H-shapes.

Figure 1(b) Preform for 155 mm shell.

Figure 2 Concept of the backward tracing scheme.

Figure 3 Test of the backward tracing scheme for compression of a circular cylinder.

Figure 4 Die dimensions and nosed shell configuration.

Figure 5 Nosed shell configuration and two types of preform shapes for non-work-hardening materials.

Figure 6 Thickness distributions in the two preforms (non-work-hardening materials).

Figure 7 Schematic illustration of the procedures to include the work-hardening effect in preform design.

Figure 8 The effective strain distributions in the nosed shell based on the two types of preform shapes.

Figure 9 Comparison of the thickness distributions for non-work-hardening and a work-hardening (Al alloy 2024 annealed) materials in (a) the Type-0 preform and (b) the Type-I preform.

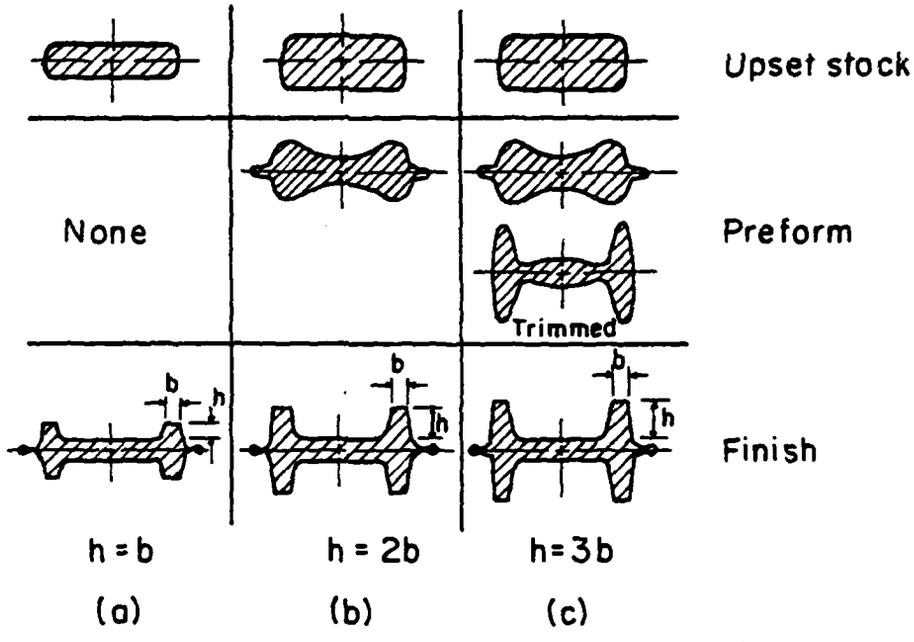

Figure 1(a) Preforms for finish forgings of various H-shapes.

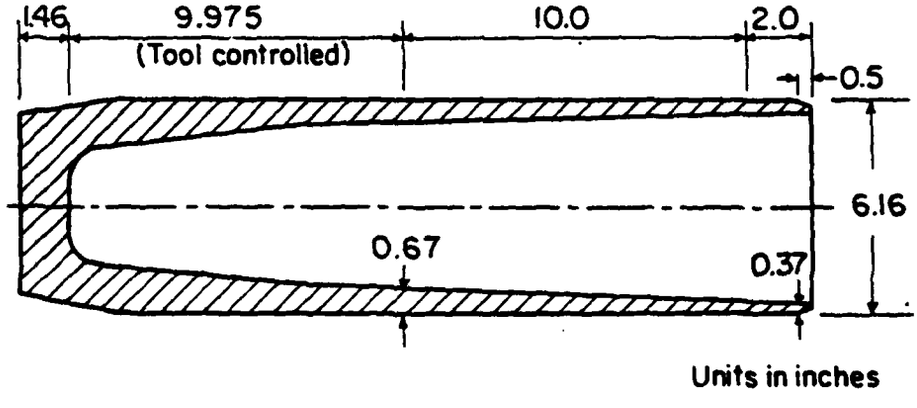

Figure 1(b) Preform for 155 mm shell.

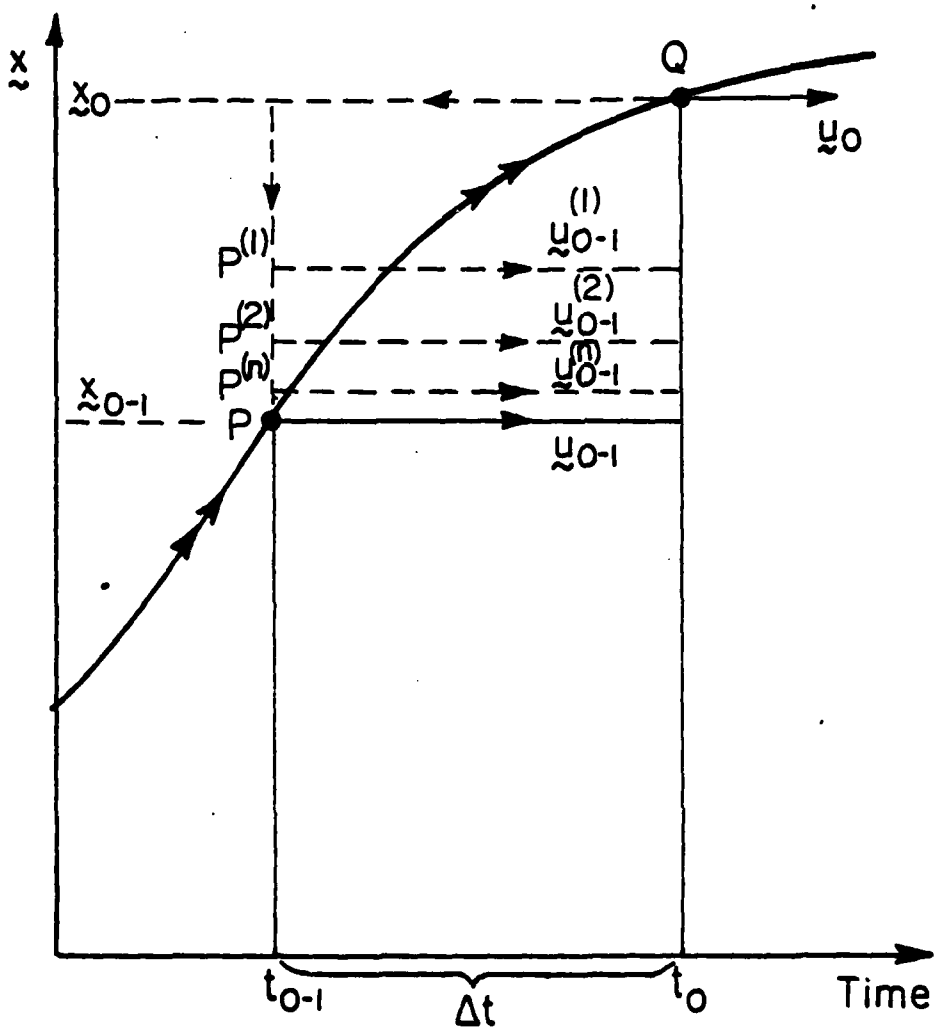

Figure 2 Concept of the backward tracing scheme.

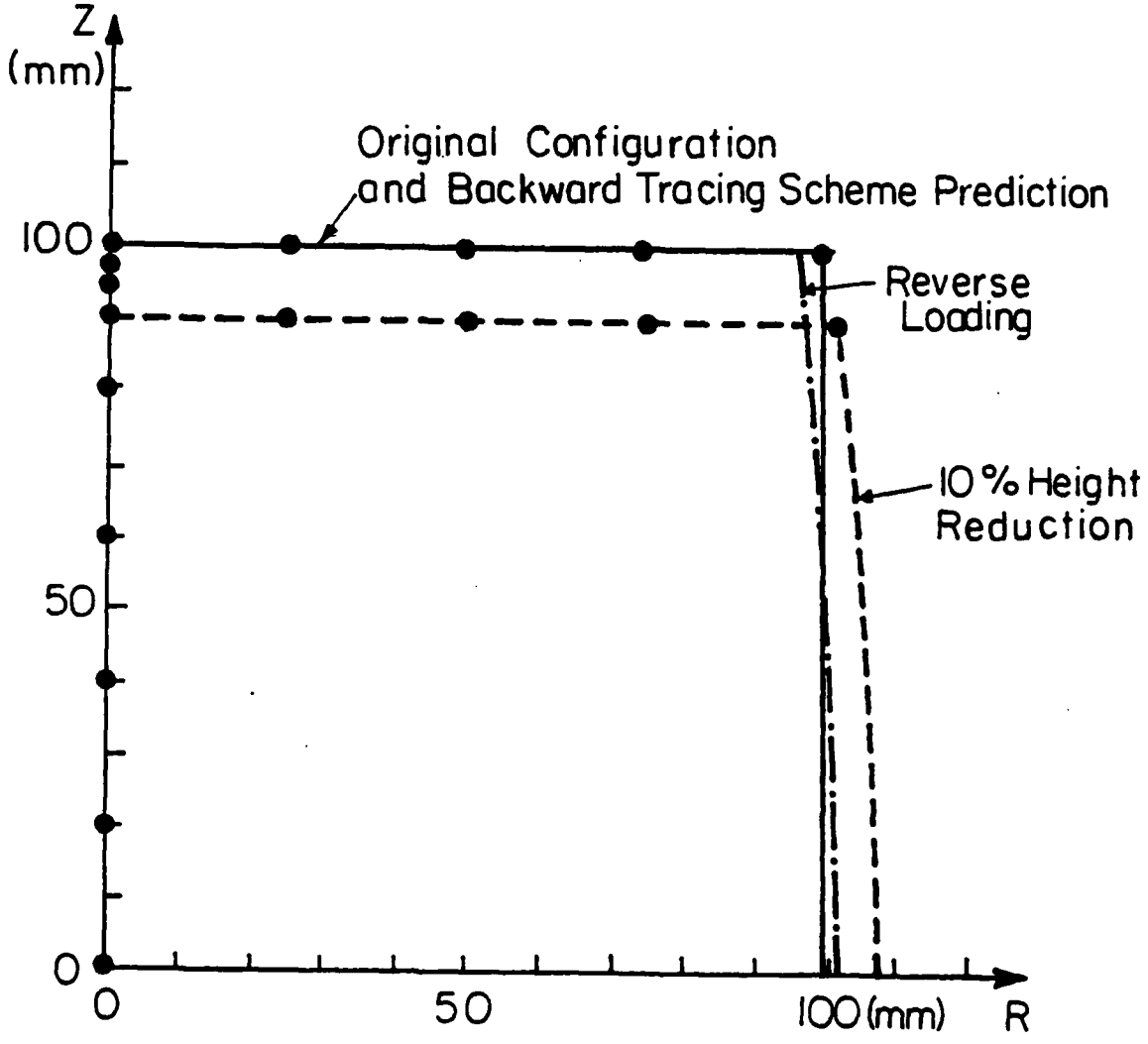

Figure 3 Test of the backward tracing scheme for compression of a circular cylinder.

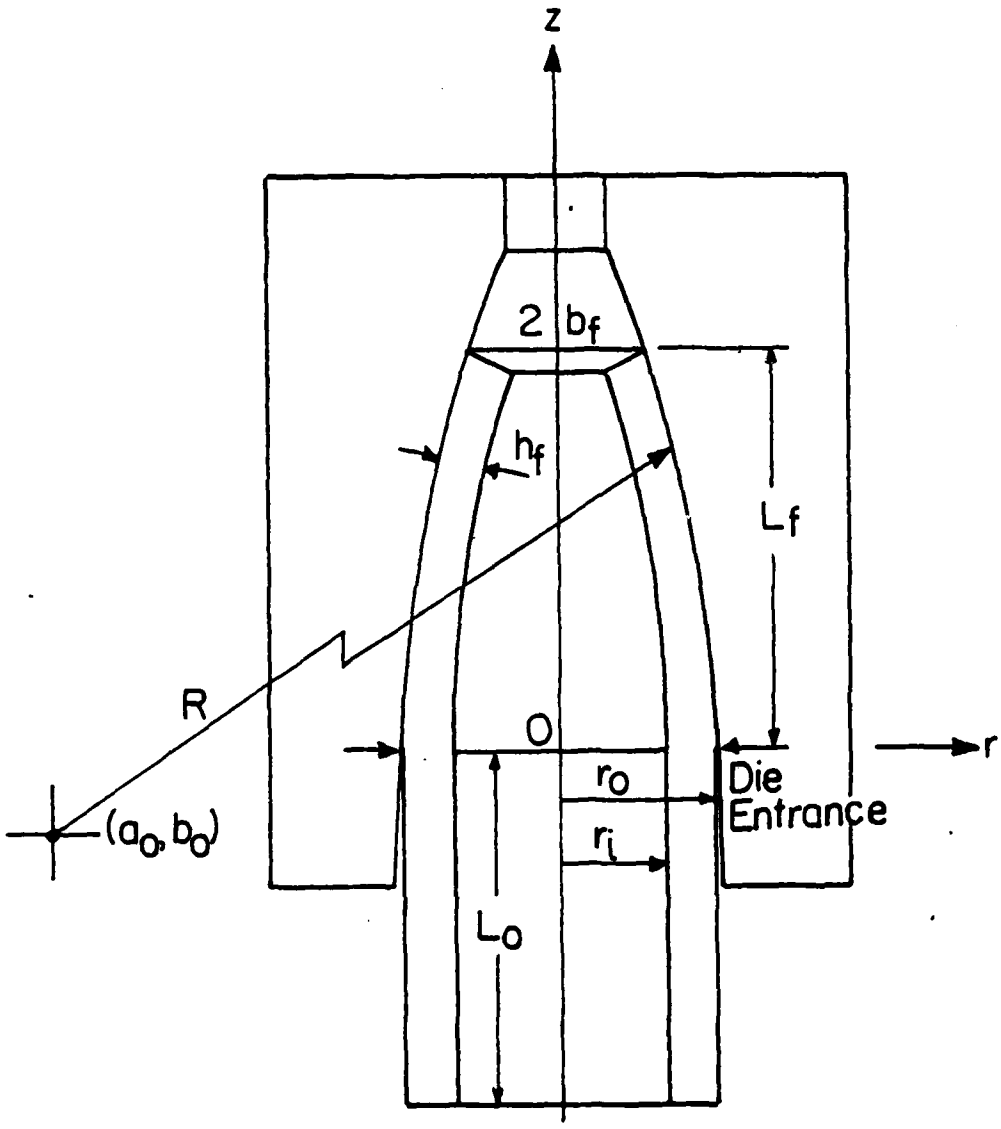

Figure 4 Die dimensions and nosed shell configuration.

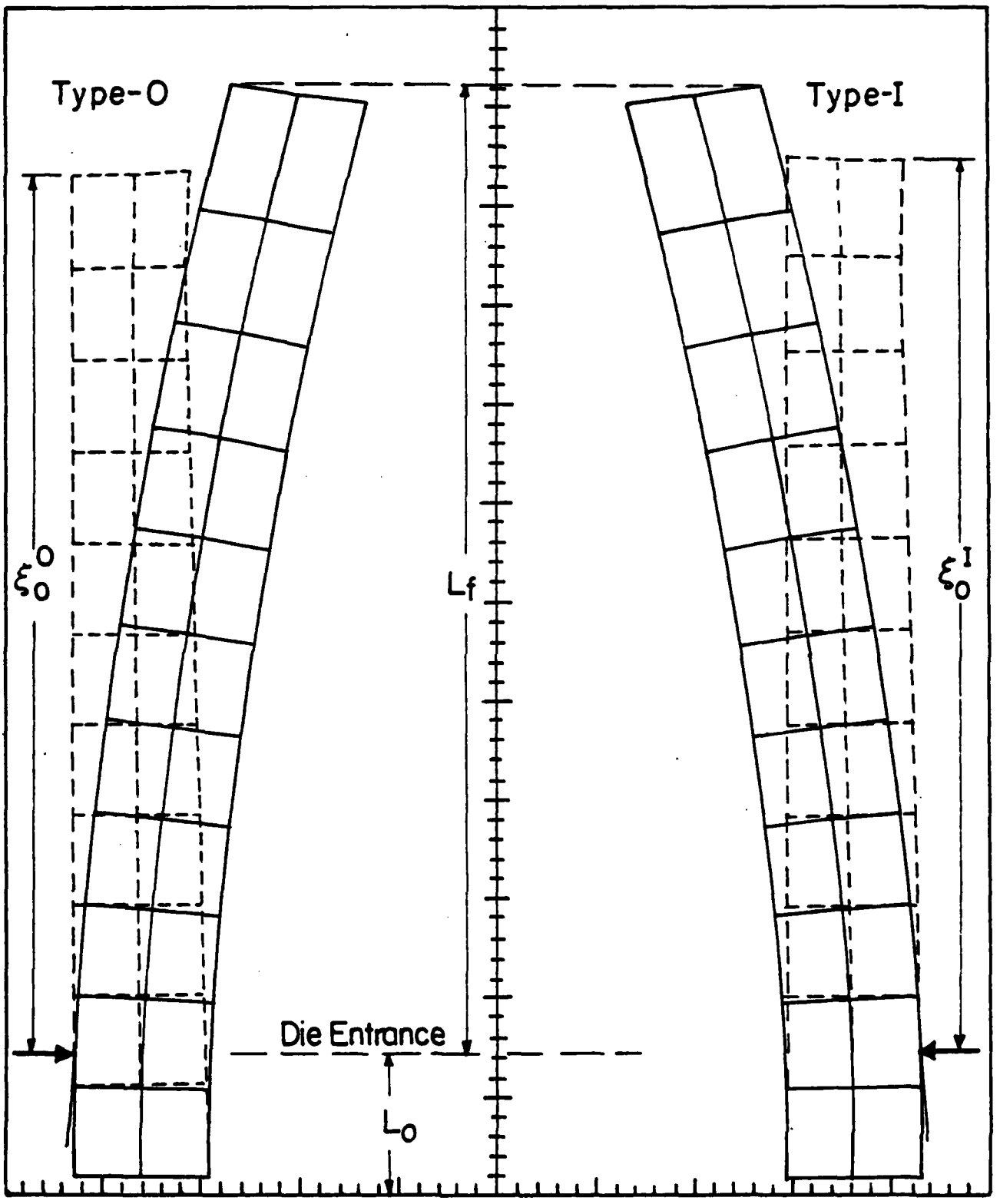

Figure 5 Nosed shell configuration and two types of preform shapes for non-work-hardening materials.

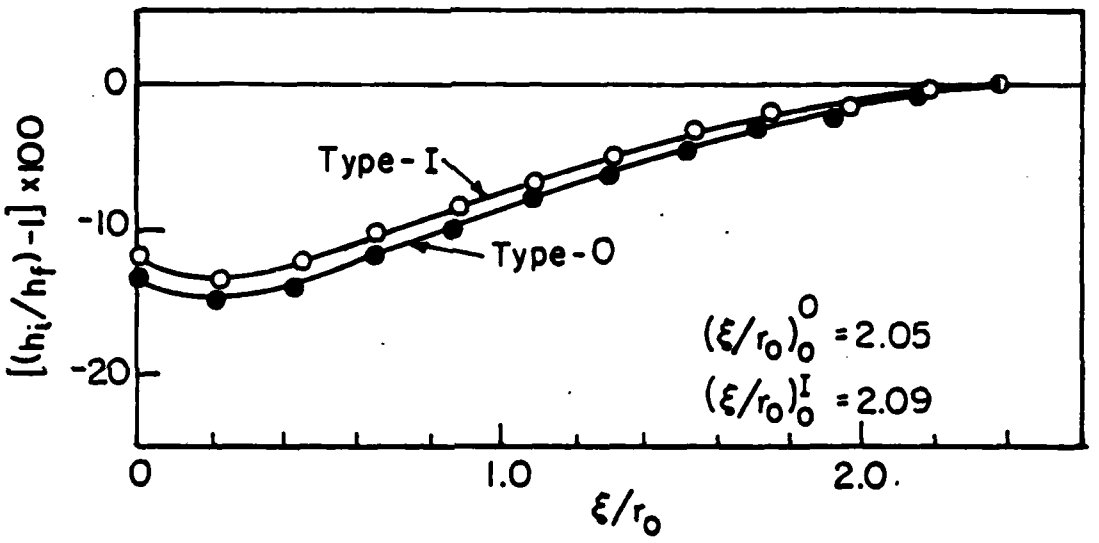

Figure 6 Thickness distributions in the two preforms (non-work-hardening materials).

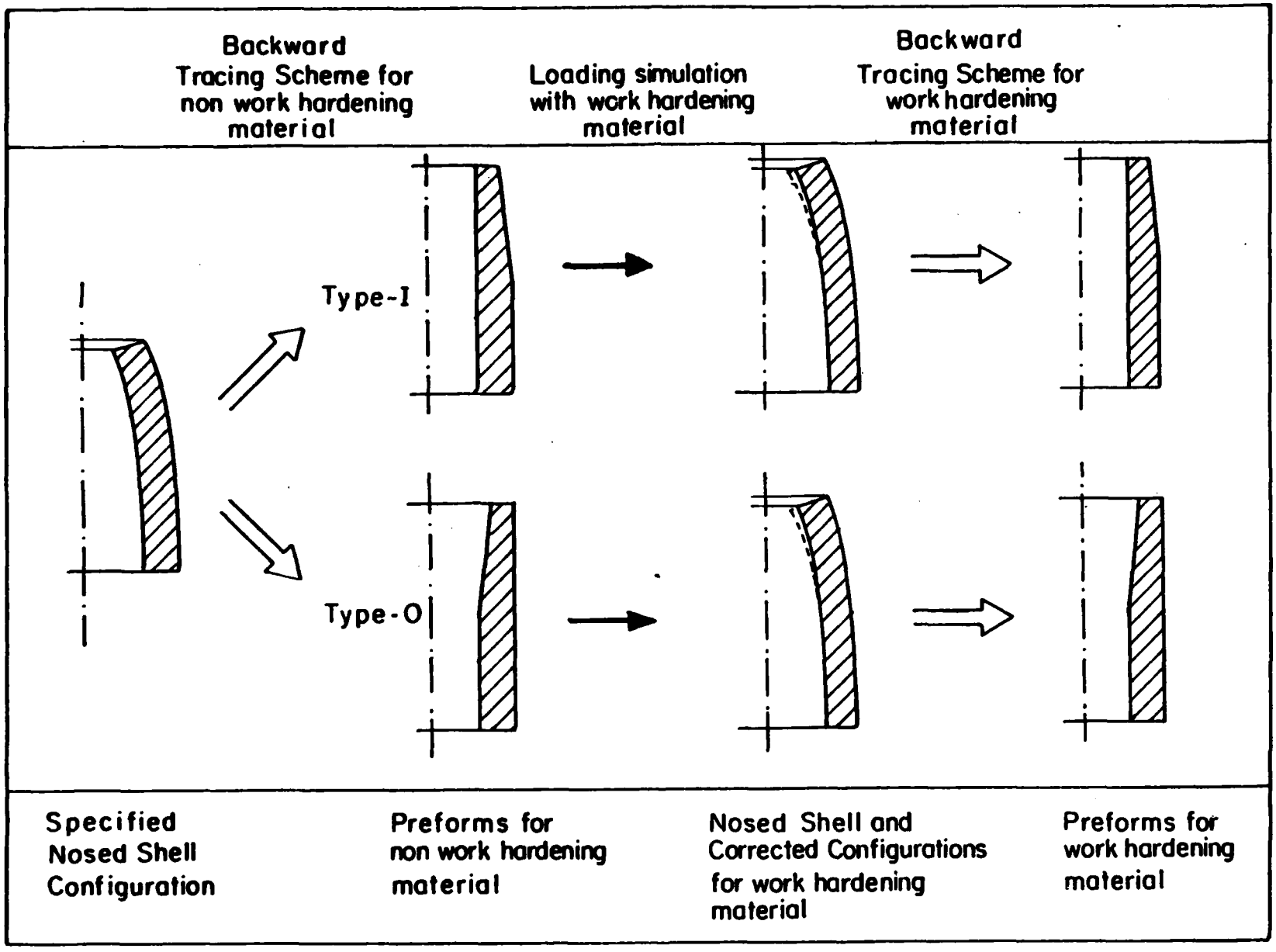

Figure 7 Schematic illustration of the procedures to include the work-hardening effect in preform design.

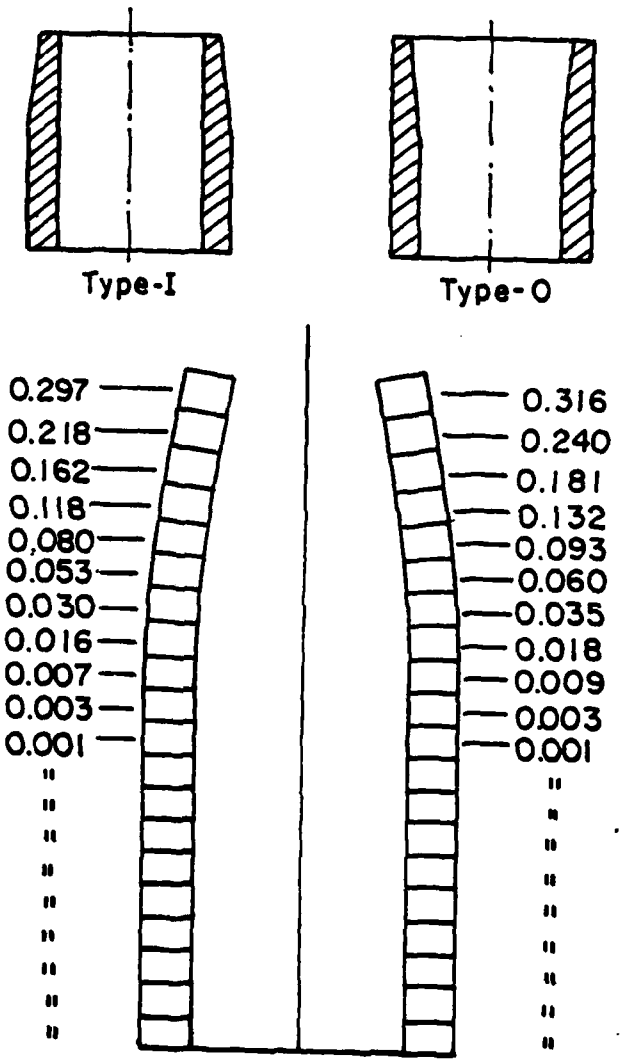

Figure 8 The effective strain distributions in the nosed shell based on the two types of preform shapes.

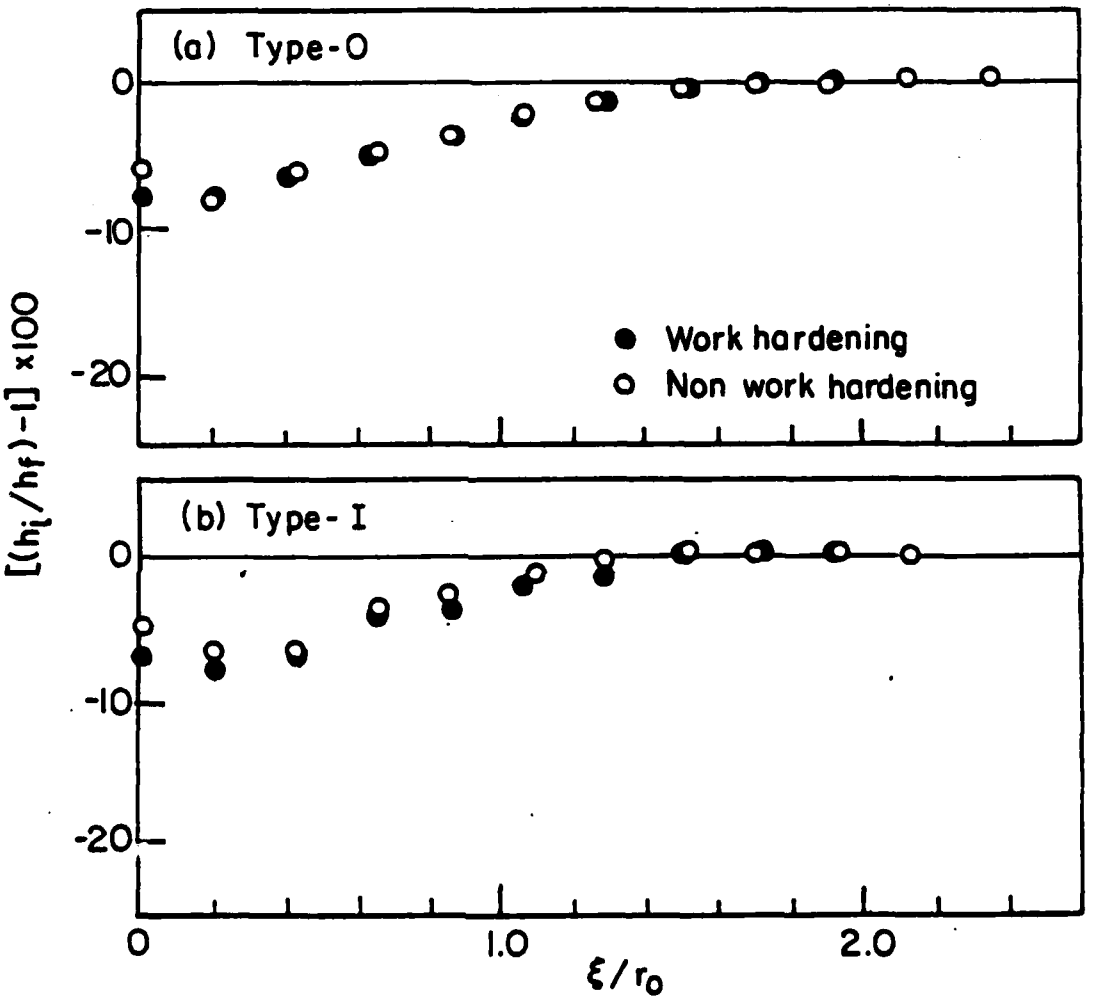

Figure 9 Comparison of the thickness distributions for non-work-hardening and a work-hardening (Al alloy 2024 annealed) materials in (a) the Type-O preform and (b) the Type-I preform.

#7.

APPROXIMATE SOLUTIONS FOR PREFORM DESIGN IN SHELL NOSING*

by

Shiro Kobayashi
Department of Mechanical Engineering
University of California
Berkeley, California

ABSTRACT

Two approximate solutions for preform design in shell nosing are derived. The degree of approximation was examined by the accurate numerical solution based on the new approach by the finite element method, for an example of uniform wall thickness of the nosed shell. It was demonstrated that both approximate solutions are useful in design, one for its simplicity and the other for its accuracy. The approximate solutions presented here will also be helpful for the further development of the new approach to preform design in shell nosing.

---

* Part 2 of "Preform Design in Metal Forming."

62

Nomenclature

r, θ, z	- radial, circumferential and axial coordinates in the cylindrical system
s	- coordinate along the die contour
ϕ	- angular coordinate
ϕ_b	- the value of ϕ corresponding to the nose tip where the reaius is equal to b
V_s	- velocity in the s-direction
σ_s, σ_θ	- stress components in the s-direction and the circumferential direction, respectively
σ_o	- flow stress (constant) of the material
$\dot{\varepsilon}_s, \dot{\varepsilon}_\theta, \dot{\varepsilon}_n$	- strain-rate components in the s-direction, the circumferential direction and the thickness direction, respectively
R	- radius of the die contour
a_o, b_o	- r, z - coordinates for the center of radius of the die contour
L_p	- length of the preform
r_o, s_o	- r coordinate and corresponding s coordinate at the entrance of the die
h_i, h	- tube thicknesses in the preform and in the nosed shell, respectively
b, B	- radius and corresponding s-value at the nose tip of the shell
b_ξ, B_ξ	- radius and corresponding s-value at the nose tip of the shell when an element ξ just begins to deform
ξ	- axial coordinate in the preform
t	- time
f	- subscript referring to the final configuration

1. INTRODUCTION

Shell nosing is the process of forming an ogive nose at an open end of a tubular part by pressing the tube into a suitably formed die. The internal cavity of a tubular part (preform) is formed to finished shape through a series of piercing and drawing operations, and the open end of the preform is then contoured by a nosing press, as shown in Fig. 1. The metal flow in nosing is complex. In general, wall thickness increases, but the shell may elongate or shrink in length after the operation, depending upon friction. Understanding the deformation mechanics of the process is an essential step toward the control of metal flow and proper design of the process.

Because shell specifications require certain wall thickness distributions after nosing, the design of the preform with which the desired shape after the nosing operation can be achieved is a very important problem. For certain shells, uniform wall thickness is required, whereas, in other shells, wall thickness distribution after nosing is defined by two ogive radii.

For shells with uniform wall thickness after nosing, Nadai [1] outlined an approach for designing the preforms based on the strains in the shell nose. Using Nadai's approach, Carlson [2] suggested the method for determining the original shell profile, knowing the final shape. The formulation for the distribution of thickness in the preform was derived from the geometry of deformed configurations and assumed distributions of the strains. Thus, the final expression for the determination of preform thicknesses requires an estimate of a quantity, for example, elongation at the tip of the nose. Lahoti et al. [3] developed the computer program for the preform design procedure based on Carlson's method. Tang et al. [4], assuming that the strain distributions that resulted from the finite-element simulation are valid for preforms having nonuniform wall thickness, designed two types of preform

64

shapes to obtain uniform wall thicknesses after nosing. In this paper two approximate solutions for designing the preforms are presented. The degree of approximation of the solution is examined by the accurage numerical solution based on a new approach by the finite element method [5], for the case of uniform wall thickness of the nosed shell.

2. PRELIMINARIES

Figure 2 shows the die geometry and the coordinate system. In the cylindrical coordinate system (r, z, θ) with the origin O at the die entrance, the die contour is expressed as $r = R \sin\phi - a_o$, and $z = R \cos\phi - b_o$. The coordinate s measures the distance along the die contour from the origin O' where r = 0. With reference to Fig. 2, and using the notation given in the nomenclature, the basic equations for shell deformation are given by

(i) equilibrium equation

$$\frac{\partial}{\partial r}(h\,\sigma_s) + \frac{h}{r}(\sigma_s - \sigma_\theta) = 0 \tag{1}$$

(ii) yield condition (plane stress)

$$\sigma_s^2 - \sigma_s\,\sigma_\theta + \sigma_\theta^2 = \sigma_o^2 \tag{2}$$

(iii) flow rule

$$\frac{\dot{\varepsilon}_s}{2\,\sigma_s - \sigma_\theta} = \frac{\dot{\varepsilon}_\theta}{2\,\sigma_\theta - \sigma_s} = \frac{\dot{\varepsilon}_h}{-(\sigma_\theta + \sigma_s)} \tag{3}$$

where strain-rates are defined as

$$\left.\begin{aligned} \dot{\varepsilon}_s &= \frac{\partial V_s}{\partial s} = \frac{\partial V_s}{\partial r}\cos\phi \\ \dot{\varepsilon}_\theta &= \frac{V_s}{r}\cos\phi \qquad (V_s < 0) \\ \dot{\varepsilon}_h &= \frac{\dot{h}}{h} \end{aligned}\right\} \tag{4}$$

Since the thickness h in general is a function of coordinate and time t, the incompressibility condition is written as [6,7]

$$\frac{1}{h}\frac{Dh}{Dt} + \frac{\partial V_s}{\partial r}\cos\phi + \frac{V_s}{r}\cos\phi = 0 \tag{5}$$

where $\frac{D}{Dt} \equiv \frac{\partial}{\partial t} + V_s \cos\phi \frac{\partial}{\partial r}$

Note that if h is a function of space variables only, eq. (5) is reduced to

$$\frac{d}{dr}(h\, r\, V_s) = 0 \tag{5a}$$

In Fig. 3 the initial and the two configurations of the shell nose are shown. Figure 3(b) shows the configuration of shell nose at a time when the element ξ just begins to deform, and characterized by the radius of nose tip denoted by $b = b_\xi$. Identifying an element in the initial and the deformed configurations, the incompressibility equation can be written as

$$h \cdot r \cdot ds = h_i \cdot r_o \cdot d\xi \qquad (b, \text{ constant}) \tag{5b}$$

and

$$\frac{h_i}{h} = \frac{r}{r_o}\,\frac{ds}{d\xi}\,. \tag{6}$$

When the final configuration is specified, the radius of nose tip b is given and h is known as a function of r. Thus the problem essentially is to determine the relationship between the corresponding coordinates in the initial and final configurations, namely, the relations between ξ and s (or ξ and r).

3. APPROXIMATE SOLUTION

Procedures:

Taking the magnitude of the velocity V_s at the nose tip as unity, the nose tip coordinate B (or b) can be used as the time scale ($dt = -dB = -db/\cos\phi_b$). Then, applying the condition that $B = s_o$ at $\xi = 0$ and $B = B_\xi$

at ξ, we have

$$\xi = \int_{s_o}^{B_\xi} (V_s)_{s=s_o} \, dB \tag{7}$$

From the definition of the velocity V_s,

$$|V_s| = \left(\frac{ds}{dB}\right)_\xi \tag{8}$$

with the initial condition that $s = s_o$ at $B = B_\xi$. The subscript ξ in eq. (8) denotes an element ξ. Thus, the relationship between ξ and s (or ξ and r) can be obtained by eliminating B_ξ from eqs. (7) and (8), when the velocity V_s is known. The determination of the velocity V_s is achieved from

$$\frac{\partial V_s}{\partial r} = \frac{2\sigma_s - \sigma_\theta}{2\sigma_\theta - \sigma_s} \left(\frac{V_s}{r}\right) \tag{9}$$

resulting from eqs. (3) and (4).

Integration of eq. (9), with approximate stress solutions [8], given by $\frac{\sigma_s}{\sigma_o} \simeq - \ell n \frac{r}{b}$, and $\frac{\sigma_\theta}{\sigma_o} \simeq - 1$, results in

$$|V_s| = \left(\frac{b}{r}\right)^2 \left(1 - \frac{1}{2} \ell n \frac{r}{b}\right)^{-3} \tag{10}$$

The derivation of Eq. (10) is given in the Appendix. In order to perform integration of V_s, involved in Eqs. (7) and (8), further approximation of the velocity solution (10) is necessary, and the final solution for pre-form shapes depends on this approximation.

Solution I:

A simple approximation [9] for the velocity V_s is given by

$$|V_s| = \sqrt{\frac{b}{r}} \tag{11}$$

The velocity distributions given by eqs. (10) and (11) are compared in Fig. 4. Substituting eq. (11) into eq. (7)

$$\xi = \int_{r_o}^{b_\xi} \left(-\sqrt{\frac{b}{r_o}}\right) \frac{db}{\cos\phi_b} = \frac{1}{\sqrt{r_o}} [G(r_o) - G(b_\xi)] \tag{12}$$

with

$$G(x) = \int \frac{\sqrt{x}}{\sqrt{1-\left(\frac{x+a_o}{R}\right)^2}}\, dx$$

From eq. (8)

$$|V_s| = \frac{dr}{db} \frac{\cos\phi_b}{\cos\phi} = \sqrt{\frac{b}{r}}$$

Integrating from r_o to r for r and from b_ξ to b for b, we have

$$G(r) - G(r_o) = G(b) - G(b_\xi) \tag{13}$$

Eliminating b_ξ from eqs. (12) and (13), we obtain

$$\xi = \frac{1}{\sqrt{r_o}} [G(r) - G(b)] \tag{14}$$

From eq. (6) $\frac{h_i}{h} = \frac{r}{r_o} \frac{dr}{d\xi \cos\phi}$ for b = constant, but $\frac{dr}{d\xi} = \sqrt{r_o} \Big/ \frac{dG(r)}{dr} = \sqrt{\frac{r_o}{r}} \cos\phi$ from eq. (14).

Thus $$\frac{h_i}{h} = \sqrt{\frac{r}{r_o}} \tag{15}$$

It is of interest to note in eq. (15) that h is not a function of time and can also be obtained directly from the incompressibility condition (5a) with the velocity V_s given by eq. (11). Noting that usually $a_o + r_o \simeq R$ and $\cos\phi \simeq \sqrt{2 \frac{r_o}{R} (1 - \frac{r}{r_o})}$, the expression for ξ in eq. (14) becomes

$$\frac{\xi}{r_o} = \sqrt{\frac{R}{2r_o}} \left[\sin^{-1}\sqrt{\frac{r}{r_o}} - \sqrt{\frac{r}{r_o}}\sqrt{1 - \frac{r}{r_o}} - \sin^{-1}\sqrt{\frac{b}{r_o}} + \sqrt{\frac{b}{r_o}}\sqrt{1 - \frac{b}{r_o}}\right] \tag{16}$$

The derivation of eq. (16) is given in the Appendix.

68

The solution for a preform shape is given by eqs. (15) and (16). The quantities h, r and b in the equations refer to those of given configuration after nosing, namely, h_f, r_f and b_f .

Solution II:

The solution II is based on the approximate velocity distribution expressed as

$$|V_s| = \left(\frac{r}{b}\right) \frac{1 - \frac{1}{2} \ell n \frac{r}{b}}{1 + \ell n \frac{r}{b}} \tag{17}$$

Equation (17) is also compared with the velocity distribution given by eq. (10) in Fig. 4. It can be seen in Fig. 4 that this approximation is better than a simple one used for solution I. In order to perform integrations involved in the solution procedure, further approximation must be made, particularly, with reference to the relation between s and r. It is assumed that

$$\frac{dr}{ds} = \cos\phi \approx \cos\phi_m \ (= \text{const}) \tag{18}$$

over the range $b_f \leq r \leq r_o$ where ϕ_m is an average value of ϕ over the relevant range.

With this assumption, eq. (7) becomes

$$\xi = \int (V_s)_{s=s_o} dB = \int (V_s)_{r=r_o} \frac{db}{\cos\phi_b} = -\frac{1}{\cos\phi_m} \int_{r_o}^{b_\xi} \left(\frac{r_o}{b}\right) \left(\frac{1 + \frac{1}{2} \ell n \frac{b}{r_o}}{1 - \ell n \frac{b}{r_o}}\right) db$$

If we define an average value ϕ_m , according to

$$\cos\phi_m = \frac{1}{b_f - r_o} \int_{r_o}^{b_f} (\cos\phi)\, dr \tag{19}$$

with $\cos\phi \cong \sqrt{2 \frac{r_o}{R} \left(1 - \frac{r}{r_o}\right)}$,

then,

$$\frac{\xi}{r_o} = \sqrt{\frac{R}{2r_o}} \cdot \frac{(3/2)}{\sqrt{1 - \frac{b_f}{r_o}}} \left(\frac{1}{2}\right) \ell n \left[\frac{b_\xi}{r_o} \left(1 - \ell n \frac{b_\xi}{r_o}\right)^3 \right] \tag{20}$$

For derivation of eq. (20), see the Appendix. Equation (20) gives the relation between b_ξ and ξ for given die deminsions and nosed shell configuration. Equation (8), with the assumption given by eq. (18), now becomes

$$\left(\frac{ds}{dB}\right)_\xi = \left(\frac{dr}{db}\right)_\xi = |V_s| \ ,$$

and its integration (given in the Appendix) results in

$$r \sqrt{b} \ \ell n \frac{b}{r} = r_o \sqrt{b_\xi} \ \ell n \frac{b_\xi}{r_o} \tag{21}$$

The thickness ratio given by eq. (6), according to eqs. (20) and (21), becomes

$$\frac{h_i}{h} = \frac{r}{r_o} \sqrt{\frac{b_\xi}{b}} \left(\frac{1 - \ell n \frac{b_\xi}{r_o}}{1 - \ell n \frac{b}{r}} \right) \tag{22}$$

The derivation of eq. (22) is given in the Appendix. Equations (20), (21) and (22), if we use h_f, r_f and b_f for the corresponding quantity, constitute the solution II for preform design. In passing it is to be noted that the thickness change expressed by eq. (22) resembles that of the flange in deep drawing obtained by Hill [6]. It should be further noted that the thickness h given by eq. (22) is not only dependent on r but also a function of time (b) and satisfies incompressibility condition (5) with the approximation (18).

4. NUMERICAL EXAMPLE AND DISCUSSION

The preform dimensions (h_i as a function of ξ) are calculated using the approximate solutions obtained in the previous section, for the case of uni-

70

form thickness after nosing.

The specifications for the die geometry and the nosed shell dimensions (unit: mm) are as follows:

$R = 259.00$ $(R/r_o = 12.03)$ $(a_o = 237.20,\ b_o = 18.75)$

$r_o = 21.53,\ b_f = 14.47$ $(b_f/r_o = 0.671)$

$h_f = h_o = 6.90,\ L_f = 48.84$ $(L_f/r_o = 2.27)$

The computation for the preform dimensions with Solution I is straight forward, and the results for the above specifications are tabulated in Table 1 and shown graphically in Fig. 5a.

Table 1. Preform Dimensions According to Solution I.

r/r_o	ξ/r_o	h_i/h_f	$-(h_i/h_f - 1) \times 100$
0.671	0.000	0.819	18.1
0.700	0.105	0.837	16.3
0.725	0.202	0.851	14.9
0.750	0.304	0.866	13.4
0.775	0.414	0.880	12.0
0.800	0.532	0.894	10.6
0.825	0.660	0.908	9.2
0.850	0.799	0.922	7.8
0.875	0.953	0.935	6.5
0.900	1.125	0.949	5.1
0.925	1.323	0.962	3.8
0.950	1.562	0.975	2.5
0.975	1.877	0.987	1.3
1.000	2.649	1.000	0

The preform dimensions according to Solution II are calculated by determining b_ξ/r_o for given r/r_o from eq. (21) first, and then from eqs. (20) and (22). The computed results are given in Table 2.

Table 2. Preform Dimensions According to Solution II.

r/r_o	b_ξ/r_o	ξ/r_o	h_i/h_f	$-(h_i/h_f - 1) \times 100$
0.671	1.000	0.000	0.819	18.1
0.700	0.976	0.155	0.830	17.0
0.725	0.954	0.291	0.841	15.9
0.750	0.932	0.431	0.852	14.8
0.775	0.908	0.574	0.864	13.6
0.800	0.885	0.719	0.877	12.3
0.825	0.860	0.866	0.891	10.9
0.850	0.835	1.016	0.905	9.5
0.875	0.809	1.167	0.920	8.0
0.900	0.783	1.320	0.935	6.5
0.925	0.756	1.475	0.951	4.9
0.950	0.728	1.632	0.967	3.3
0.975	0.700	1.790	0.984	1.6
1.000	0.671	1.950	1.000	0

The preform dimensions tabulated in Table 2 are plotted in Fig. 5b.

For preform design in shell nosing, the accurate solution can be obtained by a new approach - Backward Tracing Scheme - using the finite element method [5]. The concept involved in the approach is to trace the loading path backward from the final configuration by the rigid-plastic finite element method. The two preforms, one having distributed inner radii and the other with a cylindrical inner surface, were designed for the present example. The results are almost the same for the two types of preforms, and the preform dimensions for the case where the outer diameter of the preform is constant, are given in Table 3.

72

Table 3. Preform Dimensions - Numerical Solution.

ξ/r_o	h_i/h_f	$-(h_i/h_f - 1) \times 100$
0	0.861	13.9
0.220	0.846	15.4
0.435	0.857	14.3
0.650	0.878	12.2
0.863	0.897	10.3
1.076	0.917	8.3
1.288	0.932	6.8
1.500	0.952	4.8
1.710	0.968	3.2
1.920	0.974	2.6
2.130	0.987	1.3
2.350	0.996	0.4

The degree of approximation of the solutions I and II, therefore, can be examined by comparing them with the accurate finite element solution. A comparison of these solutions is shown in Fig. 6. It is seen that the approximate solution II gave an excellent estimate of preform dimensions for the most of the length, except near the preform tip. Approximate solution I deviates from the numerical solution somewhat, however, simplicity is its strength. Another important dimension of the preform, besides the thickness distribution, is the total length of the preform. In Fig. 6, $(\xi/r_o)_o$ is the length of the part which goes into the die after nosing. Thus the total length of the preform L_p is given by the sume of $(\xi)_o$ and the constant L_o.

Solution I over-estimate the total length, but solution II again, is very close to the numerical solution. It is seen that in the numerical solution the thickness at $(\xi/r_o)_o$ is slightly smaller than the final thickness. This reflects the fact that the actual deformation zone extends beyond the die entrance during nosing.

5. CONCLUDING REMARKS

The two approximate solutions for preform design in shell nosing were derived, and it was shown that they are both useful in design, particularly, one for its simplicity and the other for its accuracy. The examination of approximation was possible, because of the new numerical approach to the problem by the finite element method. The approximate solutions in this paper do not take into account the effects of interface friction and material properties. In this respect, the new approach will assume increasing importance in preform design in the future. However, the approximate solutions developed here will be useful in production at the present time. Also, it is anticipated that the approximate solutions can play a role during the course of further development of the new approach as an initial solution from which the final solution will converge by iteration.

ACKNOWLEDGEMENTS

The author wishes to thank the Army Research Office for its contract No. DAAG 29-79-C-0217 under which this investigation was possible. He also wishes to thank Mrs. Carmen Marshall for typing the manuscript. Mr . S. M. Hwang's assistance in computation is appreciated.

REFERENCES

1. A. Nadai, "Plastic state of stress in curved shells: The forces required for forging of the nose of high-explosive shells," Forging of Steel Shells, presented at the annual meeting of the ASME, New York, November 29 through December 3, 1943.

2. R. K. Carlson, "An experimental investigation of the nosing of shells," Forging of Steel Shells, presented at the annual meeting of the ASME, New York, Nobember 29 through December 3, 1943.

3. G. D. Lahoti, T. L. Subramanian and T. Altan, "Development of a computerized mathematical model for the hot/cold nosing of shells," Report ARSCD-CR-78019 to U.S. Army Research and Development Command, September 1978.

74

4. M. C. Tang, M. Hsu and Shiro Kobayashi, "Analysis of Shell Nosing - Process Mechanics and Preform Design," to be published in Ing. J. Mach. Tool Des. Res., 1982.

5. J. J. Park, N. Rebelo and Shiro Kobayashi, "A New Approach to Preform Design in Metal Forming - Application of the Finite Element Method," submitted for publication in Int. J. Mach. Tool Des. Res., 1982.

6. R. Hill, The Mathematical Theory of Plasticity, Oxford University Press, 1950.

7. Y. Yamada, "Studies on Formability of Sheet Metals," Report of the Institute of Industrial Science, University of Tokyo, Vol. 11, No. 5, Dec. 1961.

8. M. Singh, "A Linearized Theory of Nosing of Shells," J. Applied Mechanics, Sept. 1964, p. 535.

9. R. Karpp, P. Gordon and F. M. Lee, "Mechanics of Hot Nosing of Shell," Proceedings of 5th North American Metalworking Research Conferences, May, 1977, pp. 179-182.

APPENDIX

Derivations of the Equations

(1) Derivation of Eq. (10).

Substitution of approximate stress solutions given by $\frac{\sigma_s}{\sigma_o} \simeq - \ell n \frac{r}{b}$ and $\frac{\sigma_\theta}{\sigma_o} \simeq - 1$, into equation (9), results in

$$\frac{dV_s}{V_s} = \left(- 2 + \frac{3}{2 - \ell n \frac{r}{b}} \right) \frac{dr}{r}$$

Integration can be performed by letting $\ell n \frac{r}{b} = x$ and $dx = \frac{dr}{r}$, which gives

$$\ell n |V_s| = - 2 \ell n \frac{r}{b} - 3 \ell n \left(2 - \ell n \frac{r}{b}\right) + C$$

From the boundary condition that $|V_s| = 1$ at $r = b$, the integration constant becomes $C = 3 \ell n 2$. Then,

$$\ell n |V_s| = - 2 \ell n \frac{r}{b} - 3 \ell n \left(1 - \frac{1}{2} \ell n \frac{r}{b}\right) ,$$

from which eq. (10) results;

$$|V_s| = \left(\frac{b}{r}\right)^2 \left(1 - \frac{1}{2} \ell n \frac{r}{b}\right)^{-3}$$

(2) Derivation of Eq. (16).

From eq. (14)

$$\frac{\xi}{r_o} = \frac{1}{r_o \sqrt{r_o}} \left(G(r) - G(b)\right)$$

where $$G(x) = \int \frac{\sqrt{x}}{\sqrt{1 - \left(\frac{x + a_o}{R}\right)^2}} dx \simeq \int \frac{\sqrt{x}}{\sqrt{2 \frac{r_o}{R} \left(1 - \frac{x}{r_o}\right)}} dx$$

76

Let $\frac{x}{r_o} = \sin^2 y$, then $\frac{dx}{r_o} = 2 \sin y \cos y \, dy$, and G(x) is expressed by

$$G(x) = \sqrt{\frac{R}{2}} \int \sqrt{\frac{\frac{x}{r_o}}{1 - \frac{x}{r_o}}} \, dx$$

$$= \sqrt{\frac{R}{2}} \; 2r_o \int \left(\frac{\sin y}{\cos y}\right) \sin y \cos y \, dy$$

$$= \sqrt{\frac{R}{2}} \; r_o \, (y - \sin y \cos y)$$

Thus

$$\frac{\xi}{r_o} = \sqrt{\frac{R}{2r_o}} \left[\sin^{-1} \sqrt{\frac{x}{r_o}} - \sqrt{\frac{x}{r_o}} \sqrt{1 - \frac{x}{r_o}} \right]_b^r$$

(3) Derivation of Eq. (20).

We start with

$$\frac{\xi}{r_o} = - \frac{1}{\cos\phi_m} \int_{r_o}^{b_\xi} \left(\frac{1 + \frac{1}{2} \ln \frac{b}{r_o}}{1 - \ln \frac{b}{r_o}} \right) \frac{db}{b}$$

Changing the variable according to $\ln \frac{b}{r_o} = x$ and $\frac{db}{b} = dx$, then

$$\frac{\xi}{r_o} = - \frac{1}{\cos\phi_m} \int_0^{\ln \frac{b_\xi}{r_o}} \left(- \frac{1}{2} + \frac{3/2}{1 - x} \right) dx$$

$$= \frac{1}{\cos\phi_m} \cdot \frac{1}{2} \ln \left[\frac{b_\xi}{r_o} \left(1 - \ln \frac{b_\xi}{r_o} \right)^3 \right]$$

where $\cos\phi_m$, from eq. (19), is expressed by

$$\cos\phi_m = \sqrt{\frac{2 \, r_o}{R}} \left(\frac{2}{3}\right) \sqrt{1 - \frac{b_f}{r_o}}$$

(4) Derivation of Eq. (21).

In order to integrate

$$\left(\frac{dr}{db}\right)_\xi = \left(\frac{r}{b}\right)\frac{1 - \frac{1}{2}\ln\frac{r}{b}}{1 + \ln\frac{r}{b}} \quad , \quad \text{let } \frac{r}{b} = x$$

Then

$$\frac{dr}{db} = x + b\,\frac{dx}{db} \text{ , and } b\,\frac{dx}{db} = x\left(\frac{1 - \frac{1}{2}\ln x}{1 + \ln x}\right) - x, \text{ or}$$

$$\frac{db}{b} = -\frac{2}{3}\left(\frac{1}{x\ln x} + \frac{1}{x}\right) dx \ .$$

Since the subscript ξ denotes an element ξ, the limits of integration are $b = b_\xi$ when $r = r_o$ and $b = b$ when $r = r$ for the element ξ. Thus,

$$\ln b \Big]_{b_\xi}^{b} = -\frac{2}{3}\ln(x\ln x)\Big]_{r_o/b_\xi}^{r/b}$$

$$\ln\left(\frac{b}{b_\xi}\right)^{3/2} = \ln\left\{\frac{r_o}{b_\xi}\ln\frac{r_o}{b_\xi}\Big/\frac{r}{b}\ln\frac{r}{b}\right\} \ ,$$

which gives eq. (21).

(5) Derivation of Eq. (22).

From eqs. (6) and (18), we have

$$\frac{hi}{h} = \frac{r}{r_o}\,\frac{ds}{d\xi} = \frac{r}{r_o}\,\frac{1}{\cos\phi_m}\,\frac{dr}{d\xi} \ , \text{ for } b = \text{const.} \ ,$$

where

$$\frac{dr}{d\xi} = \frac{dr}{db_\xi}\cdot\frac{db_\xi}{d\xi} \ .$$

Differentiating eq. (21) with b = constant, we obtain

$$\frac{dr}{db_\xi} = \frac{r_o}{\sqrt{b\,b_\xi}}\left(\frac{1 + \frac{1}{2}\ln\frac{b_\xi}{r_o}}{\ln\frac{b}{r} - 1}\right)$$

78

Differentiation of eq. (20) gives

$$\frac{db_\xi}{d\xi} = \cos\phi_m \left(\frac{\frac{b_\xi}{r_o}\left(\ell n \frac{b_\xi}{r_o} - 1\right)}{1 + \frac{1}{2}\ell n \frac{b_\xi}{r_o}} \right)$$

Therefore, $\frac{h_i}{h}$ becomes

$$\frac{h_i}{h} = \frac{r}{r_o}\frac{1}{\cos\phi_m}\frac{dr}{d_\xi} = \frac{r}{r_o}\sqrt{\frac{b_\xi}{b}}\left(\frac{1 - \ell n \frac{b_\xi}{r_o}}{1 - \ell n \frac{b}{r}} \right).$$

FIGURE TITLES

Figure 1. Shell Nosing Process (from Ref. [3]).

Figure 2. Die and Workpiece geometries and the coordinate system.

Figure 3. 3 Stages of the Shell configurations.

Figure 4. Comparison of various velocity distributions.

Figure 5. Preform dimensions, based on (a) solution I and (b) solution II.

Figure 6. Comparison of the approximate solutions with the solution by the new approach using the finite element method.

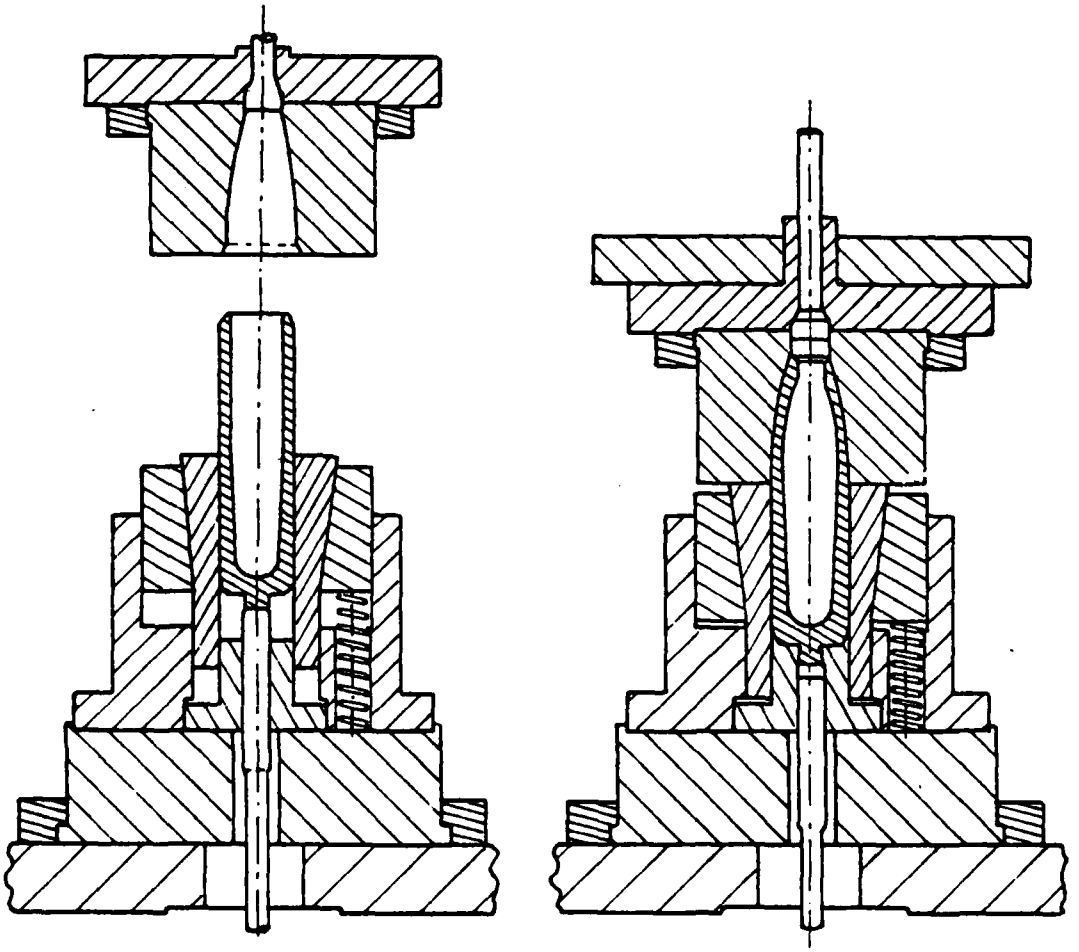

. Figure 1. Shell Nosing Process (from Ref. [3]).

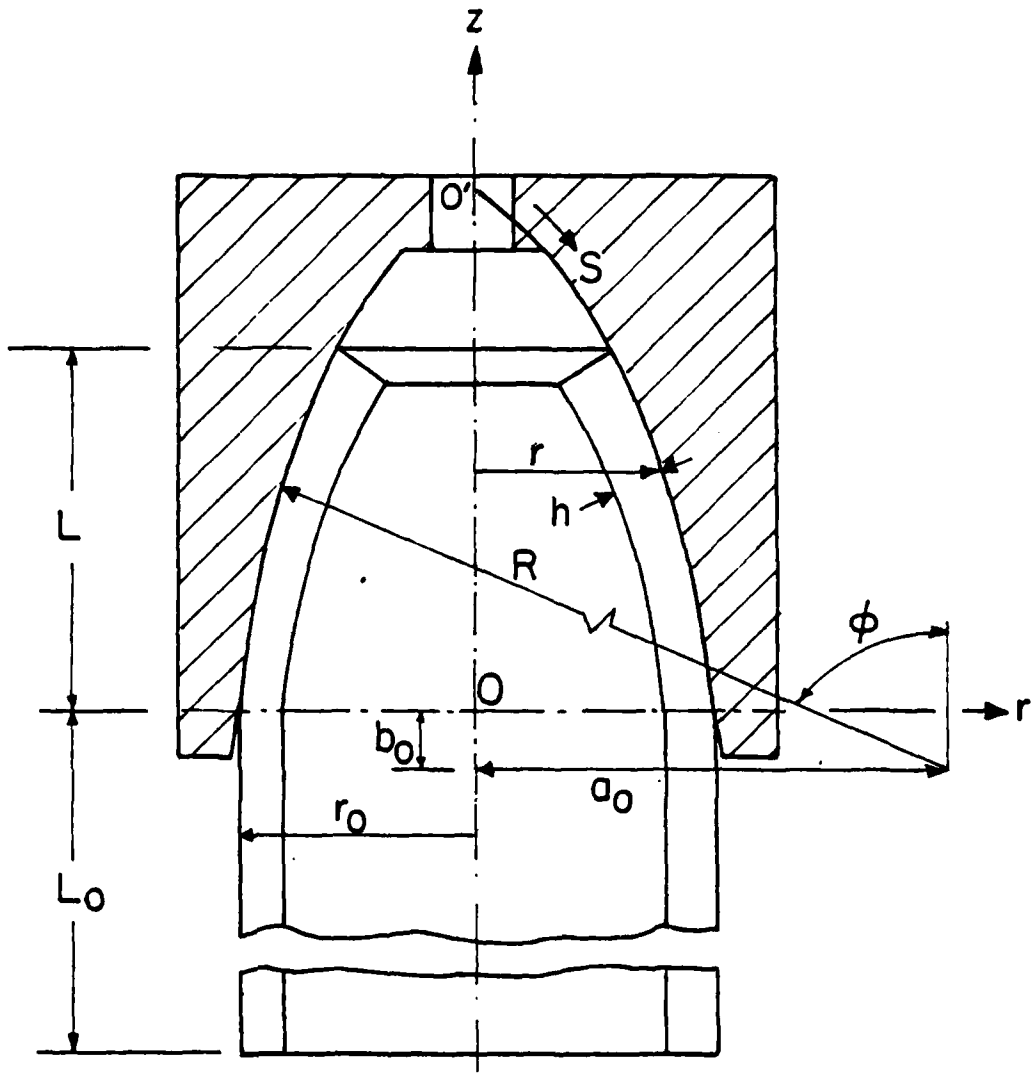

Figure 2. Die and Workpiece geometries and the coordinate system.

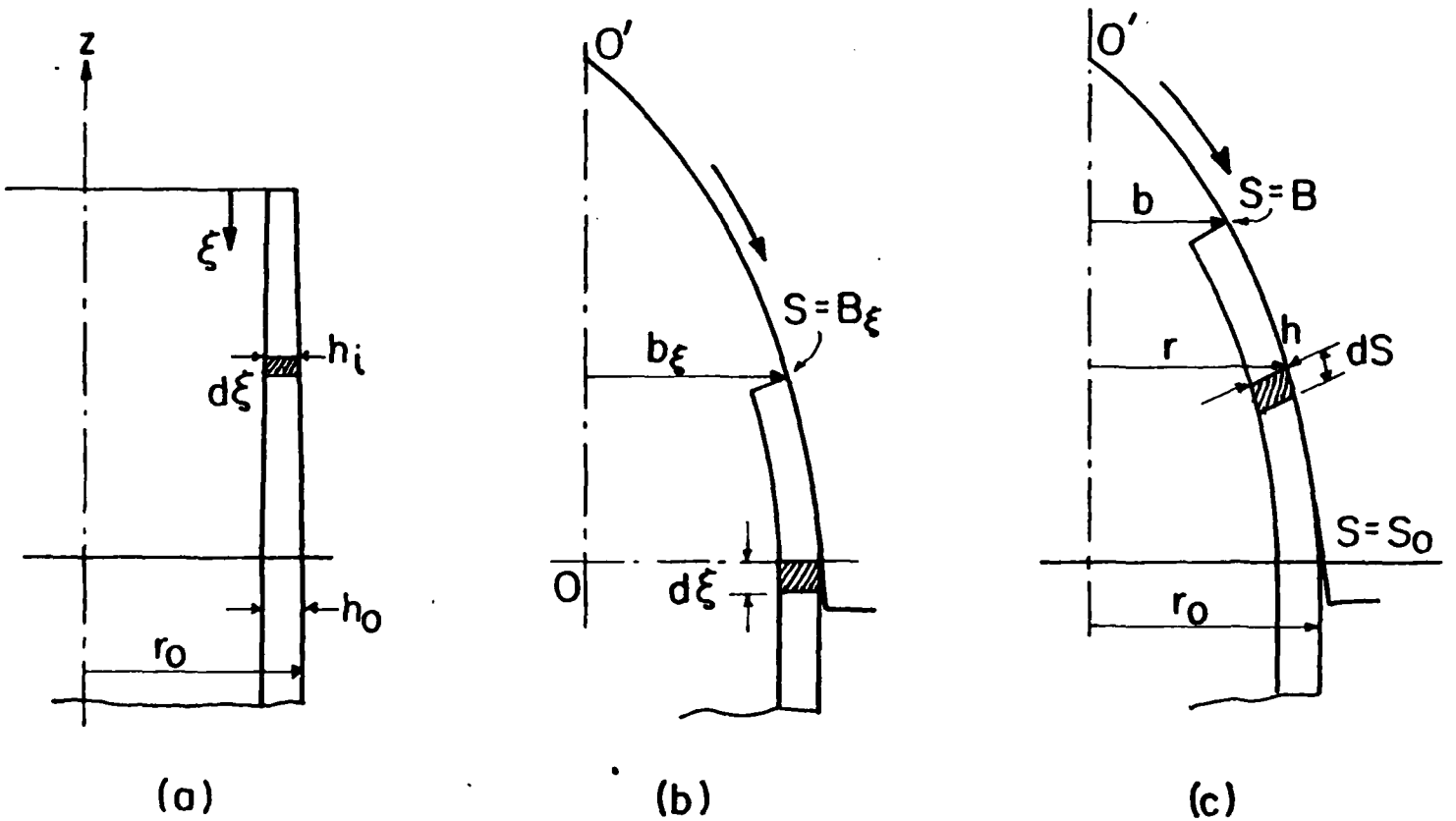

Figure 3. 3 Stages of the Shell configurations.

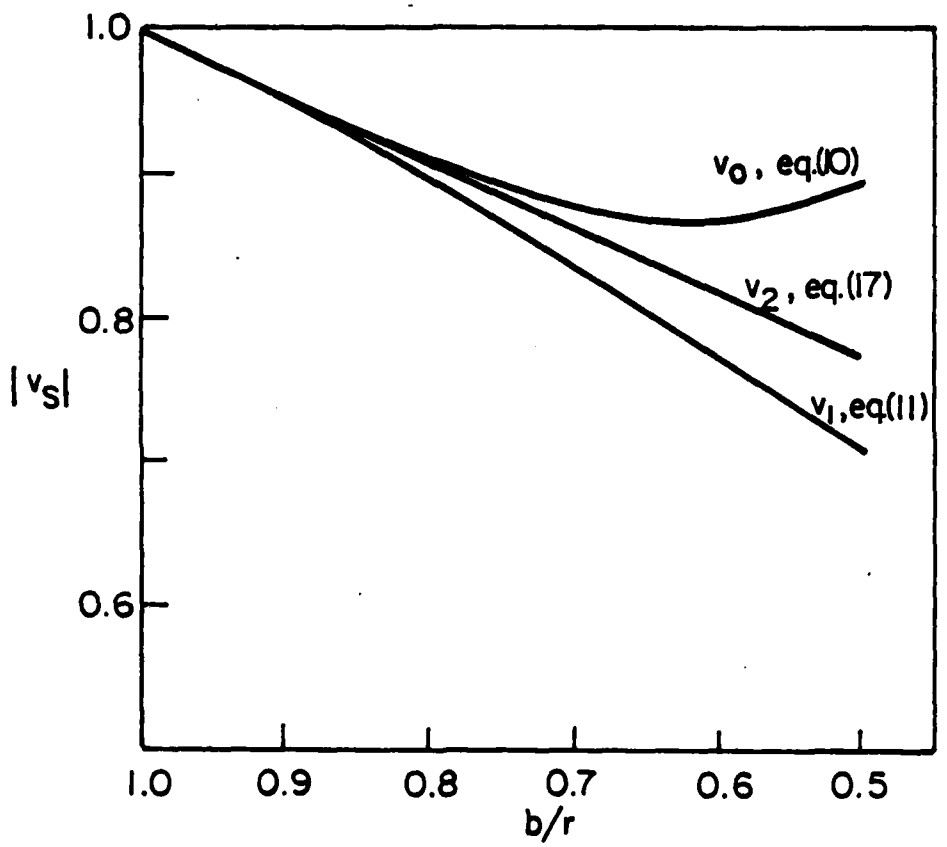

Figure 4. Comparison of various velocity distributions.

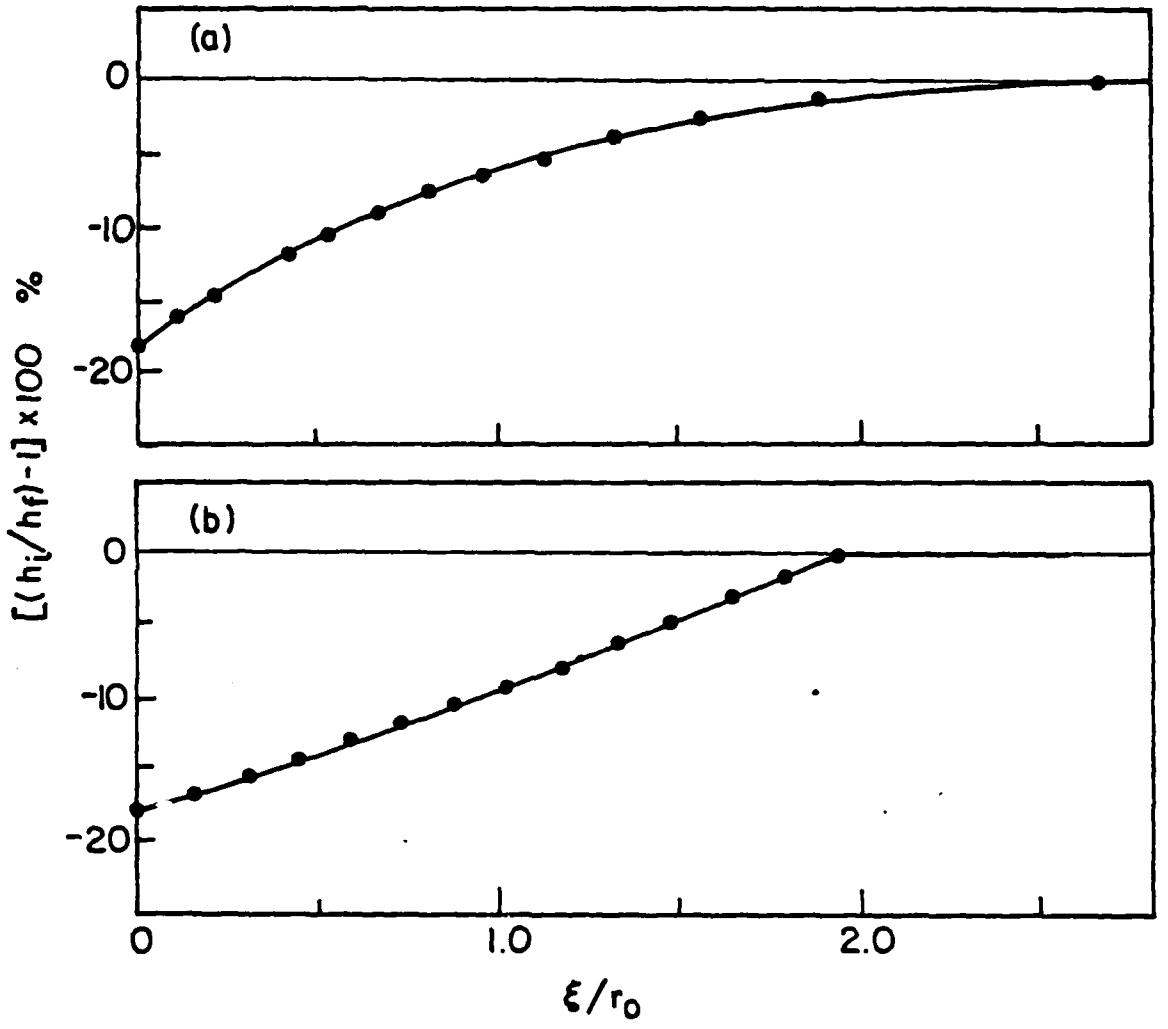

Figure 5. Preform dimensions, based on (a) solution I and (b) solution II.

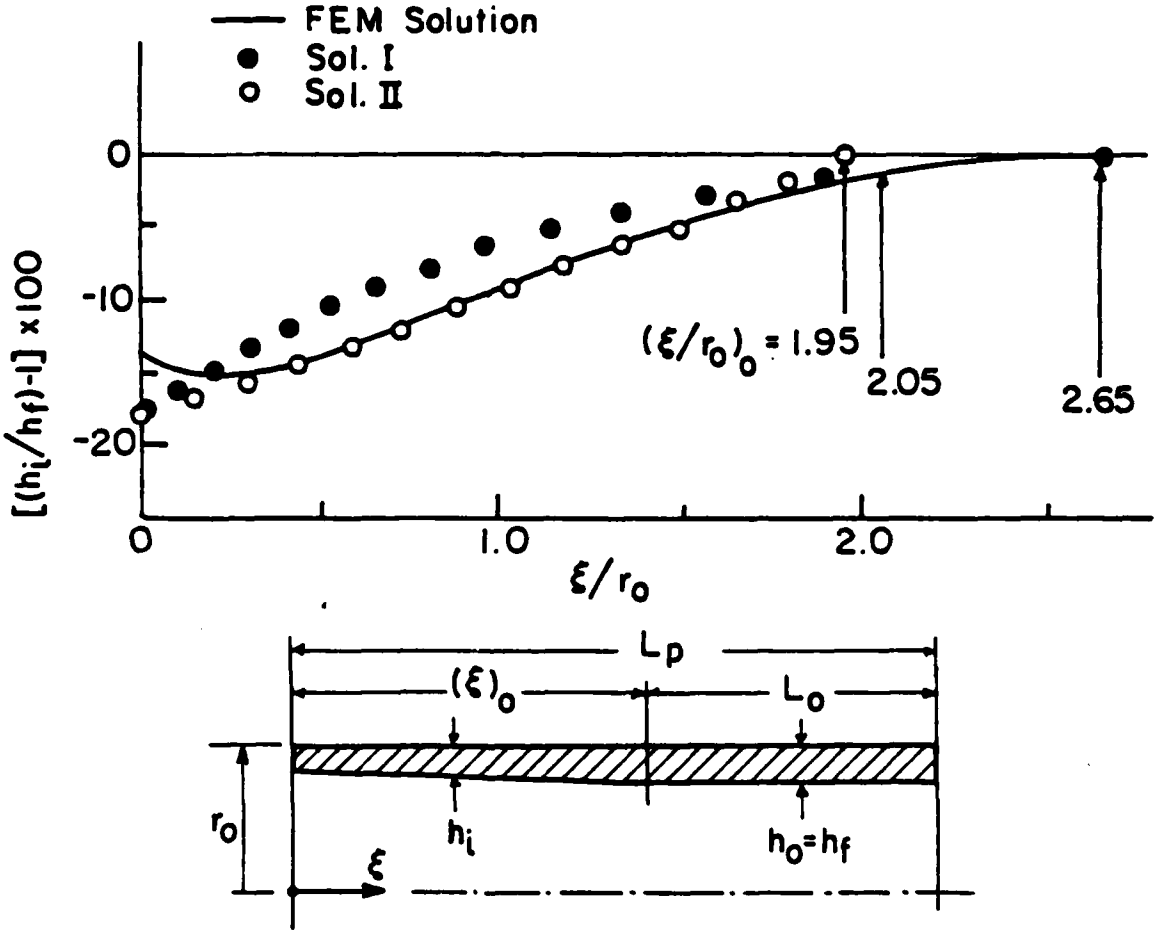

Figure 6. Comparison of the approximate solutions with the solution by the new approach using the finite element method.